

Reflection and Transmission Imaging of Thin Films

Thesis Submitted to the Faculty of Science and Health
for the Degree of Doctor of Philosophy

By

Jonathan Mullen B.Sc.



Dublin City University
School of Physical Sciences
Centre for Laser Plasma Research
Dublin City University

Research Supervisor
Dr. Paul van Kampen

March 2005

Declaration

I hereby certify that this material, which I now submit for assessment on the program of study leading to the award of Doctor of Philosophy is entirely my own work and has not been taken from the work of others save and to the extent that such work has been cited and acknowledged within the text of my work.

Signed : Jonathan Mallin I.D. No. : 50161725

Candidate

Date : 29/04/05.

To
My Family
(Past, Present and Future)

Acknowledgements

Firstly I would like to thank Dr Paul van Kampen for his continued advice, guidance and support during the course of this work. Our numerous discussions (when I could find him) allowed us to overcome some major obstacles in creating the system and producing the results presented in this thesis. Over the course of the years we developed a good friendship, which I hope will last for many years to come.

I would like to thank the heads of the physics department Professor Eugene Kennedy, Professor Martin Henry and Dr John Costello for giving me the opportunity to do my PhD in the school. I would also like to thank Professor Eugene Kennedy, Dr John Costello and Dr Jean Paul Mosnier for their help and advice during the course of the work.

I must thank the Des Lavelle and Cian Merne for their aid in designing and building the various mounts and holders required for the system. I would also like to thank the technicians in the undergraduate labs for the use of some of their equipment in the initial stages of the project.

A special thanks goes to Henry Barry and Dr Tony Cafolla for the use of the Profilometer and AFM respectively. Such measurements were vital to the end result. A special thanks also goes to Dr Brian Lawless who showed me how to work the evaporator and made numerous suggestions about an adequate substrate to use, not to mention other technical issues.

A great many thanks goes to the lads in the office and the lab. From the original crew Mark (The Stapes), John (Hirschy), Mohamed, Pat, Alan, John (Moore), Ger, James and Sarah. To the contemporary crew Eoin, Kevin, Deirdre and the newer members Ricky, Jean-Rene, Michal, Deirdre K, Alan, Caroline, John (Dardis) and the return of the Stapes.

Last but not least a great many thanks goes to all the active members of the DCU RockClimbing Club, who provided much needed distraction during weekends away and at the Wall.

Abstract

An experimental system was designed, built and used to determine the optical constants of materials in the Vacuum Ultraviolet region of the electromagnetic spectrum. An optical analysis chamber was designed to mount onto the back end of an existing monochromatic VUV imaging beam system, which covers a wavelength range from 30-200nm. The chamber may accommodate three different experimental configurations, allowing transmission and reflection measurements to be taken separately or at the same time.

A versatile computational analysis system was developed to process the data obtained with this experimental system. Recorded CCD images are aligned using a novel interpolation method, and reflection or transmission values are calculated from these. A Kramers-Kronig analysis program was developed and used to obtain a complete set of optical constants in the VUV region if reflection data is available over a sufficiently extensive wavelength range. The absorption coefficient of aluminium in the region between 30 and 85.5nm was determined to demonstrate the capabilities of the suite of experimental and computational analysis systems. The absorption coefficient of aluminium is shrouded in controversy in this region of the spectrum due to two papers with conflicting results ref [19] & [21].

Declaration	1
Acknowledgements	3
Abstract	4
1 Introduction	8
1 1 Layout	9
1 2 History	10
1 3 Reflection	13
1 3 1 Experimental Techniques	13
1 3 2 Kramers Kronig Analysis	14
1 4 Transmission	18
1 5 Reflection and Transmission	19
1 6 Plasmas	20
2 Theory	23
2 1 Light behaviour in vacuum	23
2 1 1 Energy of Light	25
2 2 Light in Materials	26
2 2 1 Reflection	27
2 2 2 Absorption	29
2 2 3 Complex Refractive Index	30
2 2 4 Dispersion of light	31
2 3 Kramers Kronig Analysis	33
2 4 Optical Sum Rules	35
2 5 Plasma light sources	36
2 5 1 Plasma Generation	37

2 5 2	Radiation and Ionisation processes	40
3	Experimental Set-up	43
3 1	Vacuum Ultraviolet Imaging Beam	43
3 1 1	Plasma Source Chamber	45
3 1 2	The Entrance Mirror Chamber	49
3 1 3	The Monochromator	50
3 1 4	The Exit Mirror Chamber	52
3 1 5	The CCD Camera	53
3 2	Material Analysis Set-up	54
3 2 1	Initial Chamber Designs	56
3 2 2	Reflection Chamber Configuration	61
3 2 3	Transmission Chamber Configuration	64
3 2 4	Reflection/Transmission Chamber Configuration	66
3 3	Filters	69
3 4	Creation of thin films	70
4	Data Analysis	74
4 1	Processing Data from the CCD Camera	76
4 2	Image Alignment	79
4 3	Extracting counts from the aligned images	89
4 3 1	Example 1 One Dimensional Arrays	90
4 3 2	Example 2 Two Dimensional Arrays	93
4 3 3	Filters	93
4 4	Calculating Absorption Data	95
4 4 1	Thickness Measurements	95
4 4 2	Absorption Spectra	100

4 5	Reflection Analysis	101
4 5 1	Kramers Kronig Analysis	101
4 5 2	Sum Rules	101
5	System Testing and Experimental Results	103
5 1	Testing of the Kramers Kronig analysis program	104
5 1 1	Generated Data	105
5 1 2	KK analysis of Experimental Data	112
5 2	Calcium Fluoride Testing	117
5 3	Filter Testing	120
5 3 1	Lithium Fluoride	121
5 3 2	Helium Gas	121
5 3 3	Argon Gas	126
5 4	Calcium Fluoride with a Filter	128
5 5	Aluminium Thin Films	130
5 5 1	TEM Grid Transmission	132
5 5 2	Free standing Aluminium on TEM Grids	133
5 5 3	Thickness Measurement	138
5 5 4	Absorption Coefficients	141
5 6	Conclusions and Discussions	150
5 7	Future Work	151
	References	152
	Appendix A	155
	Appendix B	162

The main object of this project is to build an analysis system that can be used to measure the optical constants of materials in the Vacuum Ultraviolet (VUV). The system comprises of an analysis chamber and a computerised analysis program. The analysis chamber can be mounted onto the back of an existing plasma beam light source with a wavelength range of 30-200nm (6-40eV) in the VUV region of the electromagnetic spectrum.

The analysis chamber is designed to gather transmission and reflection data from a sample material that is illuminated by the beam. The chamber is designed in such a way that both types of data can be measured separately or simultaneously. Either experimental technique allows for the determination of both the real and imaginary refractive indices of the material under study. The real (n) and imaginary (k) parts of the refractive index are collectively known as the optical constants, and may be combined to define the complex refractive index (\tilde{n}) (see equation (1.1)).

$$\tilde{n} = n - ik \quad (1.1)$$

This work is motivated both by the increased use of filters in the VUV and the lack of measured optical constants in that region. The determination of optical constants in this region is made difficult by the high absorption coefficient in the VUV of most materials. This barrier prevents the use of standard optics that are frequently used in the visible and infrared to measure optical constants. The system can thus be used as a research tool into optical constants in its own right, as well as a system to test materials useful as spectral filters for all the spectroscopic systems currently in DCU.

1.1

Layout

This thesis sets out how this goal was achieved. It is split into five main chapters:

Chapter 1 is this introductory chapter. It details how the thesis is laid out and gives the motivations for doing the work. The work that has been done by other authors in the area of optical constants research will be introduced. In their research they use a variety of techniques for measuring these constants and we will concentrate on those that use VUV radiation. The light source used in the experiments here is a laser-produced plasma and so a brief overview of these plasmas will also be presented.

Chapter 2 is the theory chapter. This chapter details the theoretical background to the behaviour of light in vacuum and in both absorbing and non-absorbing media. Reflection and transmission of light is explained by examining how light is affected by an interface between two materials. A detailed description of a Kramers Kronig analysis is given, showing how the real part of the refractive index maybe calculated if the imaginary part is known at all wavelengths and vice versa. Details about the optical sum rules and how they aid in the calculation and verification of optical constants are introduced. This chapter concludes with the basics of plasmas as VUV light sources, detailing their formation and how they produce the light used for the beam.

Chapter 3 details the experimental set-up. It describes the VUV beam apparatus from the initial plasma chamber through all the optical components to the detector. Attached to the beam apparatus is an analysis chamber. Its evolution from a simple chamber to its *final configuration shall be set out along* with the reasons for its

new design. The chapter will end with a look at the evaporator used to create thin films of aluminium.

Chapter 4 is the data analysis chapter. It contains the details of how the CCD images are processed, inputted into the analysis program and aligned so that the reflection or transmission data may be extracted. This data is then used to calculate absorption coefficients when carrying out transmission experiments, including details of how the thickness of the films were measured. In reflection experiments, the data can be used to calculate optical constants with a Kramers Kronig analysis.

Chapter 5 lists all the results from the experiments carried out with the system. It starts with some testing results done with the Kramers Kronig analysis routine along with calculations carried out on gold data found in the literature. We will then look at the initial experimental system testing, done using calcium fluoride windows. The data obtained indicated a need for using filters such as lithium fluoride, helium gas and argon gas. These filters were used in further experiments on calcium fluoride and aluminium films. The data from the transmission of the aluminium films is then used to generate the absorption coefficient for aluminium in the VUV and these are subsequently compared with measured and calculated data from the literature. This chapter concludes the thesis with a discussion of the work and the possible future developments, which could enhance the system and be used to improve the measured optical constants.

1.2 *History*

As mentioned above, the goal of this project is to design and build a system capable of measuring optical constants in the VUV. The measurement of optical constants has a long history dating back to the 17th century. However, the roots of the

interest in optics and the interaction of light with matter stretch back to the time of the Greek philosophers, where Pythagoras, Plato and Aristotle all devised their own theories of light propagating through space. These theories ranged from light rays being emitted from the eye as types of whiskers to light waves being emitted from matter.

These first theories of light paved the way for many more. Philosophers like Euclid, Hero, Ptolemy and Alhazen began to explain reflection and refraction of light, based on the same variety of ideas.

The next jump in understanding did not occur for six hundred years after Alhazen, when the first telescope was constructed and its workings explained by Galileo and Kepler. Shortly after this in 1621, Snell began lecturing about his theory on the refraction of light and introduced the concept of refractive index for the first time. Fermat verified Snell's theory of reflection mathematically with his law of least time for light rays.

A few years later, in 1665, dispersion was observed for the first time by Newton. This is another major step in the concept of optical constants, as dispersion is caused by the fact that refractive index is a wavelength dependent function. Around this time Newton proposed his corpuscular theory of light in which light is made up of massless particles of light. This theory was accepted for over a hundred years, even though in 1678 Huygens proposed the wave theory of light, the wave theory did not get much backing at that time due to the standing of Newton in the scientific community. In 1801 Young appeared to prove the wave theory experimentally when he demonstrated the interference effects of light. In 1821 Fresnel presented his famous laws, that describe how reflected and refracted light intensities may be calculated, details can be found in section 2.2.1.

In 1865 Maxwell put forward his equations describing the behaviour of electromagnetism and postulated that light was an electromagnetic wave, as the speed of electric and magnetic waves was equal to that of light. A few years later Michelson invented his interferometer and thus devised an accurate way of measuring the phase between two light waves.

Shortly afterwards, in 1887, Hertz observed the photoelectric effect but could not explain how it occurred. The first step in explaining it came in 1896 when Wien described how radiation from a black body varies with the temperature of that body. However, a theory developed from thermodynamic principles could not fully predict measurements of blackbody radiation at higher energies. According to the Rayleigh-Jeans law the intensity of the light scales as the square of the frequency at high wavelengths. This problem became known as the ultraviolet catastrophe.

Planck solved this problem in 1900, his explanation required the introduction of a new constant and the notion of a discrete unit of energy called a quantum. This allowed him to correctly model black body radiation in the ultraviolet.

In 1905 Einstein was able to explain the photoelectric effect that was noticed by Hertz a few years previously. The explanation introduced the notion that Planck's quanta (now called photons) can be thought of as particles. The energy of the photons is related to the frequency of the light. These discoveries showed how light interacts with matter and paved the way for more advanced theories such as wave particle duality, which is often summarised as "light travels like a wave yet interacts like a particle".

In 1911 Rutherford and Geiger discovered the nucleus of the atom. This discovery directed Bohr to his theory of the atom in which each electron occupies a stable orbit of discrete energy. Electrons moving to higher or lower orbits could then

explain absorption and emission. The stage was set for new developments in theory and experimentation. These new advancements in the understanding of light spurred an interest in the optical constants of materials. These measurements can now be split into three different methods: reflection, transmission and, reflection and transmission.

1.3 *Reflection*

The reflection experiments carried out through the years can be grouped up into two distinct sections: experimental techniques and the theoretical modelling and analysis of reflection data from experiments, the most common being the use of a Kramers Kronig analysis.

1.3.1 *Experimental Techniques*

Optical constants may be extracted from reflection data on the premise that the intensity of the incident and reflected light can be measured. If no data on polarisation can be measured, a technique called photometry is used, if polarisation can be measured, a technique called ellipsometry may be employed.

Drude made the first ellipsometric measurement in 1887. Using equations he derived, he managed to calculate the optical constants of a number of elements. Unfortunately with the death of Drude in 1906 the interest in ellipsometry waned, with very few measurements being made until the 1970s. From then on ellipsometry has been used to make measurements from the infrared to the ultraviolet with the only limiting factor being the availability of polarizers and analysers in the wavelength region of interest. Measurements have begun to be made in the vacuum ultraviolet. The main reasons for the time taken before measurements were made in the VUV are

both the difficulty in taking measurements at wavelengths where materials have such a large absorption coefficient and the lack of adequate light sources such as synchrotrons and laser-produced plasmas. By the 1980's however ellipsometry was widely available and several techniques of ellipsometry had evolved. A comprehensive overview of ellipsometry measurements is given by Hunter [1].

Photometry is principally the study of light intensities. For the case of reflection it entails the comparison of the incident light intensity with the reflected light intensity. The connection between the optical constants and the ratio of the light reflected against the incident light is presented in the form of the Fresnel equations described in section 2.2.1.

Another technique used associated changes in reflection at several measured angles to the optical constants. This technique was used by Scott *et al* [16] to carry out reflectance and oxide contamination tests on aluminium thin films. They deposited the aluminium and examined the reflectivity at varying angles. Using this system they were able to calculate optical constants for aluminium at 584nm.

1.3.2 *Kramers Kronig Analysis*

Accurate measurements of light intensities were not possible until the development of the photomultiplier tube during the Second World War. With such a device reflection data could be assembled and analysed using the theory developed over the previous century. Before this invention Kronig produced a paper [2] discussing the theory of dispersion of x-rays in materials and how the refractive index and absorption coefficient may be calculated. This was followed the year after by a paper by Kramers [3] who proved that if light holds true to the dispersion relations then it may not travel faster than light in vacuum. This showed the causal nature of

dispersion. The system is causal, as the effects of refractive index cannot be measured until the arrival of the E-field. Kronig then produced a proof for the equivalence of causality and dispersion in 1942 [4]. The Kramers Kronig relations have been used widely since the early days, even before Kronig's proof in 1942. The essence of the relations applied to optical constants is that by measuring either the real or imaginary parts of the refractive index for all frequencies (i.e. from 0- ∞), the other component of the complex refractive index can be calculated for all frequencies. This provides a very powerful analysis technique, however, with a substantial drawback (the summation from zero to infinity). Further details about the technique can be found in section 2.3.

The Kramers Kronig relations and the way they are applied are consistently being improved upon. Peterson and Knight [5] developed a Fast Fourier Transform based Kramers Kronig analysis routine which enabled a much faster Kramers Kronig analysis. Bortz *et al* [6] used the work done by Peterson *et al* to construct a method of calculating a Kramers Kronig analysis using a Fast Fourier Transform. In their paper they detailed how the range of the data used could be extended in order to increase the accuracy of the final calculation. Their hypothesis was tested by adding Theoretical 'wings' to the upper and lower energy regions of a test function simulating the effects of a data set tending to infinity. The test function consisted of three Lorentzian oscillators with equal oscillator strengths and equal width. The type of wings that were added depended on the energy region of interest. In the infrared region, the lower wing that gave the best results occurred when it tended towards the square root of the dc dielectric constant and when the high-energy wing tended towards that of the visible reflectivity. In the ultraviolet region, the lower wing that gave the best results tended towards the reflectivity of the visible and the higher wing was extrapolated

proportional to the negative fourth power of the photon energy as would occur for free electrons. Upon testing their analysis it was found that in the ultraviolet the best results were obtained when the higher wing tended towards the -5.6^{th} power of the photon energy, which does not hold for the use of free electron gas model. This model used for testing was of importance to our research as we were taking measurements in the VUV and we could use such a technique to test our Kramers Kronig analysis program (section 5.1.1).

Further advances in the use of Kramers Kronig analysis were carried out by Abdullah *et al* [7] who showed how a small region of data in the infrared could be sent through a Kramers Kronig analysis once sufficient boundary conditions are applied. These include that the data set must contain an absorption band between two points where the phase tends to zero. Having the phase tend to zero on either side of the absorption band is effectively isolating the absorption so that the system acts like an idealised damped oscillator and so all changes in the optical properties of the sample can be easily monitored.

The Kramers Kronig routine may also be used along with optical sum rules to evaluate spectra. Such an evaluation was carried out when Ehrenrich's results ([10] and [11]) for aluminium were used by Shiles *et al* [8]. Their paper detailed an iterative, self-consistent Kramers Kronig analysis technique that can be used with data from ellipsometry, absorption measurements, reflectometry and electron energy loss measurements. In this paper they apply their technique to metallic aluminium across a large wavelength region gathered from many sources. With the application of the sum rules (see section 2.4 for details) it was noticed that a reduction of 14% in the available extinction coefficient data around the L-edge gave a much better result.

consistent with the requirements of the sum rules. This was further supported by the agreement of the corrected data with the electron energy loss spectra of aluminium.

Barkyoumb *et al* [9] used data that was gathered by Shiles and added fine structure to the K-edge of aluminium. Such structure was noticed in measurements taken since Shiles' paper. He also added smoothing to some of the lower energy regions of Shiles data. This generated improved results in the mass absorption around the K-edge of aluminium.

The Kramers Kronig technique has been used extensively, especially in measurements on aluminium. One such measurement is that made by Ehrenreich *et al* mentioned previously [10] and [11] who described how his team used a Kramers Kronig analysis [12] to measure the optical constants of silver, copper and aluminium. This type of work on aluminium was continued through the years with an extensive study in the VUV done by Larruquert *et al* in a series of six papers from 1993-1997. These papers focussed upon reflectivity measurements of aluminium in the far ultraviolet from 80-120nm and one which probed from 77-80nm [13]. The interest was mainly in the effectiveness of aluminium mirrors in which they measured the resulting degradation of these mirrors after exposure to O₂ using apparatus described in [14]. Optical constants were then calculated for unoxidised aluminium films and the effects of recoating were shown. Comparison of Kramers Kronig data to electron energy loss spectra had been done previously. In line with other experiments French *et al* [15] carried out a comparative analysis of a Kramers Kronig analysis and electron energy loss measurement on a sample of Al₂O₃.

These are some of the major advances in measuring optical constants from reflectivity.

1.4

Transmission

Transmission measurements can give a lot of information concerning the absorption that occurs inside a material. A development in the determination of optical constants was demonstrated by Swanepoel [17]. He derived formulae for calculating the thickness and optical constants from interference effects from transmission measurements carried out on a flat sample. These equations were further extended to include rough samples [18]. This type of analysis is ideal for use with samples that are of a sufficient thickness that back reflections can destructively interfere with the penetrating light wave, however for samples that are sufficiently thick interference effects are not noticed. For such samples simple absorption techniques may be utilised.

Unfortunately some materials form an oxide layer once they come in contact with air. Such a problem with a fast forming oxide was faced by Gullikson *et al* [19]. He carried out photoabsorption measurements on aluminium in the 25-300eV range. In the experiments they measured several samples of aluminium each with a different measured thickness. All the films were handled in air and allowed to oxidise by the same amount of time, this allowed for a similar thickness of the oxide layer to form. This meant that when the transmission is plotted against the thickness the effect of the oxide layer is eliminated. The reason why it is eliminated is due to the thickness of the oxide layer on each sample being effectively the same, which results in a constant reduction in the transmission for each sample (see section 4.4). It was a simple yet cunning solution to a difficult problem.

When the data of Gullikson *et al* was compared with previous data [20] calculated from atomic scattering factors, it showed that the new data contained a lower mass absorption for the entire wavelength region. Keenan *et al* [21] carried out

similar transmission measurements on aluminium and utilised the style of analysis employed by Gullikson to correct for the oxide layer, but instead of using a plasma light source they used collisionally pumped Ne-like Ni and Ge XUV lasers that produced light at wavelengths of 53.7nm and 63.3nm respectively. Their results coincide with previous results by Henke *et al* [20] but not with those made by Gullikson *et al*. For their experiment they used a stepped sample made by vapour deposition. Both Gullikson and Keenan suggested that more measurements should be made in the region below the L edge for aluminium. The VUV beam has been optimised in this region, and so the work carried out as described in this thesis on aluminium absorption in the region used to test the system is highly important [56].

Work still continues on samples at longer wavelengths where the interference of thin films frequently plagued the analysis. Such techniques were used by Kubinyi *et al* [22] who utilised a computer simulation with transmission and incoming intensities values as an input for calculating the optical constants and thickness of the film. This worked by iterating the optical constants until an appropriate transmission was achieved. Similar computational work was done by Chambouleyron *et al* [23] whose paper describes a non-linear computer program which finds the optical constants and thickness of a film of a certain material and matches it up with measured transmission spectra. Denks *et al* [24] carried out transmission experiments on calcium fluoride in the VUV. This was particularly useful for the initial testing of the system in section 5.2.

1.5 *Reflection and Transmission*

A combination of both reflection and transmission methods on a single sample seems to be the ideal solution. However all the considerations of both styles of

measurement must be taken into account. Such experiments were carried out by Laaziz *et al* who wrote a series of papers detailing how the application of Swanepoels technique (using interference fringes) on samples less than 0.6 μm in optical thickness cannot be done to any great accuracy [25]. The reasoning behind this is the lack of the required number of fringes to carry out the analysis. The effect of spot size and thickness variation on the measurements was shown in another of his papers [26]. In the latest paper he details how a computational simulation using the data may be able to extract the required optical constants and thickness information when both reflection and transmission data are inputted [27]. At the same time work was done by Kepinska and Nowak [28]. They carried out reflection and transmission measurements on silicon using both measurements to calculate the optical constants and thickness of the samples. Similar equations to those of Swanepoel for transmission were used. Similar work by other authors has also been carried out but shall not be detailed here due to the similarities among their techniques.

1.6 *Plasmas*

The first laser produced plasma was created shortly after the invention of the laser in the 1960s. Following the production of such plasmas many papers were released concerning plasma formation, their propagation in vacuum and the interaction of the ionic species inside the plasma. Details of their formation and the radiation and ionisation processes that occur in plasmas may be found in section 2.5. The first experiments to be carried out on such plasmas were simple spectroscopic experiments to find out the type of emission spectra that emanate from a plasma. The quest for such information led to the development of a new technique, the dual laser plasma (DLP) technique. This technique was first carried out by Carillion *et al* [29].

in 1970 using aluminium plasmas. It involves the synchronisation of two lasers in such a way that the plasma furthest from the detector is used as a backlighting source, while the light produced by this plasma is used to probe the other plasma. Changing the time delay between the two plasmas has the effect of probing different parts of the second plasma. Thus its evolution in space and time may be mapped out.

During Carillion's experiments it was noticed that the emission from aluminium plasmas is highly line dominated in the VUV and so they are not suitable as a backlighting source. During later experiments improvements to the technique were made by using a material that would provide a continuum backlighting source plasma. Tantalum was such a material and was used by Breton *et al* [30] in 1973. Other high Z materials such as samarium, tungsten, europium and ytterbium were found to give equally good VUV continuum emission [31]. With an appropriate backlighting source many experiments were carried out on transitions in the VUV and XUV using the DLP technique. Many review papers have been written to summarise all the important work that has been done with laser plasmas.

Carroll *et al* [32] wrote one of the first of these in which the formation, evolution and diagnostics of plasmas are described in detail. This was followed by papers detailing photoabsorption experiments carried out in the extreme ultraviolet [33], and was followed by a review paper concerning all the experiments carried out in this region [34]. Theoretical models of how plasmas evolve in space and time were developed and their applicability was shown in [35] and in [36]. Both papers describe how a lithium plasma evolves in time and space from the initial laser shot till the final dispersion of the plasma. Such an evolutionary analysis was used in a computer simulation program developed by Stapleton [36], which can be used to model almost any kind of plasma once the appropriate target conditions are inputted into the

program The usefulness of the DLP technique was employed as the basis for developing another technique whose main aim is to image plasmas in the VUV [37] This imaging system utilised a plasma light source to produce a monochromatic parallel beam to probe other plasmas or materials in the VUV Such a system is the primary light source used for the experiments described in this thesis

The theoretical aspects of the understanding of light have come a long way in the last one hundred and fifty years with two immense leaps occurring due to Maxwell and Einstein (see section 1.2). This chapter will describe the theory of light where it applies to the work described in this thesis and how it can be used to explain effects such as reflection, absorption and dispersion in materials. The calculation of optical constants from the theory of reflected and transmitted light will be discussed, along with a theoretical analysis known as a Kramers Kronig analysis. It will be shown how sum rules derived from atomic theory can be used to further improve optical constant calculations. Alongside these improvements in the theory of light came the advancement in equipment foremost of which is the laser. The advent of the laser led to the development of laser produced plasmas, solely created due to the interaction between intense pulses of light and matter. These plasmas are the basis of the light source used in this work and shall be described in section 2.5.

2.1 *Light behaviour in vacuum*

Light in a vacuum behaves according to the laws of electromagnetism embodied in Maxwell's equations. The propagation of light can be described using the three-dimensional wave equation. Maxwell's equations describe the behaviour of electric and magnetic fields. A common form of these can be found in equations (2.1), (2.2), (2.3), and (2.4).

$$\nabla D = \epsilon_r \epsilon_0 \nabla E_{field} = \rho_c \quad (2.1)$$

$$\nabla B = \mu_r \mu_0 \nabla H = 0 \quad (2.2)$$

$$\nabla \times E_{ield} = -\mu_0 \mu_r \frac{\partial H}{\partial t} = -\frac{\partial B}{\partial t} \quad (2.3)$$

$$\nabla \times H = \epsilon_r \epsilon_0 \frac{\partial E_{ield}}{\partial t} + \sigma E_{ield} = \sigma E_{ield} + \frac{\partial D}{\partial t} \quad (2.4)$$

where D is the electric flux density, E_{ield} is the electric field (this is labelled to distinguish it from energy later in this chapter), B is the magnetic flux density, H is the magnetic field, ϵ_0 is the permittivity of free space, ϵ_r is the relative permittivity, μ_0 is the permeability of free space, μ_r is the relative permeability, ρ_c is the charge density and σ is the conductivity

Generally, the propagation of a wave can be described by equation (2.5)

$$\nabla^2 \varphi = \frac{1}{v^2} \frac{\partial^2 \varphi}{\partial t^2} \quad (2.5)$$

where φ is an oscillating function shown in equation (2.6)

$$\varphi(\vec{r}, t) = \varphi(\vec{k} \cdot \vec{r} \pm vt) \quad (2.6)$$

In equation (2.6) v is the speed of propagation, t is time, the vector \vec{r} is a three-dimensional position vector and the vector \vec{k} is the wave vector

With sufficient manipulation (see for example [40]) Maxwell's equations (2.1) to (2.4) can become those in equations (2.7) and (2.8)

$$\nabla^2 E_{ield} = \mu_0 \mu_r \epsilon_0 \epsilon_r \frac{\partial^2 E_{ield}}{\partial t^2} + \mu_0 \mu_r \sigma \frac{\partial E_{ield}}{\partial t} \quad (2.7)$$

$$\nabla^2 H = \mu_0 \mu_r \epsilon_0 \epsilon_r \frac{\partial^2 H}{\partial t^2} + \mu_0 \mu_r \sigma \frac{\partial H}{\partial t} \quad , \quad (2.8)$$

These equations represent oscillating damped electric and magnetic fields. The damping is due to the conductivity of the material that they are passing through, the fields therefore become undamped when the material's conductivity is zero. Both

equations (2.7) and (2.8) then take the form of the wave equation (2.5). This implies that both fields propagate through space at the same speed.

In a vacuum the relative permittivity and permeability are both equal to 1. From comparing equation (2.5) with both equations (2.7) and (2.8) it is clear that $\frac{1}{\sqrt{\mu_0 \epsilon_0}}$ is a speed; its value is numerically equal to the speed of light. This result for the speed of electric and magnetic field propagation led Maxwell to identify light as an electromagnetic wave.

2.1.1 *Energy of Light*

When light was recognised to be electromagnetic in nature, a new set of questions emerged regarding its interaction with matter. One major question concerning light was how much energy would be interacting with matter when light comes in contact with it. In classical electromagnetic theory, this energy can be calculated by assuming that the total energy in a light wave is made up of the energy contained in both the electric and magnetic fields. The energy flow of light is given by the Poynting vector (\vec{S}) and is defined by equation (2.9).

$$\vec{S} = c^2 \epsilon_0 \vec{E}_{field} \times \vec{B} \quad (2.9)$$

Its magnitude is essentially the power per unit area associated with the light wave; the direction is the same as the propagation direction of the wave.

The Poynting vector gives an important insight into the energy contained in light and how this energy is transported by an electromagnetic wave. Due to the Poynting vector being associated with both the instantaneous \vec{E} and \vec{B} fields it must be time dependent, like both \vec{E} and \vec{B} fields. If we wish to calculate the amount of energy that is coming in contact with an area such as the surface of a material, the

instantaneous value is often unimportant, as it changes on a timescale of nanoseconds. The time-averaged value of the Poynting vector at a given energy, is called the irradiance, it gives the average energy passing through an area per unit time. The total energy may then be calculated by multiplying the irradiance by the amount of time that the light is striking the area.

This was the accepted way of determining the energy of light for a number of decades until Planck began working on a model to account for blackbody radiation. In his model he introduced packets of energy known as quanta. The concept of light quanta was used later by Einstein to explain the photoelectric effect, see equation (2.10)

$$E = h\nu \quad (2.10)$$

where E is the energy of the photon, h is Planck's constant and ν is the frequency of the photon. The equation (2.10) shows the link between energy and the frequency of the incident radiation. The irradiance at a given photon energy is then simply the summation of the number of photons hitting a surface per unit time and is equal to the value of the time-averaged Poynting vector.

2.2 *Light in Materials*

When light is travelling through a medium the relative permeability and permittivity are no longer equal to 1. The velocity of the light wave then becomes that of equation (2.11)

$$v = \frac{1}{\sqrt{\mu_0 \epsilon_0 \mu_r \epsilon_r}} \quad (2.11)$$

The ratio of the velocity of light in a vacuum compared to inside a material is commonly known as the material's refractive index as given by equation (2.12)

$$n = \frac{c}{v} = \sqrt{\epsilon_r \mu_r} \quad (2.12)$$

For the majority of materials the magnetic permeability is close to unity. This leads to the refractive index being equal to the square root of the permeability of a non-magnetic material. When light passes from one material to another it must pass through an interface where the refractive index changes, this causes some interesting effects such as reflection.

2.2.1 *Reflection*

When light comes in contact with an interface between two materials of different refractive index a certain amount of reflection will occur. The amount of reflection and transmission at the interface is dependent upon the angle at which the incident light comes in contact with the interface and the refractive indices of both media. The behaviour was first described quantitatively by Fresnel. Even though his work predates that of Maxwell, Fresnel's equations can be obtained by applying boundary conditions on electromagnetic fields on both sides of an interface of two materials. A typical light interface interaction can be seen in Figure 2-1.

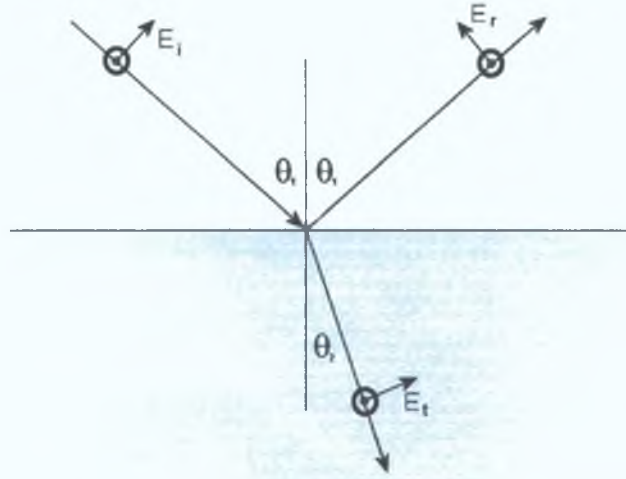


Figure 2-1 Representation of the E-fields as they are affected by an interface. The circles represent the B-fields coming out from the page [40].

When the boundary conditions of both the E and B fields are applied the identity $E_{field} = vB$ may be applied to get a second equation containing the E field. The two equations are then divided to get those in equations (2.13)-(2.16) [38]-[40].

$$r_{\perp} = \left(\frac{E_{or}}{E_{oi}} \right)_{\perp} = \frac{n_1 \cos \theta_1 - n_2 \cos \theta_2}{n_1 \cos \theta_1 + n_2 \cos \theta_2} \quad (2.13)$$

$$t_{\perp} = \left(\frac{E_{ot}}{E_{oi}} \right)_{\perp} = \frac{2n_1 \cos \theta_1}{n_1 \cos \theta_1 + n_2 \cos \theta_2} \quad (2.14)$$

$$r_{\parallel} = \left(\frac{E_{or}}{E_{oi}} \right)_{\parallel} = \frac{n_1 \cos \theta_1 - n_2 \cos \theta_2}{n_1 \cos \theta_2 + n_2 \cos \theta_1} \quad (2.15)$$

$$t_{\parallel} = \left(\frac{E_{ot}}{E_{oi}} \right)_{\parallel} = \frac{2n_1 \cos \theta_1}{n_1 \cos \theta_2 + n_2 \cos \theta_1} \quad (2.16)$$

where $r_{\perp/\parallel}$ is the reflection amplitude coefficient for light whose E-field is perpendicular and parallel light to the interface, $t_{\perp/\parallel}$ is the transmission amplitude coefficient for light whose E-field is perpendicular and parallel light to the interface,

E_{0r} is the intensity of the reflected light, E_{0i} is the intensity of the incoming light, E_{0t} is the intensity of the transmitted light, n_1 is the refractive index of medium that the light is coming from, n_2 is the refractive index of the medium that the light is going into, θ_1 is the incident angle and θ_2 is the transmitted angle. These equations only relate to the reflection and transmission at the interface and in the absence of absorption due to the material itself.

2.2.2 *Absorption*

The process of absorption is a major factor to be taken into account when light travels through any medium other than a vacuum. When light travels through a material it tends to interact with it. This interaction manifests itself in two forms: absorption and scattering. Absorption is caused when an incident photon has the same amount of energy that is required by an atom to be excited to a higher energy level. The photon is then absorbed by the atom, which increases the energy of the system. If the atom is part of a medium (gas, liquid or solid) the energy that the atom absorbed will be dissipated through the medium in the form of thermal energy or some other form of atomic movement. The absorption of radiation is dependent on the thickness and the absorption coefficient of the medium as shown by equation (2.17)

$$I = I_0 e^{-\alpha d} \quad (2.17)$$

where I is the intensity of light transmitted, I_0 is the incident intensity, d is the thickness of the medium and α is the absorption coefficient given by equation (2.18)

$$\alpha = \frac{4\pi k}{\lambda} \quad (2.18)$$

where k is the imaginary refractive index. The effect of absorption can be represented in Maxwell's equations by introducing a solution that includes the complex refractive index.

2.2.3 Complex Refractive Index

The solutions of the wave equation (2.7) for the electric field with $\sigma = 0$ is given by equation (2.19)

$$E_{inc,d} = E_0 \exp \left[i\omega \left(t - \left\{ \frac{z}{c} \right\} \{n\} \right) \right] \quad (2.19)$$

where E_0 is the amplitude of the incoming wave, ω is the angular frequency, t is the time, z is the direction of propagation and c is the speed of light. If the refractive index is assumed to be complex ($\tilde{n} \rightarrow n - ik$), as in equation (1.1) the solution becomes of the form of equation (2.20)

$$E_{inc,d} = E_0 \exp \left[i\omega \left(t - \left\{ \frac{z}{c} \right\} \{n - ik\} \right) \right] \quad (2.20)$$

When the solution with complex refractive index in equation (2.20) is substituted into the damped wave equation (2.7), equation (2.21) is obtained

$$(n - ik)^2 \left(\frac{\omega}{c} \right)^2 = \mu_0 \mu_r \epsilon_0 \epsilon_r \omega^2 + \mu_0 \mu_r \sigma i \omega \quad (2.21)$$

The real and imaginary parts can then be equated to give equations (2.22) and (2.23)

$$n^2 - k^2 = c^2 \mu_r \epsilon_r \mu_0 \epsilon_0 \quad (2.22)$$

$$2nk = \frac{\sigma}{\omega \epsilon_0} \quad (2.23)$$

These equations relate the optical constants n and k to the permittivity, permeability, conductivity and frequency [38],[40]. Equation (2.22) can also be related to ϵ_r (the

real part of the dielectric constant) and equation (2 23) can be related to ε_2 (the imaginary part of the dielectric constant)

The introduction of complex refractive index also affects the Fresnel equations. These can be seen in [38] where it is shown how letting the refractive index $\tilde{n}=n-ik$ results in the definition of the identity in equation (2 24) to reduce the complexity of the calculations later on

$$\tilde{n} \cos \theta = u - iv \quad (2\ 24)$$

This identity is then applied for both media at the interface and results in a simplification of the Fresnel equations in absorbing media. These then take the useful form given by equations (2 25), (2 26), (2 27) and (2 28)

$$r_{\perp} = \frac{(u_1 - iv_1) - (u_2 - iv_2)}{(u_1 - iv_1) + (u_2 - iv_2)} \quad (2\ 25)$$

$$r_{\parallel} = \frac{(u_1 - iv_1)(n_2 - ik_2)^2 - (u_2 - iv_2)(n_1 - ik_1)^2}{(u_1 - iv_1)(n_2 - ik_2)^2 + (u_2 - iv_2)(n_1 - ik_1)^2} \quad (2\ 26)$$

$$t_{\perp} = \frac{2(u_1 - iv_1)}{(u_1 - iv_1) + (u_2 - iv_2)} \quad (2\ 27)$$

$$t_{\parallel} = \frac{2(n_1 - ik_1)(n_2 - ik_2)}{(n_2 - ik_2)^2 + [(n_1 - ik_1)(u_1 - iv_1)/(u_1 - iv_1)]} \quad (2\ 28)$$

These equations can be used to model the reflection or transmission of a material as long as the values of n and k are known for the materials on either side of the interface. The intensity of the reflected light is equal to r^2 , and that of the transmitted light is t^2 .

2.2.4 Dispersion of light

The dispersion of light is a phenomenon that is readily noticed when white light passes through a prism. The effect is due to the fact that a medium's refractive index

is wavelength dependent. This can be shown by applying a damped harmonic oscillator model to predict how a medium's refractive index changes with wavelength when an incident beam of light is passing through it.

When a dielectric medium is subjected to an electric field, it causes the electrons to oscillate about their equilibrium positions inside the medium. This creates internal dipole moments, which results in a polarisation (P) given by equation (2.29).

$$P = (\epsilon - \epsilon_0) E_{field} \quad (2.29)$$

The electromagnetic field associated with the light wave is harmonic and so the internal charge structure experiences a time-varying force. The atoms or molecules have sufficient mass that their inertia keeps them relatively stable, but the electrons have much less inertia so they tend to react more readily to the variations in the electric field. Since each electron is bound to the nucleus of the atom we can model the electron interactions with light by a simple harmonic oscillator model. The natural frequency of the oscillation is given by equation (2.30).

$$\omega_0 = \sqrt{\frac{k'}{m_e}} \quad (2.30)$$

The force (F_E) being exerted upon the electron is given by equation (2.31)

$$F_E = q_e E_0 e^{i\omega t} \quad (2.31)$$

We may then show how the forces are affecting the electron using equation (2.32)

$$q_e E_0 e^{i\omega t} - m_e \omega_0^2 x - m_e \gamma \frac{dx}{dt} = m_e \frac{d^2 x}{dt^2} \quad (2.32)$$

where m_e is the mass of the electron and a damping term $m_e \gamma dx/dt$ has been included.

We can assume that the electron is oscillating at same frequency as the electric field

and so a solution for equation (2 32) is of the form $x(t)=x_0e^{i\omega t}$ With this in mind we obtain a value for the complex amplitude \hat{x}_0 given by equation (2 33)

$$\hat{x}_0 = \frac{q_e}{m_e (\omega_0^2 - \omega^2) - i\gamma\omega} \quad (2 33)$$

Since the electric polarisation is equal to the density of dipole moments we can be easily shown that the polarisation is equal to equation (2 34)

$$P = Nq_e x = \frac{Nq_e^2}{m_e (\omega_0^2 - \omega^2) + i\gamma\omega} \quad (2 34)$$

where N is the number of atoms per unit volume We can then apply equation (2 29) and the identity $n^2 = \epsilon/\epsilon_0$ to give a value for the frequency dependent refractive index in equation (2 35)

$$n^2(\omega) = 1 + \frac{Nq_e^2}{\epsilon_0 m_e} \sum_j \frac{f_j}{\omega_{0j}^2 - \omega^2 + i\gamma_j\omega} \quad (2 35)$$

Generalising this to a number of harmonic oscillators, each with oscillator strength of f_j and a damping term of γ_j , we obtain equation (2 35) A similar equation is used in section 5 1 1 to simulate refractive index and test our Kramers Kronig analysis program

2.3 *Kramers Kronig Analysis*

The Kramers Kronig analysis is the result of the link between dispersion theory used to calculate optical constants [2] and dielectric constants [3] and causality Kronig first proved this link in 1942 [4] The resulting equations to calculate real and imaginary refractive indices can be seen in (2 36) and (2 37)

$$k(\omega_0) = -\frac{2\omega_0}{\pi} P \int_0^\infty \frac{n(\omega) - 1}{\omega^2 - \omega_0^2} d\omega \quad (2 36)$$

$$n(\omega_0) - 1 = \frac{2}{\pi} P \int_0^\infty \frac{\omega k(\omega)}{\omega^2 - \omega_0^2} d\omega \quad (2.37)$$

These equations allow us to calculate the real part of the refractive index if the imaginary part is known for all wavelengths, and vice versa. Such a link between real and imaginary components may also be used with reflection intensities (the real part) whose imaginary part is the phase change upon reflection seen in equation (2.38). Such a calculation is ideal for use with measurements of reflection spectra that will be obtained using the chamber configuration in section 3.2.2.

$$\varphi(\omega_0) = -\frac{2\omega_0}{\pi} P \int_0^\infty \frac{\ln(\sqrt{R(\omega)})}{\omega^2 - \omega_0^2} d\omega \quad (2.38)$$

where

$\varphi(\omega)$ = the phase at energy ω

P = the principal part of the integral (this is integrating around the singularity that occurs when $\omega = \omega_0$).

$R(\omega)$ = the percentage reflection at energy ω

This is one of the most used forms of the Kramers Kronig analysis for obtaining optical constants from reflection spectra. When the reflectance of a material is taken the spectrum can be inputted into equation (2.38) resulting in the calculation of the phase. The optical constants may then be calculated using equations (2.39) and (2.40)

$$n(\omega) = \frac{1 - R(\omega)}{1 + R(\omega) - 2\sqrt{R(\omega)} \cos[\varphi(\omega)]} \quad (2.39)$$

$$k(\omega) = \frac{-2\sqrt{R(\omega)} \sin[\varphi(\omega)]}{1 + R(\omega) - 2\sqrt{R(\omega)} \cos[\varphi(\omega)]} \quad (2.40)$$

The dielectric constants may also be calculated using the equations (2.22) and (2.23).

2.4 *Optical Sum Rules*

Optical sum rules stem from the same source as the Kramers Kronig analysis, the dispersion relations. The first sum rule that we will look at is sometimes referred to as the inertial sum rule. This rule is shown in equation (2.41) [8],[41].

$$\int_0^{\infty} [n(\omega) - 1] d\omega = 0 \quad (2.41)$$

The inertial sum rule can be used to test the accuracy of any extrapolation of the real refractive index by normalising and is commonly used to test Kramers Kronig analyses (see section 4.5.2).

Optical measurements are not the only type of measurements that can be made, light is electromagnetic in origin, so electrical sum rules can be brought into this too. Those include the dc conductivity sum rule equation (2.42), which equates the sum of the real dielectric constant to the dc conductivity (σ_0) of the material under analysis.

$$\int_0^{\infty} [\epsilon_1(\omega) - 1] d\omega = -2\pi^2 \sigma_0 \quad (2.42)$$

Since the real dielectric constant can be linked to the optical constants a simple measurement of the conductivity is all that is needed to apply this sum rule.

Other sum rules of similar style are collectively known as the f -sum rule. These relate the imaginary dielectric (equations (2.43), (2.45)) and optical (equation (2.44)) constants to the plasma frequency of the material. These are also quite useful and are easily applied as the plasma frequency can be calculated from equation (2.52)

$$\int_0^{\infty} \omega' \varepsilon_2(\omega') d\omega' = \frac{\pi}{2} \omega_p^2 \quad (2.43)$$

$$\int_0^{\infty} \omega' k(\omega') d\omega' = \frac{\pi}{4} \omega_p^2 \quad (2.44)$$

$$\int_0^{\infty} \omega' \text{Im}[\varepsilon^{-1}(\omega')] d\omega' = -\frac{\pi}{2} \omega_p^2 \quad (2.45)$$

These sum rules can be manipulated to give the effective number of electrons (Z_{eff}) that can take part in optical processes below energy ω . These rules are known as the partial f sum rules and can be seen in equations (2.46), (2.47), (2.48)

$$Z_{eff}(\omega)|_{\varepsilon} = \frac{m_e}{2\pi^2 e^2} \int_0^{\omega} \omega' \varepsilon_2(\omega') d\omega' \quad (2.46)$$

$$Z_{eff}(\omega)|_k = \frac{m_e}{\pi^2 e^2} \int_0^{\omega} \omega' k(\omega') d\omega' \quad (2.47)$$

$$Z_{eff}(\omega)|_{\varepsilon^{-1}} = \frac{m_e}{2\pi^2 e^2} \int_0^{\omega} \omega' \text{Im}[\varepsilon^{-1}(\omega')] d\omega' \quad (2.48)$$

If we let $\omega \rightarrow \infty$, then all three calculated values of $Z_{eff}(\omega)$ should tend to Z , the number of electrons in the atom. Thus the f sum rules provide an effective way of verifying the accuracy of any optical constant measurement.

2.5 *Plasma light sources*

According to the Oxford English Dictionary a plasma is “a gas of positive ions and free electrons with little or no overall electric charge”. This is a concise description of a plasma, also known as the fourth state of matter. The plasma state is the most abundant in the universe constituting about 99% of all observed matter.

A plasma can be generated in the laboratory in a number of ways. Two common methods are firstly, by using electrical discharges to heat up a gas to sufficient temperatures to allow electrons to escape creating an electron ion pairs. These radio frequency plasmas tend to be used for processing or etching materials specifically in the production of microprocessors. A second way of generating a plasma is by firing an intensely focussed laser beam onto a target, which raises the temperature of the material enough to ablate material from the target surface and allows the separation of electrons from the atoms.

The main use of a laser-produced plasma in this work is as a VUV light source. The reason laser produced plasmas are used as light sources, is due to the high temperatures and ionisation density that occurs in the plasma allowing for production of continuum VUV and XUV light. Continuum emission takes place when a plasma is created from a high-Z material. The line emission due to the resulting highly ionised atoms is spread over such a large number of transitions that the lines tend to blend into a quasi-continuum.

2.5.1 *Plasma Generation*

A plasma is generated when a light beam from a high power, Q-switched laser is focussed onto a target, in this case it shall be assumed that the target is solid. When the laser light hits the target some of the light is reflected off the target, the amount is dependent on the energy of the light and the optical properties of the material at that energy, see section 2.2.1. The remainder of the light penetrates into the target by a small fraction of the wavelength, this depth is known as the skin depth δ and is given by equation (2.49)

$$\delta = \sqrt{\frac{2}{\omega \mu \sigma}} \quad (2.49)$$

where ω is the angular frequency of the incident light defined to be equal to $2\pi\nu$ (ν is the frequency of the light), μ is the magnetic permeability of the material and σ is the conductivity of the material

The light that enters the material is absorbed and causes a heating effect on the target, which after a short period of time results in the material reaching its melting temperature. Shortly afterwards the energy exceeds the latent heat of vaporization of the material resulting in evaporation. The amount of energy required for this to occur limits the power at which a plasma can possibly form as the material needs to be in a gaseous state before it can become a plasma. This threshold power ($P_{threshold}$) is given by equation (2.50)

$$P_{threshold} = \rho L_{vapour} \sqrt{\frac{a}{T_{pulse}}} \quad (2.50)$$

where ρ is the target density, L_{vapour} is the latent heat of vaporisation, T_{pulse} is the laser pulse duration and a is the diffusivity defined by equation (2.51)

$$a = \frac{K}{\rho C_p} \quad (2.51)$$

where K is the thermal conductivity and C_{sp} is the specific heat capacity. The target being used to generate the plasma in the experiments is made of Gold whose properties are given in Table 2-1

Table 2-1 Constants for Gold [50]

Density	0.0193 kgcm ⁻³
Thermal conductivity	3.17 Wcm ⁻¹ K ⁻¹
Specific heat capacity	128Jkg ⁻¹ K ⁻¹
Latent heat of vaporisation	1.64495×10 ⁶ Jkg ⁻¹
Diffusivity	1.28cm ² s ⁻¹
Laser pulse duration	10ns
Power threshold	3.59×10 ⁸ Wcm ⁻²

The power densities that are used in our experiments range from 10⁹ – 10¹² Wcm⁻². This will allow evaporation to occur at the surface, and a very dilute plasma is produced. The radiation will then interact with the plasma and the photons that are energetic enough will ionise the atoms. Some of the free electrons proceed to ionise other atoms through collisions. Both processes result in a cascade effect producing a very rapid increase in the amount of electrons released. The high electron density has an effect on the light passing through the plasma, since the electron oscillations in the plasma are characterised by the plasma frequency (ω_p) shown in equation (2.52)

$$\omega_p = \sqrt{\frac{n_e e^2}{m_e \epsilon_0}} \tag{2.52}$$

where n_e is the electron density, e is the charge on an electron, m_e is the mass of an electron and ϵ_0 is the permittivity of free space. The light travelling through the plasma is related to the plasma frequency by equation (2.53)

$$\omega^2 = \omega_p^2 + c^2 k^2 \tag{2.53}$$

where c is the speed of light in a vacuum and k is the propagation constant. The propagation constant has a real value when $\omega > \omega_p$ resulting in the light wave propagating through the plasma. When $\omega < \omega_p$, k becomes imaginary and the wave is not transmitted through the plasma. The light wave is reflected during the times that $\omega = \omega_p$. This occurs when the plasma has reached the critical density, shown in equation (2.54)

$$n_c = \frac{\epsilon_0 m_e \omega^2}{e^2} \quad (2.54)$$

When the critical density is reached the light no longer comes in contact with the target and so no more ions are introduced to the plasma at this time. The laser light still interacts with the plasma and so the laser pulse can generate multiply ionised species, however at the same time the plasma expands away from the target and takes up an even greater volume. This increase in volume leads to a reduction in electron density, which reduces the electron density below the critical density allowing the laser light to transmit through the plasma and ablate more material.

2.5.2 *Radiation and Ionisation processes*

There are a few radiation processes that occur inside plasmas during their lifetime and for each process its opposite form also exists. These processes may be split into three distinct sections due to the type of interactions that are involved. They are bound-bound transitions, free-bound transitions and free-free transitions.

Bound-bound transitions occur when a bound electron that is bound to an atom or ion is raised to another bound state due to photon or collisional interactions. Photo-excitation occurs when an atom/ion absorbs a photon that is energetic enough to raise the atom/ion to a higher energy state. The inverse process, photo de-excitation, when

an atom/ion that is currently in an excited state decays to a lower state due to fluorescence may also occur. The energy of the emitted photon is equal to the difference in energy between the higher to the lower state. The resulting spectrum has discrete lines associated with these types of transitions. Similar transitions due to collisions also occur and are known as collisional excitations. These happen when an atom/ion collides with another particle. The collision causes the atom/ion to be raised to a higher state whose energy change is directly related to the kinetic energy lost during the collision. Collisions with electrons tend to be more efficient for such transitions than any other particles due to the electrons being smaller in mass and can easily transfer their kinetic energy during collisions. Similarly collisional de-excitation also occurs and results in excitation energy being converted into kinetic energy of a particle when it comes in contact with the atom/ion in an excited state.

Free-bound transitions occur when an electron is freed from a bound state around an atom/ion or when it gets bound back to an atom/ion from its free state. This occurs due to both radiative and collisional interactions. Photo-ionisation may take place when a photon has sufficient energy to free an electron from an atom/ion thus increasing the ionisation. The opposite effect, called photo-recombination also occurs and is due to an electron recombining with an ion under the emission of a photon. The recombination spectrum takes the form of a continuum. The collisional form of this interaction is known as collisional ionisation. It happens when the kinetic energy of an electron is sufficiently high to free another electron from an atom/ion during a collision. Its inverse form, collisional recombination occurs when two electrons collide with an ion. One of the electrons recombines with the ion resulting in an increase in kinetic energy of the system.

Free-free transitions occur between two free bodies, be it electrons or ions. It takes two forms, bremsstrahlung and inverse-bremsstrahlung. Bremsstrahlung occurs when an electron comes in contact with a particle such as an ion. This allows for a transition of the system to a lower energy state, which results in the emission of a photon and the spectrum of this is a continuum. Inverse-bremsstrahlung is the opposite process where a photon is absorbed by an electron-ion pair. The electron gains kinetic energy as a result. Both these processes are the main energy conversion methods that occur inside a plasma during its lifetime. This is due to the fact that the laser energy is absorbed by inverse-bremsstrahlung, which increases the kinetic energy of the electrons, resulting in more collisions and increases the ionisation of the plasma.

In the gold plasma used for the VUV beam a continuum is emitted. As with other high-Z materials, the line emission spectrum has the appearance of a continuum due to the immense number of lines, each with a low level of probability of occurring, lying close to each other. Such a quasi continuum can even surpass that of the free-free and free-bound continuum states [42]. In the wavelength region of interest 30-200nm details on gold spectra was given by Carroll *et al* [42] and at lower wavelengths 2-10nm [43].

The experimental setup contains a wide range of equipment, which can be categorised into 3 main sections

- 1 The light source
- 2 The analysis chambers
- 3 Thin film production and thickness measuring

In section 3.1 all facets of the equipment that produce the beam are discussed in detail, from the initial laser pulse to the detection of the beam. In section 3.2 three possible configurations of the analysis chamber are discussed. These include the initial concept designs and their implementation into the final configurations of a simple transmission chamber, a reflection chamber (which we labelled the KK chamber), and a combined reflection and transmission chamber configuration. Section 3.3 introduces the types of filters that are used for the different wavelength ranges. The chapter will conclude with details of the evaporator that was used to grow the thin films.

3.1 *Vacuum Ultraviolet Imaging Beam*

The Vacuum Ultraviolet Imaging Beam, or VUV beam, was designed and built by John Hirsch as a major part of his PhD work in Dublin City University [44]. It was designed to produce a tuneable collimated beam in the vacuum ultraviolet region of the electromagnetic spectrum (from 30-200nm). This system became fully operational in the spring of 2003 and it has been used to get absorption images of a plasma comprising of various ionised states of calcium and barium for which the

results can be found in [37]. In contrast with DLP experiments, the plasma under investigation was probed with a beam of monochromatic light instead of with continuum light. The advantage of using a monochromatic beam is that a single species of ion can be tracked in two spatial dimensions as the plasma expands in space and time. Monochromatic light is ideal for this as a certain wavelength of light can be selected, which can be absorbed by only one of the ion stages in the plasma.

The VUV beam was designed to facilitate the swapping of sample test chambers and as a result the beam could be used for a variety of experiments. In this work the VUV beam is used in the optical analysis of materials. We focussed our experiments on materials that would be useful as filters or windows in the VUV. The apparatus for the beam is an $f/100 \times f/100$ aperture system, which delivers a 4mm x 4mm square beam. The system is composed of six main parts (Figure 3-1)

- 1 Plasma source chamber
- 2 Entrance mirror chamber
- 3 Monochromator
- 4 Exit mirror chamber
- 5 Sample Test chamber
- 6 Detector

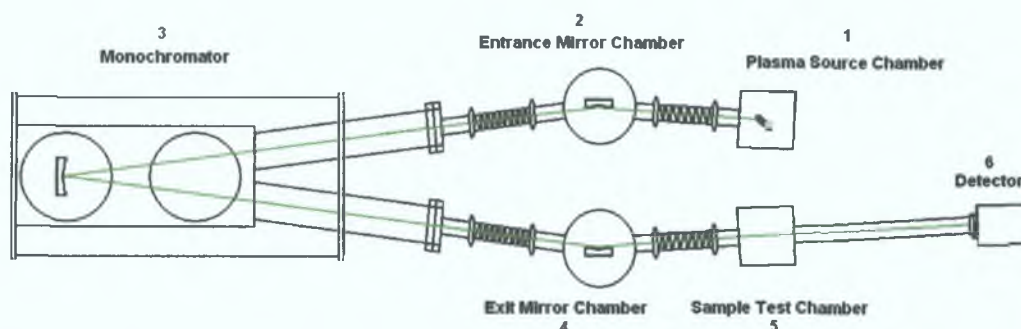


Figure 3-1 The beamline with all the components shown as is in place in the lab

Each of the six sections can be isolated from the other sections by closing gate valves, which are positioned on each connection pipe. Each numbered section in the diagram has its own dedicated pump and the gate valves are located between each of these sections. Parts 1-4 produce the parallel VUV beam, independent of the position or nature of the sample test chamber and the detector. These parts are referred to as the 'beamline'. This design allows for the changing of the sample chamber while keeping the beamline under vacuum as low as 10^{-7} mbar. Its operation is in this respect similar to a synchrotron beam line. Such a facility avoids long down times.

The beam is detected with an Andor Technology DO440 CCD camera attached to the end of the sample test chamber. To reduce the amount of readout noise from the camera it is water-cooled to -40°C .

Each segment of the beamline is presented in detail along with the detector, while the sample test chamber segment will be looked at in section 3.2.

3.1.1 *Plasma Source Chamber*

The plasma source chamber contains the plasma, the light source for the beamline. The chamber is shown in Figure 3-2 and is made from an aluminium cube of side 127mm with 70mm diameter ports in all six faces for the attachment of various windows, pipes and gauges.

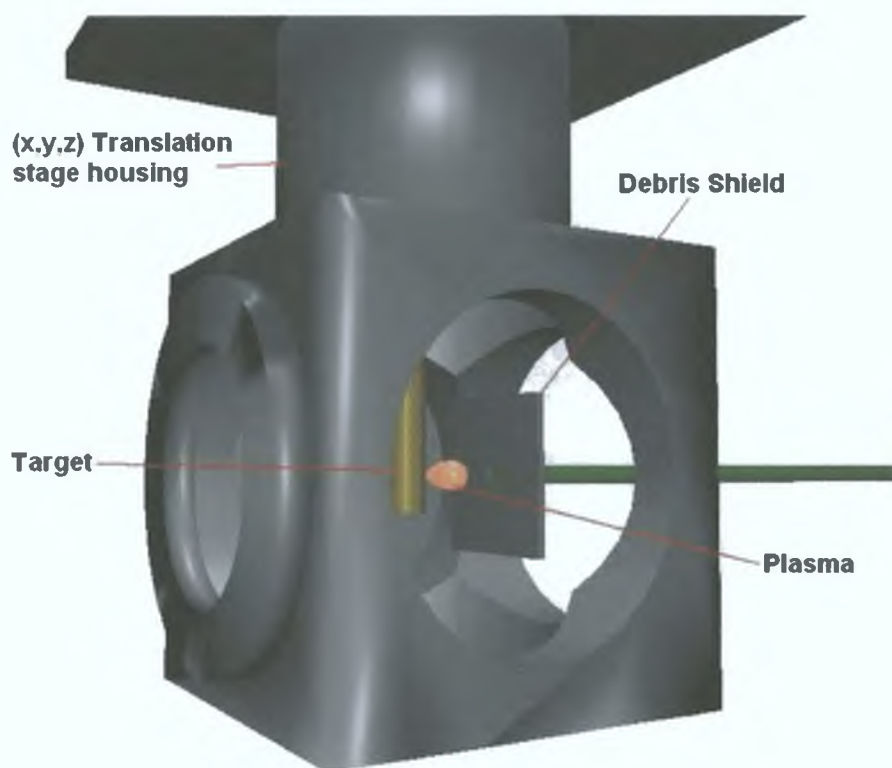


Figure 3-2 Diagram of the Plasma Source chamber in which the main components are shown.

The chamber can be evacuated down to 10^{-5} mbar with the use of a Leybold Pt-50 pumping rig, which is attached onto the base of the cube by a suitable bellows along with Penning and Pirani gauges for high and low vacuum reading respectively (Figure 3-5). The sustainable vacuum pressure (10^{-5} mbar) of this chamber is sufficiently low that the plasma can effectively expand unimpeded by any gas. On the top port is an x,y,z translation stage that is used to manoeuvre the target in the chamber. The target is a 6mm diameter gold rod and needs to be positioned so that the part of the plasma that emits VUV radiation is on the optical axis of the 'beamline'.

The plasma is formed by focusing a laser beam onto the rod using a 30mm diameter lens with a focal length of 100mm. The lens is located outside the chamber, which allows for the quick and easy adjustment of the laser spot size and degree of focusing on the target without the hindrance of using vacuum feedthroughs. As an

added advantage to this set up the lens does not get covered with any debris that is ejected due to the plasma.

The laser used is a 800mJ Nd:YAG continuum Surelite laser with a pulse width of 10ns which must be triggered at a rate of 10 Hertz. Triggering the flashlamps is controlled with a Stanford DG 535 delay generator, which triggers the flashlamps every one hundred milliseconds. The delay generator also sends out a second pulse to the Pockels cell in the laser 180ns after the first pulse (see Figure 3-3a). The Pockels cell is only activated when the Andor control software that operates the CCD camera simultaneously provides a signal. This pulse from the software is sent through an AND gate along with the Pockels cell trigger pulse from the delay generator, see Figure 3-3b.

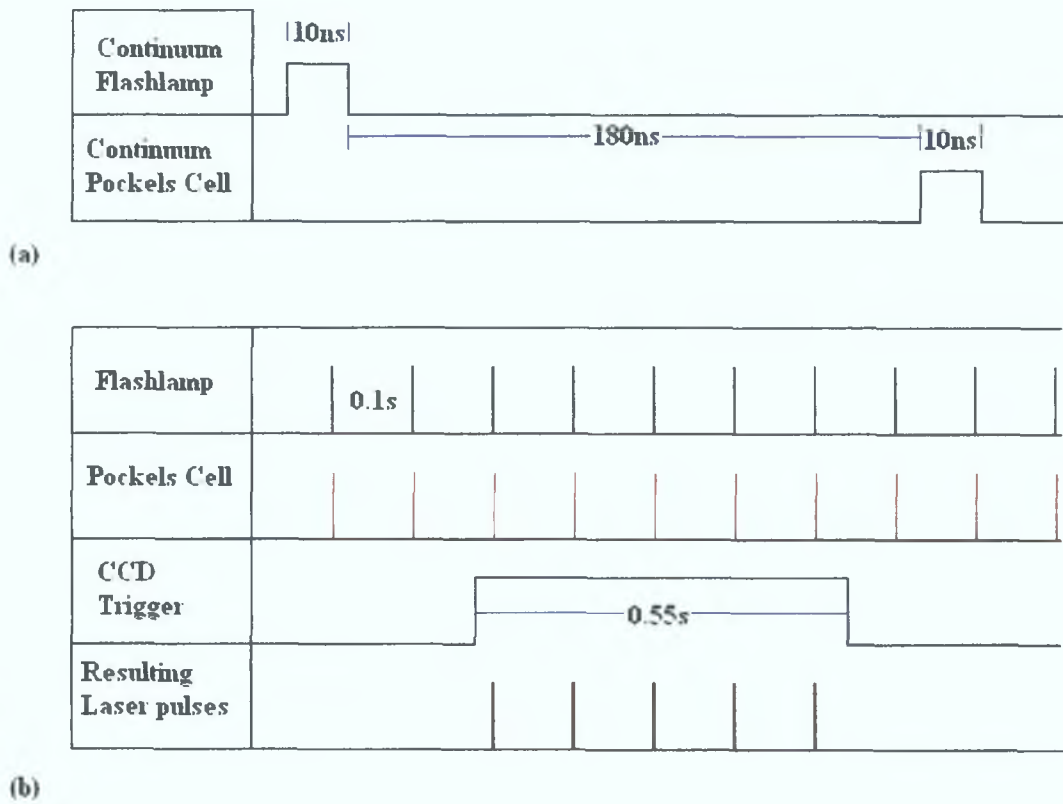


Figure 3-3 (a) The timing between the flashlamps and the Pockels cell. (b) Shows the synchronisation timing between the CCD camera, flashlamps and Pockels cell which result in the laser firing five shots.

This allows for the synchronization of the laser with the camera. The setup of these components can be seen in Figure 3-4.

Figure 3-4 Diagram of the synchronisation setup of the PC, delay generator laser and detector

One problem with using a laser produced plasma as a light source is that the laser pulse ablates material from the target. This affects the position of the light source due to a hole being dug into the target by the laser, this shall be discussed further in section 4.2. The majority of this material that is ablated during the firing of the laser hits the entrance window, which requires replacing or cleaning after a number of experiments. Some of the particles can also pass into the mirror chamber and possibly

coat the mirror there. This problem has been greatly reduced by placing a debris shield at the exit flange of the plasma source chamber and the entrance mirror chamber, the use of a gold target is necessary to reduce the effects of debris on the gold coated mirrors, see Figure 3-2.

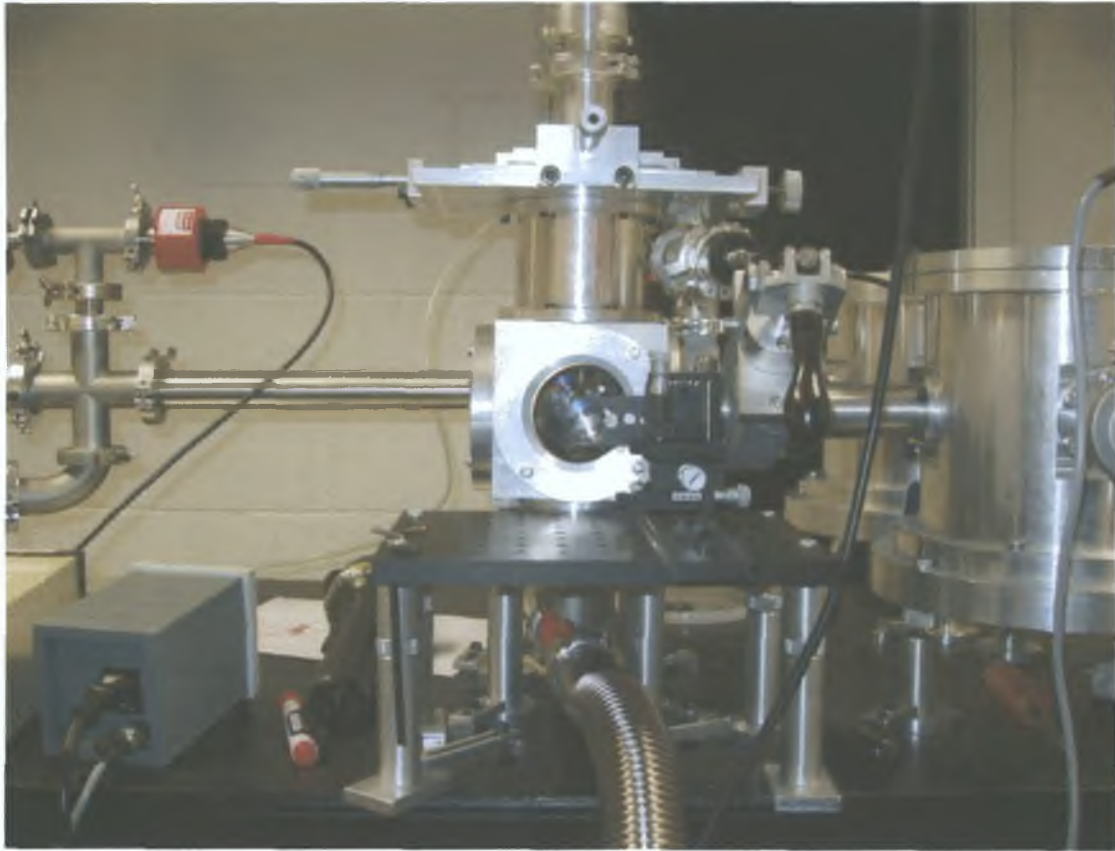


Figure 3-5 Plasma Source Chamber connected onto the rest of the system, with the pipe to the right leading to the mirror chamber. Below the chamber is a bellows connecting the bottom port to the vacuum gauges and the pump.

3.1.2 *The Entrance Mirror Chamber*

The mirror chamber is constructed out of a cylindrical piece of aluminium. It contains four 40mm ports with a secure base plate and a removable top plate. When the top plate is removed the mirror holder contained inside the chamber can be adjusted while keeping the chamber in place. This is normally only done during the initial alignment of the beamline or for essential maintenance. Two ports are on

opposite sides of the cylinder bisecting the chamber while the other two are positioned slightly off centre so that they make a 10° angle with the mirror holder inside the chamber (see Figure 3-6). The location of the mirror is critical to the production of the beam. It is necessary that the entrance mirror be 400mm from the source plasma and 400mm from the entrance slit of the spectrometer in the Rowland configuration. The entrance mirror is toroidal in shape with a tangential radius of 4590mm and a sagittal radius of 35mm. When it is placed at a grazing angle of 85° it stigmatically images the plasma onto the entrance slit. Unfortunately the chamber was manufactured incorrectly in such a way that the required 10° offset for the mirror could not be achieved [44]. This was corrected by adding wedge shaped blocks to where the entrance and exit ports are connected to the chamber. This resulted in changing the angle of the ports and allowed for the 10° offset to be achieved. The plasma could then be imaged onto the entrance slit of the monochromator.

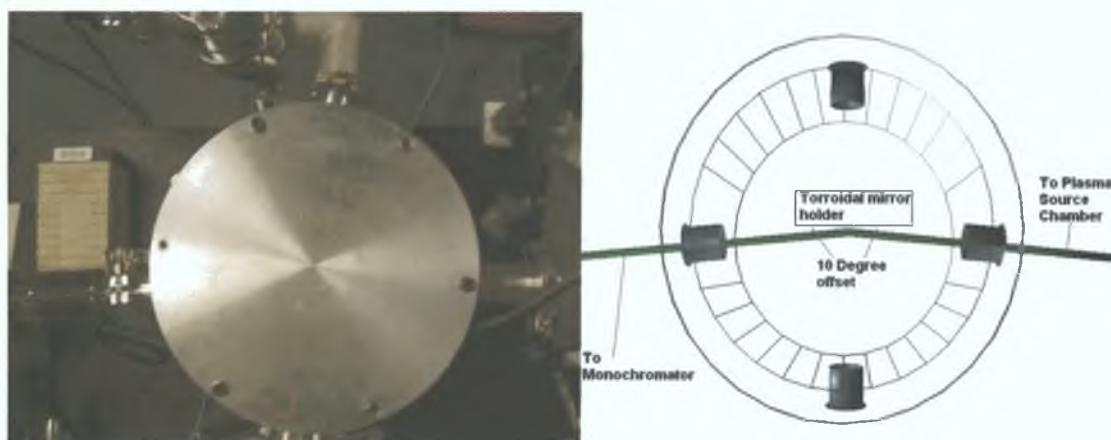


Figure 3-6 Photo and diagram of the entrance mirror chamber. The four ports are visible as is the 10° correction angle required for the mirrors.

3.1.3 *The Monochromator*

The Acton Research Corporation 1 meter normal incidence spectrometer (shown in Figure 3-8) is fitted with an exit slit and is used in a monochromator

configuration. Inside the spectrometer is a spherical concave iridium coated grating with 1200 grooves/mm which is capable of covering a wavelength range of between 30-325nm. Currently it houses a grating blazed for 80nm giving a workable wavelength range from 30-200nm.

The entrance mirror chamber is attached onto the entrance slit adapter with a bellows for ease of alignment. The monochromator takes the light from the entrance slit and directs the required wavelength of light onto the exit slit. Both slits can be changed in width to achieve a smaller bandwidth of light at the expense of light intensity. The resolving power of the beamline was calculated by for a variety of entrance and exit slit widths Figure 3-7 [44]. In the experiments that we carried out we used an entrance slit width of 200μm and an exit slit width of 200μm.

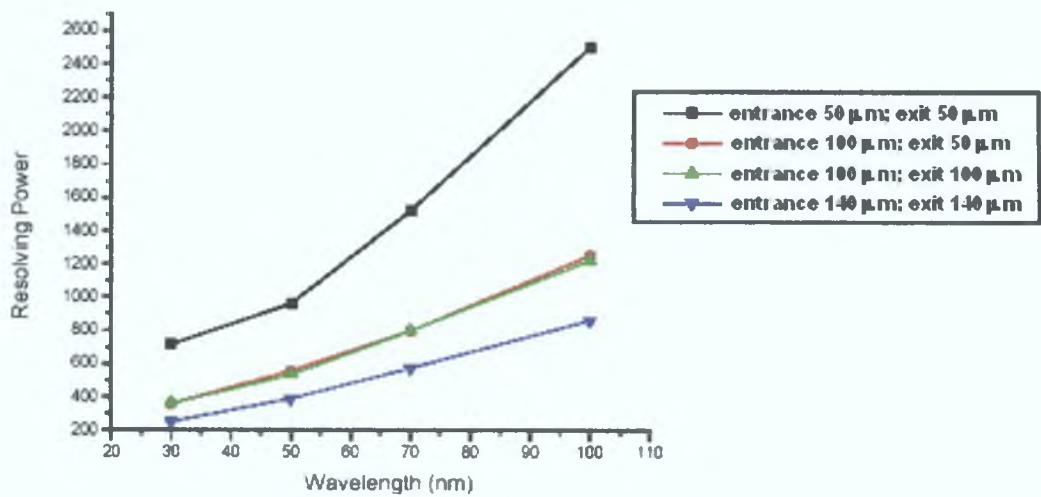


Figure 3-7 Resolving power of monochromator with different slit widths [44]



Figure 3-8 The Acton Research Corporation 1 meter normal incidence spectrometer

3.1.4 *The Exit Mirror Chamber*

The exit mirror chamber is connected to the monochromator with another bellows to facilitate alignment. The exit mirror chamber (Figure 3-9) is of the same design as the entrance mirror chamber and unfortunately also had the same manufacturing flaw. The combination of both corrections resulted in the parallel beam being produced slightly off centre in the exit pipe. This minor problem is counteracted by using a third bellows, which realigns the pipe with the beam. This step ensures that any chambers placed after the mirror chamber can be clamped down in the appropriate position with relation to the beam.

The exit mirror inside the chamber is placed 400mm from the exit slit. Like the entrance mirror, it is toroidal in shape but with a tangential radius of 9180mm and a sagittal radius of 63.5mm. It is placed at a grazing angle of 85° with respect to the

exit slit such that it produces a parallel beam with a 4mm x 4mm footprint. A KF-40 connection allows the attachment of a sample chamber for analysis or a detector for characterising the beam. The beam has a divergence of 0.30 ± 0.01 mrad in the horizontal plane and 0.25 ± 0.01 mrad in the vertical plane [44].

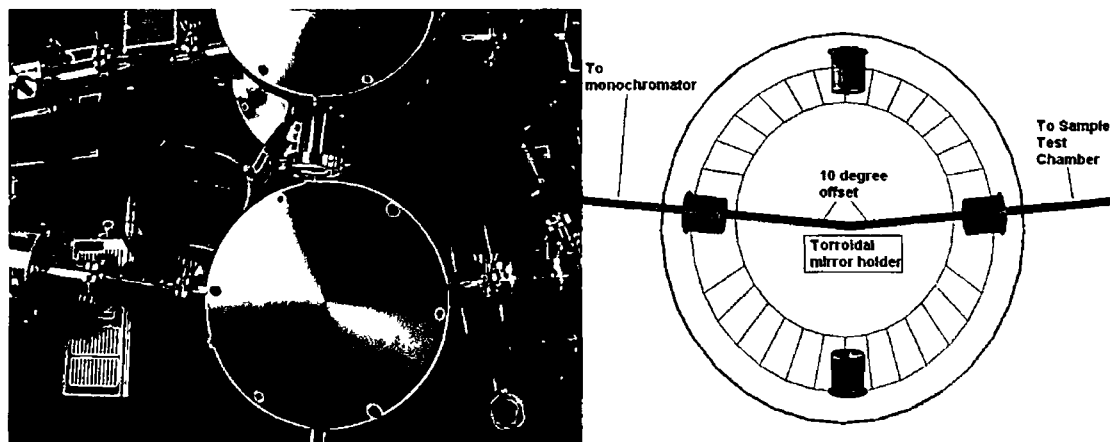


Figure 3-9 Photo and diagram of the exit mirror chamber. The four ports are visible as is the 10° correction angle required for the mirrors.

3.1.5 The CCD Camera

When the VUV beam is produced it passes through a sample test chamber (section 3.2). After passing through this chamber a measurement of the beam has to be made. To measure the amount of light produced by the beamline a suitable detector needs to be used. The Andor Technology DO440 CCD Camera was selected for this purpose and is capable of detecting light in the vacuum ultraviolet (4-40 eV or 31-310 nm) region of the electromagnetic spectrum. It is comprised of 2048×512 $13 \mu\text{m} \times 13 \mu\text{m}$ pixels with a gain (g) of 1.4 and a quantum efficiency (Q_E) of 22% at 50 nm. The quantum efficiency as a function of energy is shown in Figure 3-10.

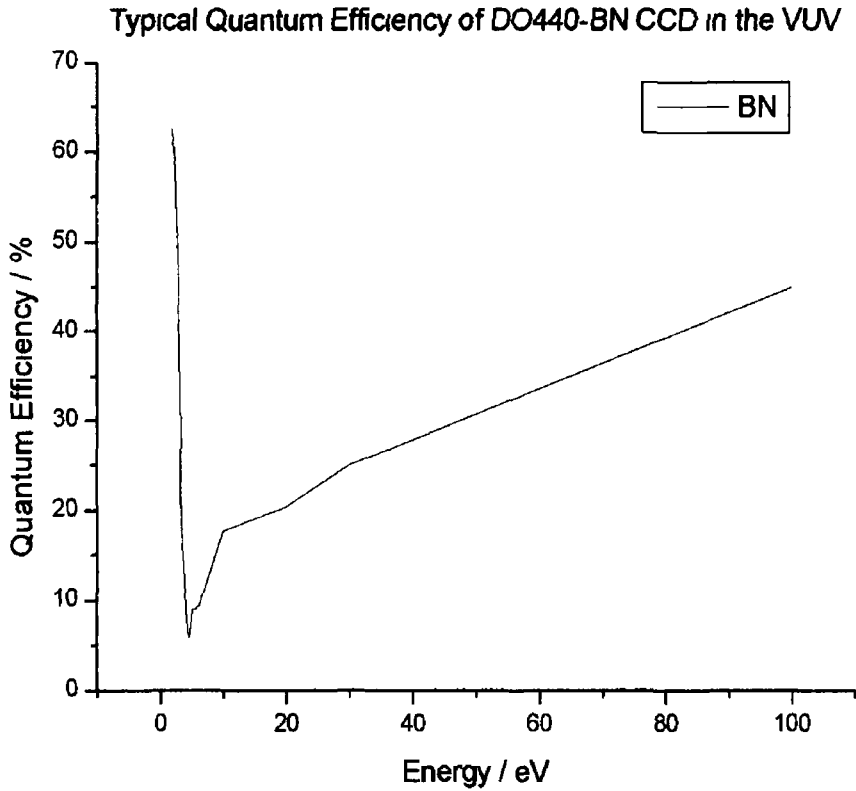


Figure 3-10 Graph of quantum efficiencies as a function of energy From correspondence with Andor see [45]

The number of counts per detected photon (N_C) is given by equation(3.1) [46]

$$N_C = Q_L \frac{E}{3.65g} \quad (3.1)$$

where E is the energy of the incident photon in electron volts. The number 3.65 is a measurement of the energy in eV that is required to create an electron hole pair in a CCD as stated by Poletto [46]

3.2 *Material Analysis Set-up*

The analysis chamber used in this work was designed to analyse the optical properties of windows and thin films in the VUV spectral region. In order to do this kind of analysis two types of experiments can be carried out on materials: reflection measurements off the surface of the material (section 1.3) and transmission

measurements through the material (section 1.4). While the chambers that are needed to carry out these experiments are similar in principle, the physical layout of the detector with relation to the sample is quite different. The basic transmission experiment would be set-up like the schematic in Figure 3-11a, similarly a schematic for reflection is shown in Figure 3-11b and for a combined reflection transmission set-up in Figure 3-11c. Notice that for the set-ups that use reflection we try to ensure a near incident reflection to reduce calculation (see section 2.2.1) and the effects of scattering.

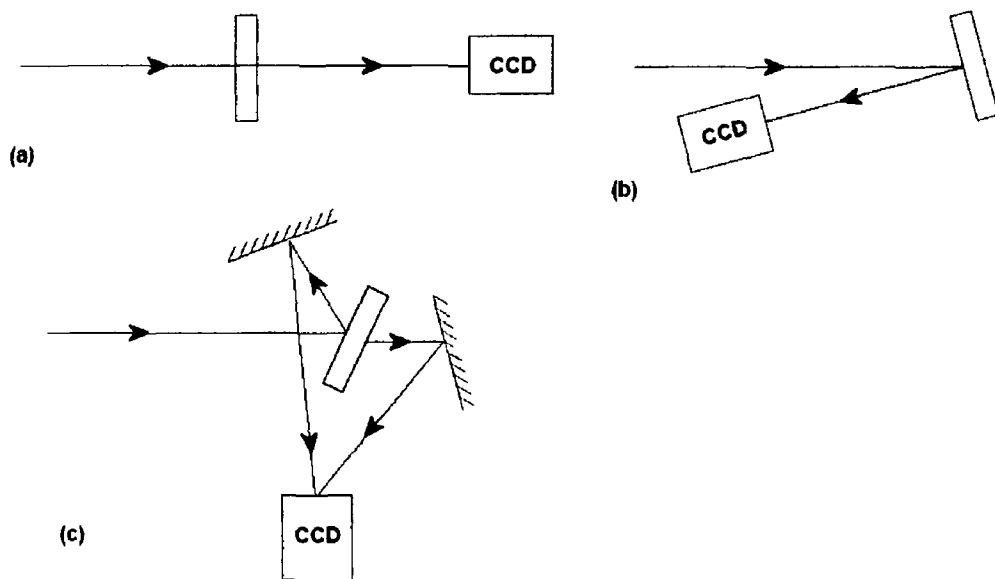


Figure 3-11 Schematic diagrams of possible set-ups of apparatus. (a) is a transmission experiment. (b) is a reflection experiment. (c) is a combined reflection and transmission experiment.

By careful design, all these set-ups can be housed inside one vacuum chamber. Having more than one chamber not only adds additional cost, but also means that there will be a significant amount of down time due to swapping of large vacuum chambers. Whenever a chamber is to be removed from the system it must be brought up to atmospheric pressure, and the chamber that replaces it must be carefully realigned and pumped down.

With these schematics in mind three chambers were initially designed and all the optical mounts for these two chambers built so that the migration into a single chamber could be easily done. A detailed discussion of the initial designs for each of the three types of experiments will be shown along with the concept of how to merge the designs into a single chamber (see section 3.2.1). This final chamber configuration is shown with specific detail given for the changes that are required to modify the chamber for the three types of experiments.

3.2.1 *Initial Chamber Designs*

The initial design of the chambers was kept as simple as possible. Each chamber had to have a KF-40 adaptor flange to connect onto the pipe coming from the exit mirror chamber and a place to mount the CCD camera for detection of the beam, the positioning of which depends on the experiment. Once this is achieved the specific experimental requirements come into play.

The transmission experiment is a simple one where a material is placed in the path of the beam and the reduction in intensity of the beam gives the transmission of the material in question. The main design issue lies with the material sample holder. This holder needs to be able to securely hold a window or film, which must be suspended without movement inside the chamber. It also had to be manoeuvrable under vacuum to allow for the holder to be taken in and out of the VUV beam. This ensures that the incoming beam intensity can be measured without any unwanted material absorbing the light. Such requirements led us to a simple chamber with a connection pipe at one end, an arm mounted on the top of the chamber to lift up and

down the sample holder and a connection for the camera at the back of the chamber as shown in Figure 3-12.

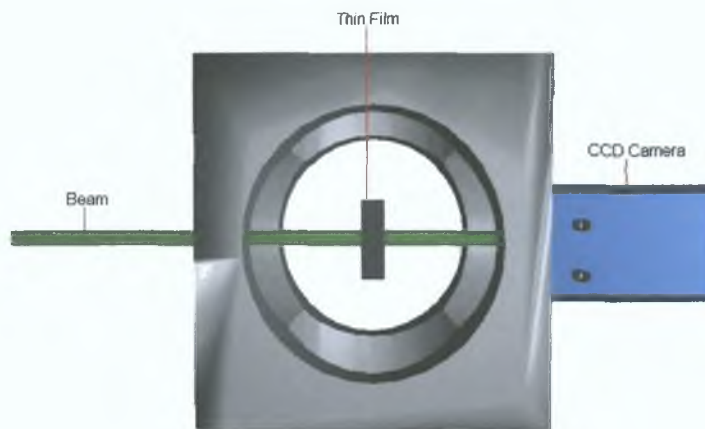


Figure 3-12 Initial design for transmission experiment chamber

This design provides a straightforward method to get absorption measurements by taking an incoming measurement, lowering the sample into the optical axis of the beamline before taking a transmission measurement. The basic design shown in Figure 3-11b was then transferred to a large chamber. It is then possible to introduce the combined reflection transmission style experiment (Figure 3-11c) into this large chamber as described below in section 3.2.4.

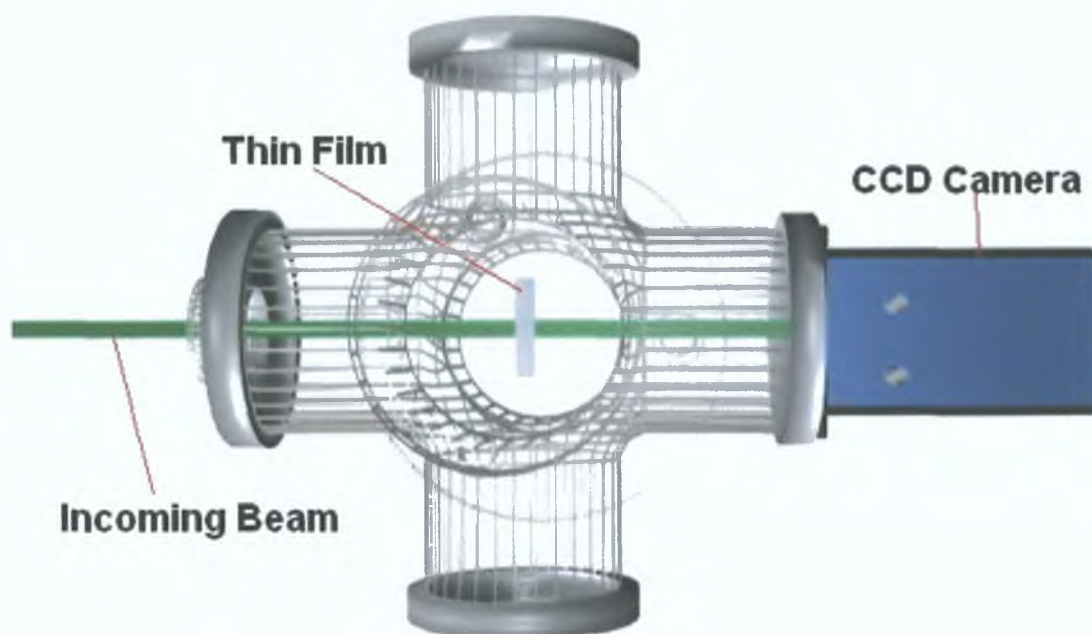


Figure 3-13 Implementation of the transmission set-up inside the six-way cross

The chamber used for this purpose is a steel six-way cross, made up of three 100mm diameter pipes all perpendicular to each other (Figure 3-13). Each of the six ends has a Contra Flat 100mm vacuum connection (CF-100). This six-way cross was supported by an adjustable stand, designed specifically for this chamber, which allowed for its orientation to be altered during alignment. To comply with the initial requirements mentioned above the chamber was fitted with a KF-40 to CF-100 adaptor attached onto the front of the chamber for connecting to the beamline. At the back end of the cross a CF-100 blank was adapted so that the CCD camera could be mounted onto the chamber.

The sample holder is attached to a retractable rod from the top of the chamber, which allows for the movement of the sample into and out of the beam. This sample holder system is comprised of four parts: a smooth steel rod, a Balzers vacuum feedthrough, a KF-40 to CF-100 adaptor and the sample holder. The steel rod on which the sample holder is attached (see Figure 3-15) can be manoeuvred in and out

of the beam with the use of a vacuum feedthrough, which is connected to the chamber through a KF-40 connection. The sample holder is designed to hold discs with a diameter of 25mm and of varying thickness, as shown in Figure 3-14.

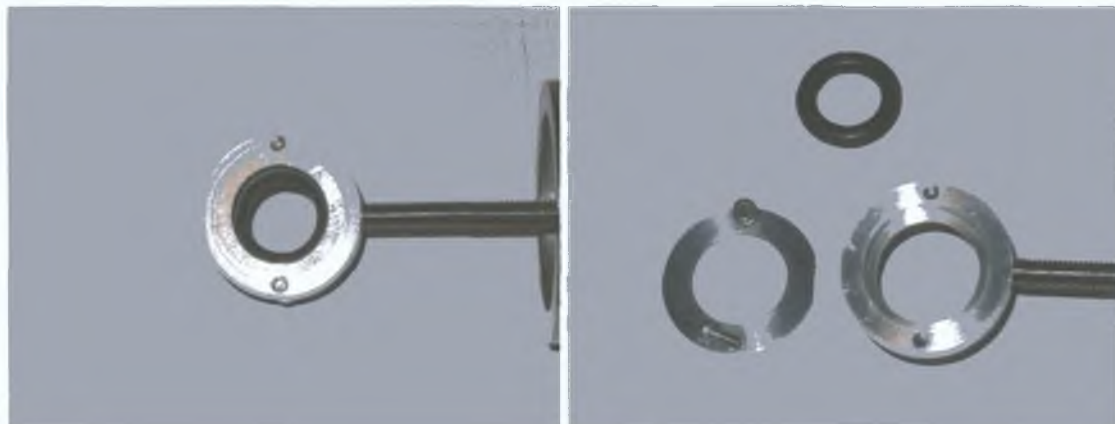


Figure 3-14 Pictures of the sample holder used for the lithium fluoride filters, calcium fluoride windows and the aluminium thin films.



Figure 3-15 Pictures of the sample holder used inside the cross with the gold mirror in place for use in the reflection experiments.

The advantage of this chamber over a simple cube chamber is the sheer size of the internal structure with the possibility of expanding through the other ports.

The reflection experiment however is not as simple in design as the transmission experiment was. For this experiment it is desirable to have near normal incident reflection off the surface of the sample. The Fresnel equations (see section 2.2.1) allow, in principle, the determination of the optical constants at any angle of incidence, but the analysis is greatly simplified if near normal incidence can be assumed. This led to the need for a chamber with the entrance and exit ports at the

front of the chamber. To this end a CF-100 flange fitted with two pipes entering the front of the chamber forming a V-shape was used. The thin film must then be located at the intersection of the two axes through the entrance, and exit pipes.

Such a chamber had been designed and built before, in the form of a 100 millimetre diameter T-piece shaped chamber with CF-100 vacuum connections similar in size to the six-way cross. The flanges on this T-piece included a V-shaped flange as described above, and a sample holder with adjustable orientation. The reflected beam leaving the chamber through the exit port at the front would come in contact with the CCD Camera attached to the exit port (see Figure 3-16).

Implementation of such a design would require the sample holder to be located at the back of the chamber.

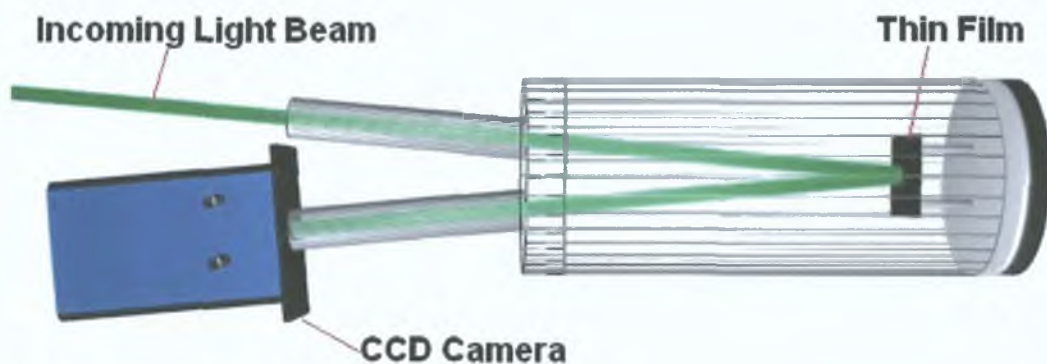


Figure 3-16 Diagram of initial design of reflection chamber. It is very similar to the actual chamber that was used

The similarities between both initial transmission and reflection chambers allowed for the possibility of combining the major elements of both into the six-way cross. This was made possible with the use of two different types of flanges placed at the front of the chamber. Such a combined design raised other issues that must be addressed for each experiment.

3.2.2 Reflection Chamber Configuration

The main components of the original reflection chamber were an adjustable sample holder and the front flange containing the two pipes. The front flange could be easily fitted to the six-way cross that is used for the transmission experiments, as the vacuum connections and diameter of the flange were identical to those of the cross. With the front flange attached to the front of the chamber the location where the two axes converge could be calculated, this is where the sample should be positioned.

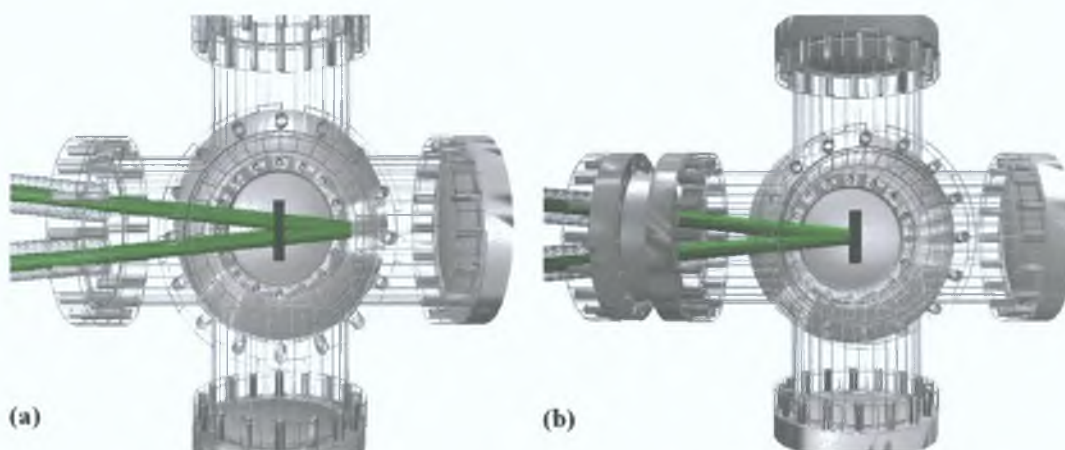


Figure 3-17 (a) Diagram of the reflection flange directly attached onto the sample chamber, it shows the ideal position of the sample where the two beams converge. As opposed to where the sample actually is. (b) Diagram of the reflection flange attached onto the cross fitted with an extension pipe. The ideal position of the sample now converges with the position of the sample in the chamber.

The orientation adjustable sample holder mentioned above was placed at the back of the chamber to reflect the beam through the exit pipe. However, due to the design of this holder we could only move the sample further into the chamber by a small amount. We were also unable to move the holder out of the beam to allow for the measurement of the incoming beam intensity by either direct measurement or by using a calibrated mirror to reflect the beam. Positioning the holder at the top of the chamber in a similar way to the transmission sample holder was fruitless. Thus the possibility of using the sample holder for transmission experiments was considered,

however it was located in the centre of the chamber which is too close to the front port to be useful for reflection experiments (see Figure 3-17a) The position of the sample holder for reflection would need to be 74mm further to the back of the chamber In order to use the same sample holder for both experiments two possible solutions presented themselves The first was to fabricate a new front flange whose entrance and exit pipes were set at a greater angle Such a fabrication would not be easy The second option was to extend the front section of the chamber with an extension pipe This was the solution of choice as it meant buying an inexpensive component The extension pipe that was purchased was 74mm in length and could be fitted onto the front of the chamber Thus the distance between the v-shaped flange and the sample holder was identical to that of the old chamber shown in Figure 3-17b

In order to measure both the incoming and reflected intensities with this configuration (Figure 3-18) two cameras could be used camera #1 is used to record the incoming beam, and camera #2 is to record the reflected beam When taking measurements with two cameras the quantum efficiency of each must be taken into account when carrying out the analysis This ensures that a correct reading is being taken To further ensure the accuracy of such a system the cameras should be swapped around and the experiment repeated However, if only one camera was available a calibrated gold mirror could be placed above the sample in a specially designed mirror holder, which will reflect light through the exit pipe This mirror would be calibrated for all wavelengths being used prior to carrying out an experiment Such a holder to mount the mirror is shown in Figure 3-15

With this design we achieved a single versatile chamber for use with reflection and transmission experiments Section 3.2.3 shows the final design of the chamber in

a transmission configuration. Section 3.2.4 describes how the chamber can also be used for a combined reflection and transmission experiment.

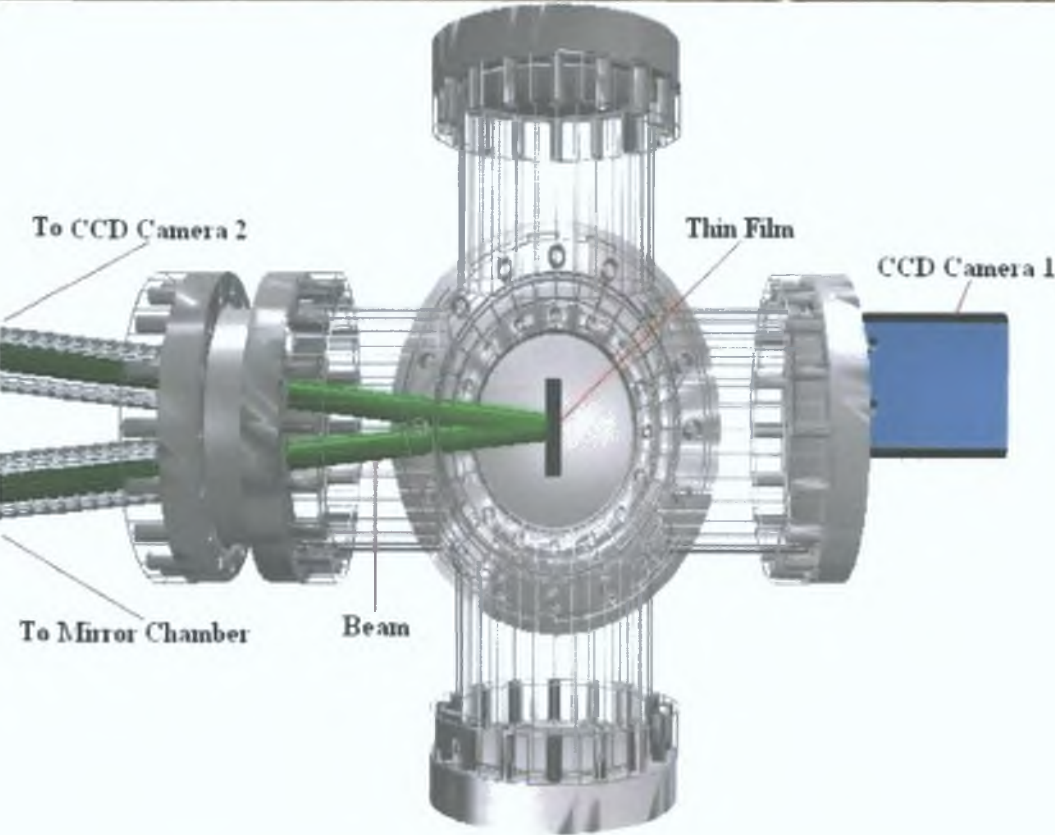
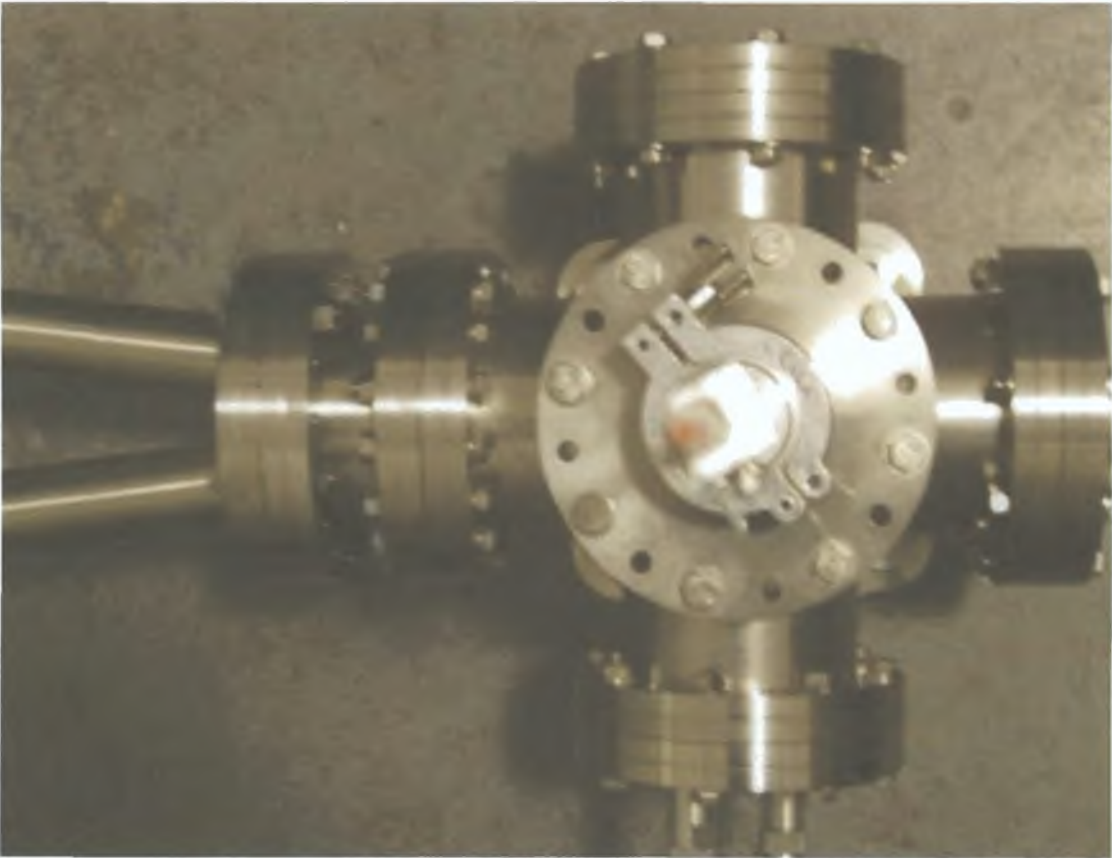


Figure 3-18 Picture and diagram of the reflection chamber configuration

3.2.3 *Transmission Chamber Configuration*

The final configuration of the transmission chamber did not change much from the original design implementation. That design employed a large volume six-way cross with a sample holder in the centre. Full details of this chamber can be found in section 3.2.1. The only minor difference from the original is the addition of the extra piece of pipe at the front of the chamber and a KF-40 connection at the back so that the camera can be isolated from the system with a valve. The reason for the extra section of pipe is explained in section 3.2.2. The valve was included as some water vapour was entering the system when the rod was being lowered into the chamber. This caused a small amount of ice to form on the camera head when it was cooled down to -40°C . The final configuration can be seen in Figure 3-19.

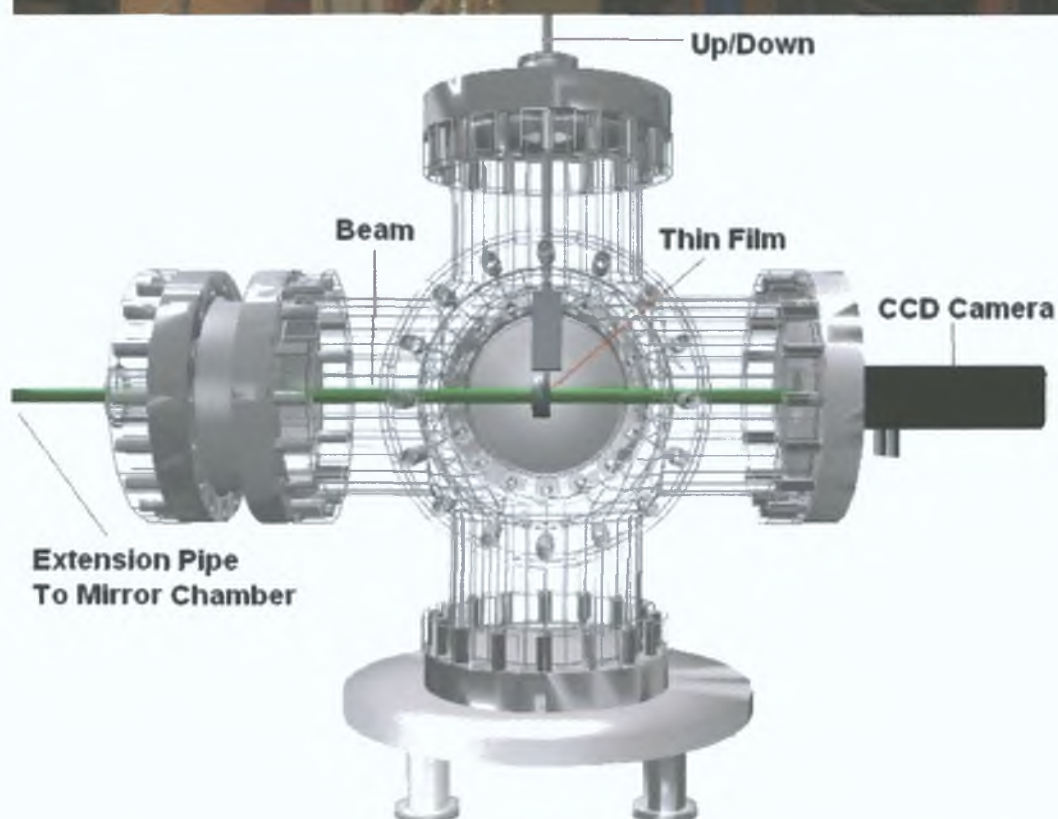


Figure 3-19 Picture and diagram of the analysis chamber used for transmission experiments. The extension pipe connection is clearly visible on the left of the chamber to the mirror chamber and to the vacuum pump and gauges. The metal rod used to raise and lower the sample can be seen at the top. The diagram represents what is happening inside the chamber during a transmission experiment. The picture was taken before the introduction of the valve to protect the CCD from water vapour buildup, this is located between the CCD and the right exit flange of the six-way cross.

3.2.4 Reflection/Transmission Chamber

Configuration

With the combination of both the reflection and transmission experiments into one chamber we investigated the possibility of a configuration that would allow for both reflection and transmission to be measured simultaneously with one camera. This is done with the use of high quality gold mirrors, which redirect both beams onto the camera mounted onto the side of the chamber. Both mirrors require to be positioned at two locations and also needed to be slightly manoeuvrable so that fine adjustments could be made. This ensured the reflection from each mirror would strike the camera. One mirror was placed at the back of the chamber on a wedge-shaped holder (Figure 3-20b).

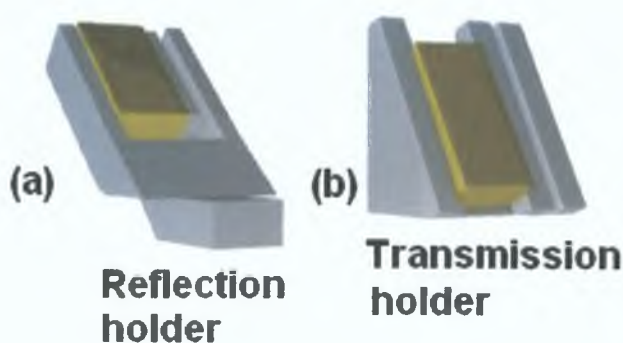


Figure 3-20 (a) Diagram of the mirror holder used to redirect the beam reflected off the sample. The block at the bottom of the holder is used to clamp the holder in position. (b) Diagram of the mirror holder used to redirect the beam transmitted through the sample. See Figure 3-21 for location of the holders in the chamber.

The angle of the wedge was calculated so that the 4mm square beam after transmission through the sample could pass by the sample holder and the side of the chamber and strike one side of the camera without obstruction. This mirror was also used to redirect the incoming beam when the sample was out of path of the beam.

The other mirror would have the sole purpose of directing the reflected beam from the sample surface onto the other side of the camera. The holder for this was set at an obtuse angle with its end pointing towards the front of the chamber as shown in Figure 3-20a. Once again the ideal position of the mirror in this holder was calculated before its construction. This positioning of both mirrors is shown in Figure 3-21.

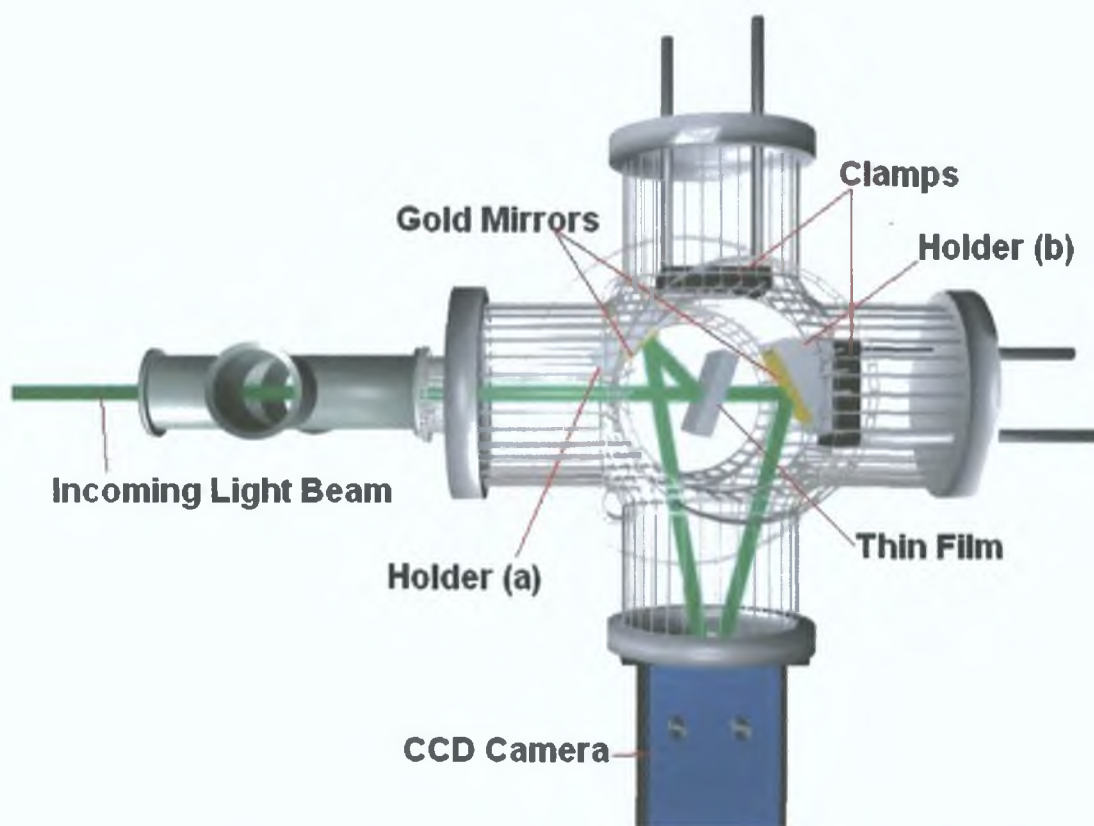


Figure 3-21 3D representation of the Reflection Transmission Chamber showing how the light is redirected to the CCD camera using both mirrors.

The locations of both mirrors inside the chamber were tested on a mock up of the chamber using a laser diode, some foam models and some mirrors before the actual holders were constructed. When the holders were made the angles were once again

checked using a laser diode. These holders were placed in the chamber and secured by two clamps whose orientation could be changed by using two vacuum feedthroughs per clamp. The angles that the transmitted and reflected beams come in contact with the CCD is known and therefore can be corrected for by using a simple $\cos(\theta)$ angle correction formula. Upon application the program that was written had to lengthen the image by weighting each pixel and reassigning counts to the new stretched image to obtain the image at a 0° angle the program can be found in Appendix A.

This set-up was tested further with a proof-of-principle experiment using a visible spectrometer and a magnesium lamp as the light source. An image taken during the testing phase can be seen in Figure 3-22. The image shows a combined transmission and reflection image on the CCD. In order to get an incident image of the beam the sample is simply raised out of the beam. This allows the incident beam to be reflected onto the CCD using the transmission mirror at the back of the chamber (holder b in Figure 3-21). It must also be noted the opposite angle of the slopes in the binned image. This effect is due to the transmission having one reflection and thus the image is reversed, and the reflected image is in fact undergoing two reflections and so is now the same orientation as the incident light as it strikes the transmission mirror.

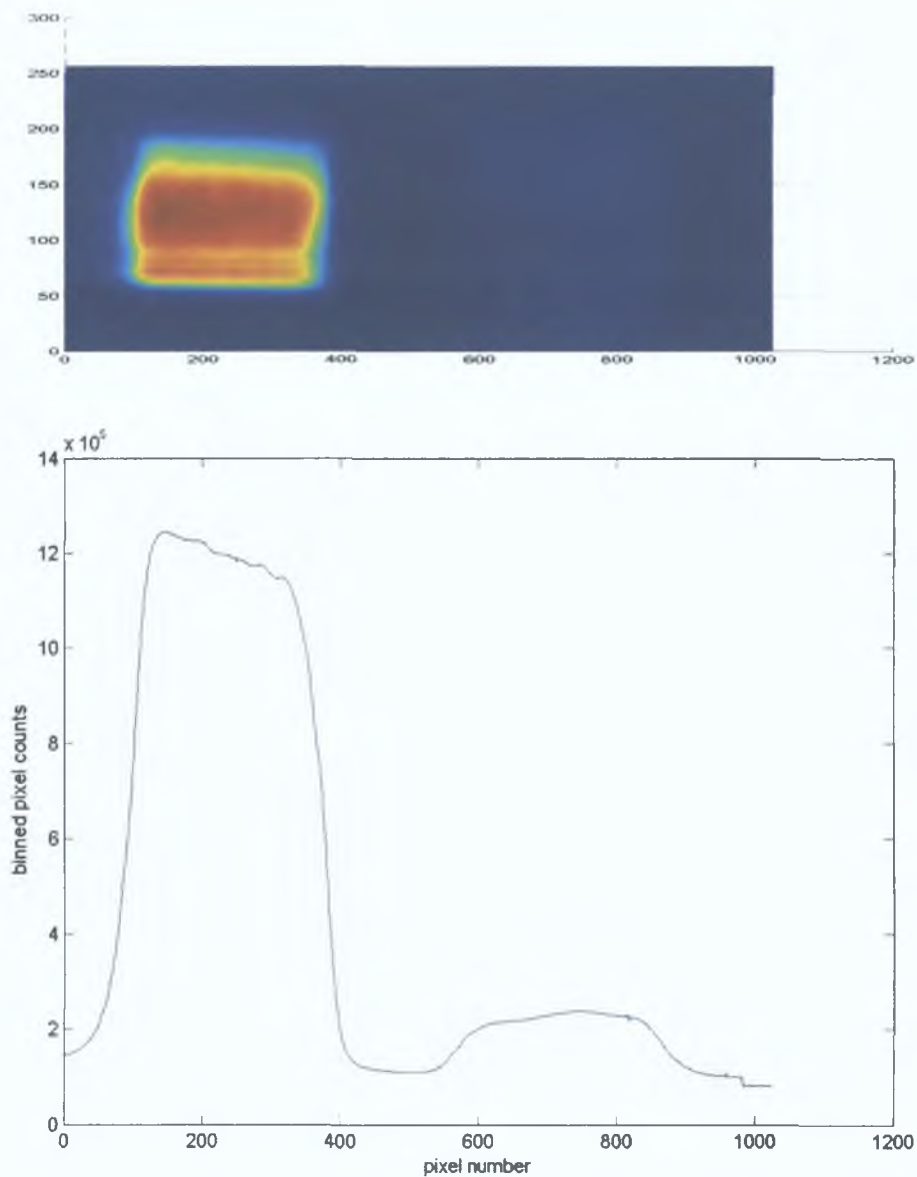


Figure 3-22 The top image shows the reflected and transmitted light taken during the testing of the combined reflection transmission set-up with a visible spectrometer and a light bulb. The left hand side shows the reflected beam while on the right is the transmitted beam. The bottom graph is a graph of all the vertical pixels in the image summed together. The difference in intensity of both reflected and transmitted beams is most easily seen in the bottom graph.

3.3 Filters

With all of the experiments it was necessary to employ a wavelength filter in order to remove any second order light from the incoming beam. This problem was

especially severe in the region above 50nm. The need for this became apparent during experiments with calcium fluoride (see section 5.2 for details). Suitable filters had to be found for all the wavelengths that were going to be used. Lithium fluoride was an appropriate filter for use at the high wavelength end as its transmission cut off is about 104nm. With this filter in place it ensured that the region from 110-200nm was free from second order light. The lithium fluoride window was mounted in a holder (Figure 3-14) and placed on the end of a retractable arm, so that the window could be taken out of the beam when operating at wavelengths below the lithium fluoride cut off.

At lower wavelengths other filters are required, however, no single free standing filter was found that worked well in the region, hence we used noble gases. From 80nm argon can be used as a filter and from 50-80nm helium can be used. At wavelengths below 50nm it was not necessary to use a filter as the 25nm second order light is not distinguishable from the background and would not affect the measurements. The gas was fed in through a needle valve just after the exit mirror chamber close to a set of vacuum gauges. More details about each of these filters and their use can be found in section 5.3.

3.4 *Creation of thin films*

A major part of the experiments was carried out on films of aluminium from 10-40 nm thick. Such experiments allowed us to further test and refine both the experimental and the analysis systems, while at the same time provided us with data for calculating the mass absorption coefficient of aluminium. These aluminium films are so thin that it is necessary to support them with copper mesh grids details of which

can be found in Table 3-1. A representation of the 200 grid used for all films can be seen in Figure 3-23. Without these grids the films would not be able to stand freely during the experiments.

Table 3-1 Details of the Transmission Electron microscope grids used

Grid Title	Mesh μm	Hole μm	bar μm
New 100	100	230	12+ 30
New 200	200	100 x 100	20+30



Figure 3-23 Representation of the new 200 mesh grid used to support the aluminium thin films with details of both bar thicknesses and the hole clearly shown

The grids were themselves mounted onto aluminium holders, which were 25mm in diameter with a 2mm diameter hole in the centre; the grids are glued onto the rim of this hole with araldite.

The films are created using an Edwards auto 306 vacuum coater (Figure 3-24). This is a bell jar glass chamber that is pumped down with a diffusion pumping system. Inside it houses a rotateable stage, a deposition shield to block any material being deposited onto the sample until the optimum deposition conditions are satisfied, and an Edwards FTM5 thickness monitor.

The thickness monitor is suspended above the evaporating elements and it houses a driven quartz crystal whose oscillations are monitored during the deposition. The frequency of the crystal decreases as material is deposited onto the crystal. This variation in frequency is noted and allows for the thickness to be calculated as explained in section 4.4.1.1. This evaporator evaporated high purity (99.999%) aluminium wire onto cleaved sodium chloride crystals, which were stuck onto glass microscope slides. Each crystal is approximately 4mm long and 2.5mm wide, which gave us 0.5mm extra to cover the grid. Once the aluminium was deposited onto the crystals they were removed one at a time by slowly immersing the slide into a bath of warm water. The sodium chloride was quickly dissolved allowing the film to float off the surface of the crystal. This method of removing the aluminium works quite effectively. Once the aluminium is removed it is a tricky job to scoop up the film onto the holder, it is especially difficult to ensure that the film fully covers the grid at the centre.



Figure 3-24 Edwards Auto 306 vacuum coater

The films are then left to oxidise for three days so that a consistent layer of aluminium oxide would form on all the films. The reason for this is so that each film would have the same thickness of oxide on the surface that could be accounted for (see section 4.4.2). As aluminium oxide is a very strong absorber of VUV radiation, failure to take its presence into account would result in a false measurement of the transmission and lead to overestimating the value of the absorption coefficient see [19].

The data that is measured from the experimental configurations mentioned in chapter 3 needs to be analysed in such a way that as much information is extracted as is possible. During the experiments, images are recorded in a definite sequence. First an incoming beam measurement is needed followed by either a reflection or transmission measurement and finishing with an incoming measurement. An example of a typical sequence is displayed in Figure 4-1.

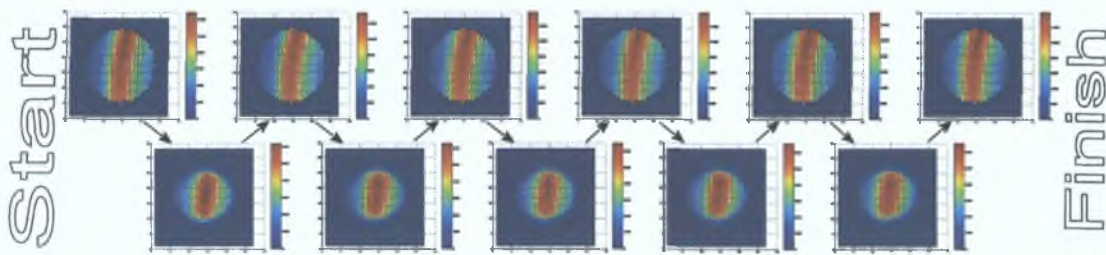


Figure 4-1 Sample experimental sequence, with time increasing from left to right. The top line is the incoming beam after alignment while the bottom line is a transmission through a 2mm aperture.

The reason for this sequence is that the incoming beam cannot be measured at the same time as the other measurement. Fortunately the beam does not change much between measurements. This allowed us to estimate a value for the incoming beam during a reflection/transmission measurement by interpolating the incoming beam taken before and after each measurement.

This technique was verified by recording seven incoming images (as opposed to the eleven images in Figure 4-1) each generated with five shots from the laser. Each image was assigned a number from 1-7 in order of when the image was taken. The even numbered images were treated as the transmission measurements. The odd incoming beam images were then interpolated to generate images that correspond to

what the incoming beam would have looked like when the transmission images were recorded. The average counts on each image were then calculated for all the images. The close agreement between interpolated and measured counts is shown in Figure 4-2.

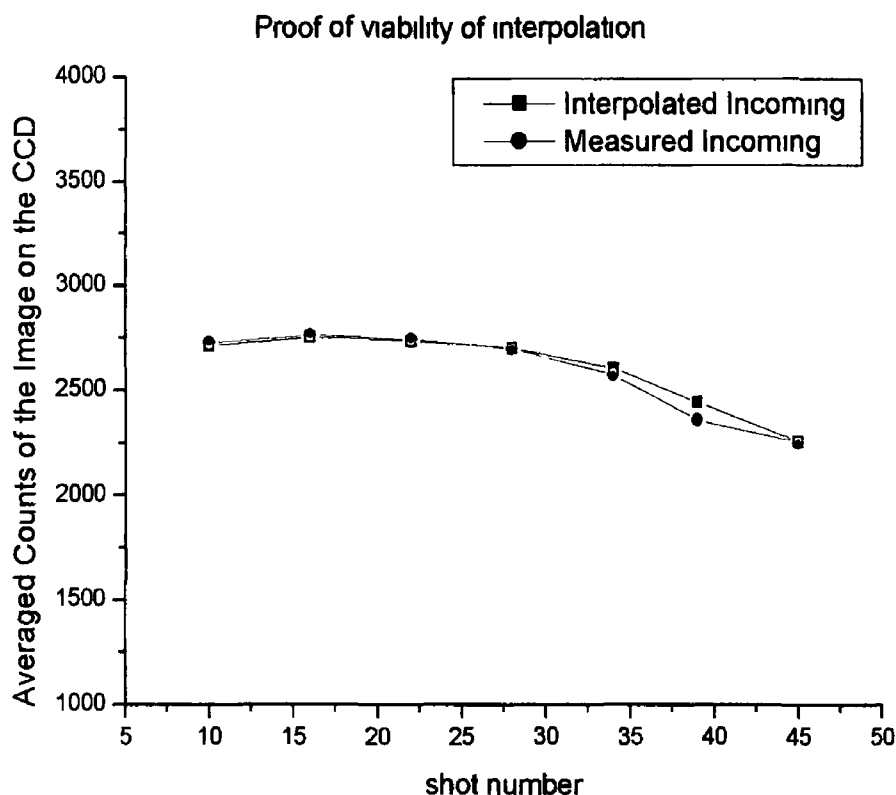


Figure 4-2 This graph shows what occurs during normal interpolation. The largest error in the interpolated incoming count is about 3%.

The images are recorded with a CCD camera that can output two types of files: a single array of numbers (plot) that is associated with all the vertical pixels in the camera being binned into one row and a two dimensional array (image), whose pixels can be binned up to 64x64 pixels generating a so called 'superpixel' array. The reason for using these two file types is explained in section 4.1. The analysis program is able to deal with both types of files as well as the other necessities of the reflection and transmission analysis. A complete analysis includes aligning all the images,

eliminating pixels that are outside the beam, finding out the percentage reflectance or transmission and using this data to calculate the optical constants of the material held in the sample holder

This chapter discusses all the elements that are needed to fully analyse the data. It commences with how the data from the CCD is put into a form that can be used in the analysis programs. Once in this form all the images can be aligned, so that they can be used to find the percentage reflection and transmission of the samples. The sample thicknesses are also measured using three independent techniques: a thickness monitor (during deposition), profilometry and atomic force microscopy. These measurements will be used in conjunction with the percentage transmission to obtain the absorption coefficient of aluminium in the VUV region.

The percentage reflection measurements can be used in conjunction with available data from the literature to obtain optical constants using a Kramers Kronig analysis. It is also shown how optical sum rules can be used to verify and improve on these calculated values.

4.1 *Processing Data from the CCD Camera*

As mentioned above the camera can output two types of files that are useful for our measurements. The type chosen depends on the intensity of the incident, transmitted and reflected beams. When taking measurements at wavelengths higher than 100nm the counts per pixel are very low, in this case a process known as 'full vertical binning' must be used to achieve a good signal-to-noise ratio. Full vertical binning is a process where all the vertical columns on the CCD chip are added

together before being sent to the software, which reduces the amount of transmission noise and produces a one dimensional array or plot

At lower wavelengths, down to 30nm the counts per pixel are greater due to the light intensities produced by the plasma. Thus an image with a number of binned pixels can be used to maintain the counts per 'superpixel' (a term used for the sum of binned pixels) well above the level of the noise

All images from the camera, whether they are a plot or an image, are saved to files with an 'sif' extension. These files are encoded in binary format and have to be converted to the ASCII format. In this new form they can be loaded into Mathworks Matlab®. Matlab was chosen to analyse the data as it can deal with large arrays of numbers with ease and can also produce three-dimensional views of these large arrays. Figure 4-3 shows a chart representing the way the analysis is carried out where the main parts are the image alignment, the interpolation and getting the ratio of the transmission/incoming images. All of these shall be described in detail below

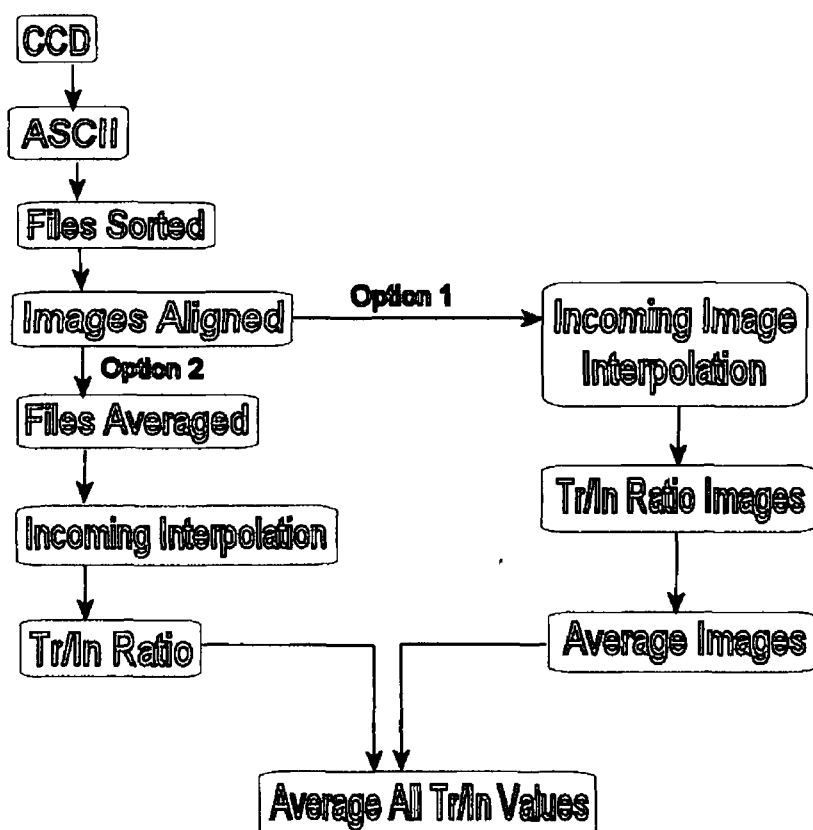


Figure 4-3 Flow chart outlining the analysis procedure with both analysis options shown

As can be seen in Figure 4-3 above, there are two possible options to take after the images are aligned. Option 1 includes a much greater number of calculations, as it requires the interpolation of full images while option 2 only interpolates the averaged counts over the entire image. Option 1 should be taken if the structure of the image plays a significant role in the analysis, whereas option two should be taken if only the average intensity of the images is required. For the analysis here option 2 was chosen. All of the steps in the analysis set out by the diagram including both options described below.

To aid with the conversion to ASCII, the Andor software that operates the camera contains a batch converter, which converts a list of image files to the ASCII format. When using this converter there are options to export the signal, background and reference parts of the data, the signal and background files must also be outputted

When all the files are converted to the ASCII format, a file list must be generated. This list should contain the directory location on the first line and the filenames on the subsequent lines. Further details on this and the sorting of the files can be found in Appendix A. After sorting the files into their appropriate directories we must then carry out the first major step in the analysis, the alignment of all the images.

4.2 *Image Alignment*

Image alignment is a necessity, as the beam tends to drift across the CCD during an experiment. The drift is usually only a fraction of a pixel between successive shots, but after 50 shots on the target the drift is noticeable even when comparing superpixel images. The reason for the drift is that the laser digs a small pit into the target with every shot, and each data set typically requires around fifty laser shots for one transmission or reflection data point. After recording a data set the target is moved to allow a fresh part of the gold target to be available as the target for the next set of measurements. The gold target (used in creating the plasma that emits continuum light) is positioned at a certain distance from the optical axis of the beam so that during the first shot the light emitted on the optic axis at the required wavelength is maximised. As each image is taken, the laser digs a deeper pit into the target. This results in a slight change in the position of the plasma with respect to the optical axis of the beam. This slight change in the distance of the target surface from the lens results in the degree of focussing of the lens changing slightly. This alters the spatial and temporal behaviour of the plasma. The light emitted now hits different parts of the toroidal mirrors and the grating in the monochromator.

This not only causes the beam to drift but also affects its intensity for a number of reasons. Firstly, there is less emission of the selected wavelength from the plasma in the optical axis, secondly, the reflectivity of the gold mirrors and iridium coated grating is dependent on the angle of incidence, and thirdly different superpixels on the CCD are illuminated which tend to have different quantum efficiencies. It is important to correct for this drift not least because during experiments with aluminium thin films, the film only has a diameter of 2mm while the beam has a 4mm x 4mm footprint this means that only a small section of the beam is recorded during a transmission. Aligning all the images to less than a superpixel compensates for the drift and dramatically improves the accuracy by reducing the associated errors with the final result.

Before any alignment is done, the signal-to-noise ratio of the camera must be calculated for each wavelength. This ratio is taken to be 3:1 like in astronomical circles [47]. With this ratio the signal can be extracted reliably at those values that are more than three times the value of the noise. The readout noise from the Andor CCD chip is about 5 electrons [46]. The number of photons corresponding to this number of electrons can be calculated by dividing the number of electrons by the quantum efficiency of the chip at the energy of the incoming photons. For example the camera we use has a quantum efficiency of 0.197 for 16.9eV photons, so the number of these photons that would generate the number of electrons that contribute to the noise is $5/0.197=25.35$. This number of photons can then be converted to counts when knowing that the camera is set to have a gain of 1.4 and by using equation (3.1). The resulting number of counts generated per photon is 0.655, which when multiplied by the number of photons gives us 16.61 counts due to noise. Taking our 3:1 signal to noise ratio results in pixels with a count lower than 49.8 containing only noise. The

readout noise can then be removed by disregarding any pixel that has a count lower than 49.8

The alignment program (*bulkfwrroughalignment2dXX*) is used to roughly align all the files recorded at a certain wavelength. The alignment has two stages to it, firstly the preparation of the first transmission image and secondly rastering of this image through all the other images in the list to be aligned and applying a correlation function to them. To aid in the visualisation of this method we will step a sample incoming and transmission array through the process. These two arrays can be seen in Figure 4-4

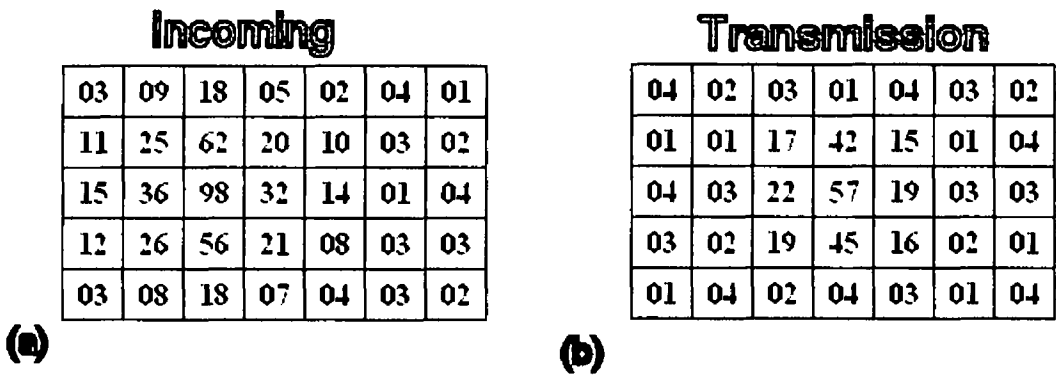


Figure 4-4 (a) shows the raw incoming image array (b) shows the raw transmission array

The first transmission image, which every other image in the set will be aligned with, is prepared by firstly creating a rough mask. This mask is created by setting each pixel in the mask to 0 if the corresponding value in the image is less than the three times noise. If however the signal is greater than three times the noise then the pixel in the mask is assigned the value of 1. In Figure 4-5 we shall assume the signal to noise ratio of 3:1 is achieved at a count of 4.5 so all pixels lower than this are set to 0 and all above are set to 1 in the mask.

Transmission to Mask

04	02	03	01	04	03	02
01	01	17	42	15	01	04
04	03	22	57	19	03	03
03	02	19	45	16	02	01
01	04	02	04	03	01	04

→

00	00	00	00	00	00	00
00	00	01	01	01	00	00
00	00	01	01	01	00	00
00	00	01	01	01	00	00
00	00	00	00	00	00	00

Figure 4-5 Creation of the mask from an array

The mask (M) and the transmission image (O) are then multiplied to gain the signal on top of a zero array (N) as shown in equation (4.1)

$$N(i, j) = O(i, j) * M(i, j) \quad (4.1)$$

where $N(i, j)$ is the value of the pixel in the cleaned image N , $O(i, j)$ is the value of the pixel in the image O and $M(i, j)$ is the value of the pixel in the mask (M). The new array generated from applying the masks can be seen in Figure 4-6

Incoming

00	09	18	05	00	00	00
11	25	62	20	10	00	00
15	36	98	32	14	00	00
12	26	56	21	08	00	00
00	08	18	07	00	00	00

(a)

Transmission

00	00	00	00	00	00	00
00	00	17	42	15	00	00
00	00	22	57	19	00	00
00	00	19	45	16	00	00
00	00	00	00	00	00	00

(b)

Figure 4-6 Result of applying equation (4.1) to (a) the incoming image and its mask and (b) the transmission image and its mask

The transmission image is now cropped and rastered through all the images to be aligned with it. In our example the cropped transmission image (Figure 4-7) is rastered through the incoming image

17	42	15
22	57	19
19	45	16

Figure 4-7 Cropped Transmission image

Rastering is the process where a smaller image I_1 of size (x_1, y_1) is moved through a larger image I_2 of size $(x_1+\Delta x, y_1+\Delta y)$ in steps of $\Delta x=1$ and $\Delta y=1$ until the end of the larger image is reached see Figure 4-8

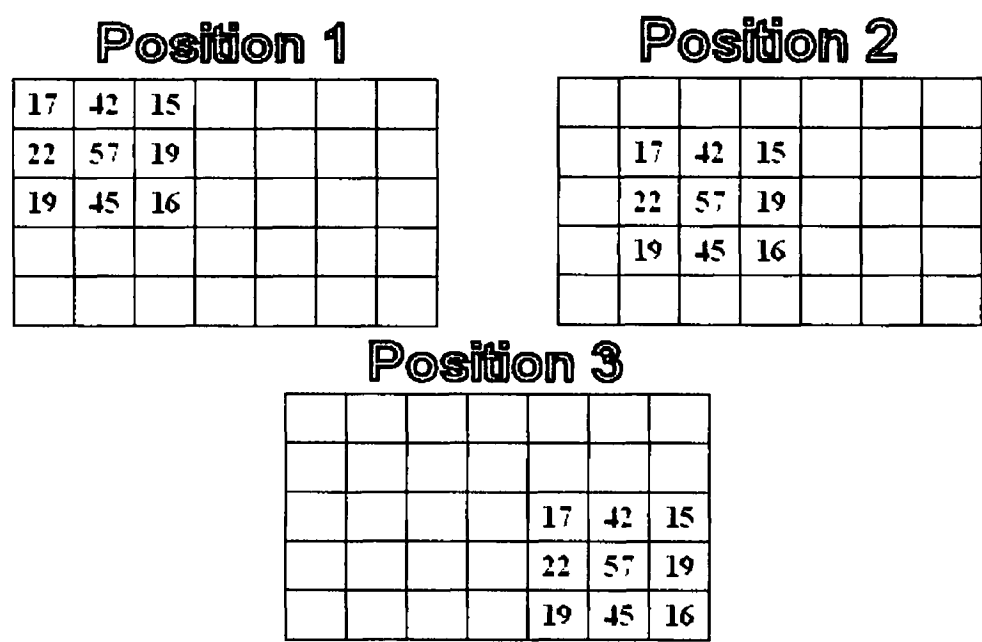


Figure 4-8 Example of rastering the small transmission image through a larger array with position 1($\Delta x=\Delta y=0$) being the starting position, position 3($\Delta x=4, \Delta y=2$) is the finishing position and Position 2($\Delta x=2, \Delta y=1$) is where the correlation function produces a maximum for the correlation function

During alignment, the correlation function (4 2)

$$f(I_1, I_2, \delta x, \delta y) = \sum_{x=1}^{x_1} \sum_{y=1}^{y_1} I_1(x, y) * I_2(x + \delta x, y + \delta y) \tag{4 2}$$

is calculated for each value of $\delta x = 0, 1, 2, \dots, \Delta x-2, \Delta x-1, \Delta x$ and $\delta y = 0, 1, 2, \dots, \Delta y-2, \Delta y-1, \Delta y$, where $I_1(x,y)$ is the number of counts of pixel (x,y) in image I_1 and $I_2(x+\Delta x,y+\Delta y)$ is the number of counts of pixel $(x+\Delta x,y+\Delta y)$ in image I_2 If we apply the correlation function to the transmission while being rastered though the incoming image we obtain a value of 2488 for Position 1, 13323 for Position 2 and 2183 for Position 3 Position 2 clearly has the greatest value When dealing with experimental

data, f would be calculated for all Δx , Δy until the position giving the maximum value for f is found

The pixels that correspond to the alignment image at the maximum value of the correlation function are extracted to a new smaller array that has the same size as the alignment array. The two aligned arrays can be seen in Figure 4-9, the top left value of Figure 4-9a is that of pixel $(\Delta x=2, \Delta y=1)$ of the original array Figure 4-4a

25	62	20
36	98	32
26	56	21

(a)

17	42	15
22	57	19
19	45	16

(b)

Figure 4-9 (a) is the aligned incoming array and (b) is the aligned transmission array

This process aligns the two images to ± 1 superpixel. The rough alignment applied to actual images from the CCD camera can be seen in Figure 4-10

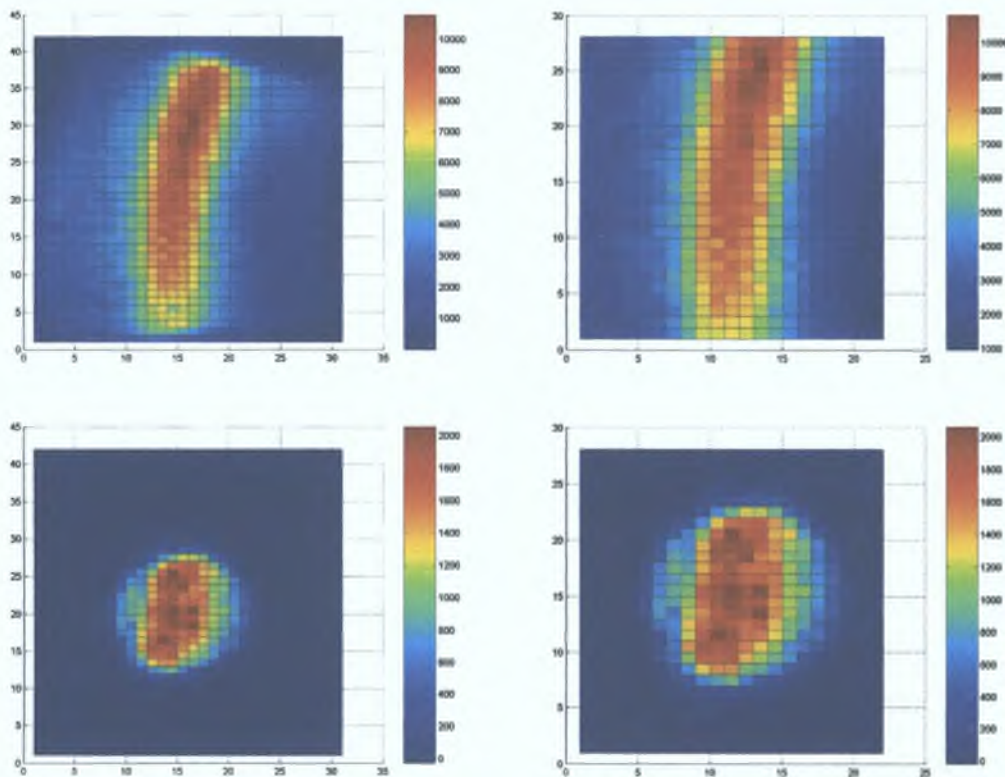


Figure 4-10 Alignment of images taken from the CCD camera. Pictures on the left are before aligning and pictures on the right is after aligning

With the images now within ± 1 superpixel of each other, the drift is not sufficiently compensated for yet as the majority of the images are binned and so further fine aligning must be done. This fine alignment (*bulkffinealign2dXX*) ensures that the images are aligned to within one tenth of a superpixel and relies upon interpolation of the pixels. This process is similar to the rough aligning as in it applies a correlation function to get the best alignment. The preparation of the files to be aligned however is very different. The same alignment image is used as previously while the incoming image is interpolated using a ‘spline’ interpolation algorithm. This style of interpolation was used as there was an inbuilt interpolation algorithm in Matlab that could handle 1-3 dimensional interpolation. The spline fit was chosen as the beam was set up to be gaussian like with the largest intensity at the centre. For the sake of clarity in the example, we only interpolate the incoming array to three times their size as shown in Figure 4-11.



Figure 4-11 Interpolation of the incoming array to 3 times its size. Each colour represents a different array

In the example the data that is originally in columns 1,2,3 is now resident in columns 2,5,8. The new larger array can then be split up into nine new arrays the same size as the original array. Each colour in the diagram represents one of the arrays. These nine arrays allow us to look at the image at ± 1 superpixel in the horizontal and vertical directions in steps of 0.33 of a superpixel (see Figure 4-12 the original incoming array can be seen in the centre).

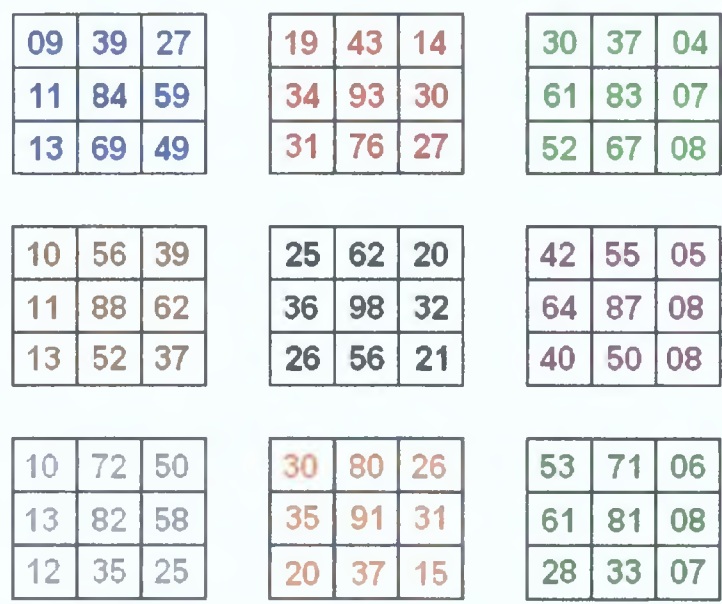


Figure 4-12 The interpolated incoming arrays where the original array is the one in the centre.

A correlation function using the alignment array is then applied to the nine incoming arrays. Like in the rough alignment the maximum value of the correlation function indicates the array that has the best alignment. For our sample incoming the aligned image happens to be the central array in Figure 4-12 the next is closely followed by the orange array below it whose value for the correlation function is a mere 7% lower than the one above it. The arrays are now aligned to within 0.33 of a superpixel. With the actual images the files are interpolated to 10 times their size, resulting in alignment of up to 0.1 of a superpixel. This alignment is more than adequate to correct for any drift of the beam.

This procedure was validated by applying it to a number of consecutive incident and transmitted images. These images were then aligned using both procedures. The rough alignment was then compared to the fine alignment. The mean value of the transmission did not change significantly, but the associated error was reduced by a factor of 2.

If we are working with samples that are smaller than the beam itself preparatory manipulation of the images is needed before any further analysis can be done. Usually such samples would be circular and held in place by a holder with a circular hole in it (see section 3.4). In such a case an elliptical (near circular) mask is generated from the alignment image and used on all the files, the results of which can be seen in Figure 4-13. In this particular measurement the film is only 2mm in diameter while the footprint of the beam is 4mm \times 4mm, so the incoming image must be cropped to compensate for the light that does not transmit through the sample holder. This is done after the background noise has been eliminated for both the incoming and transmission arrays and the images have been aligned. These automatically generated masks give a guide to removing the effects at the edge of the transmission image. This is carried out by simply reducing the size of the mask. Once this is done further analysis of the images may take place.

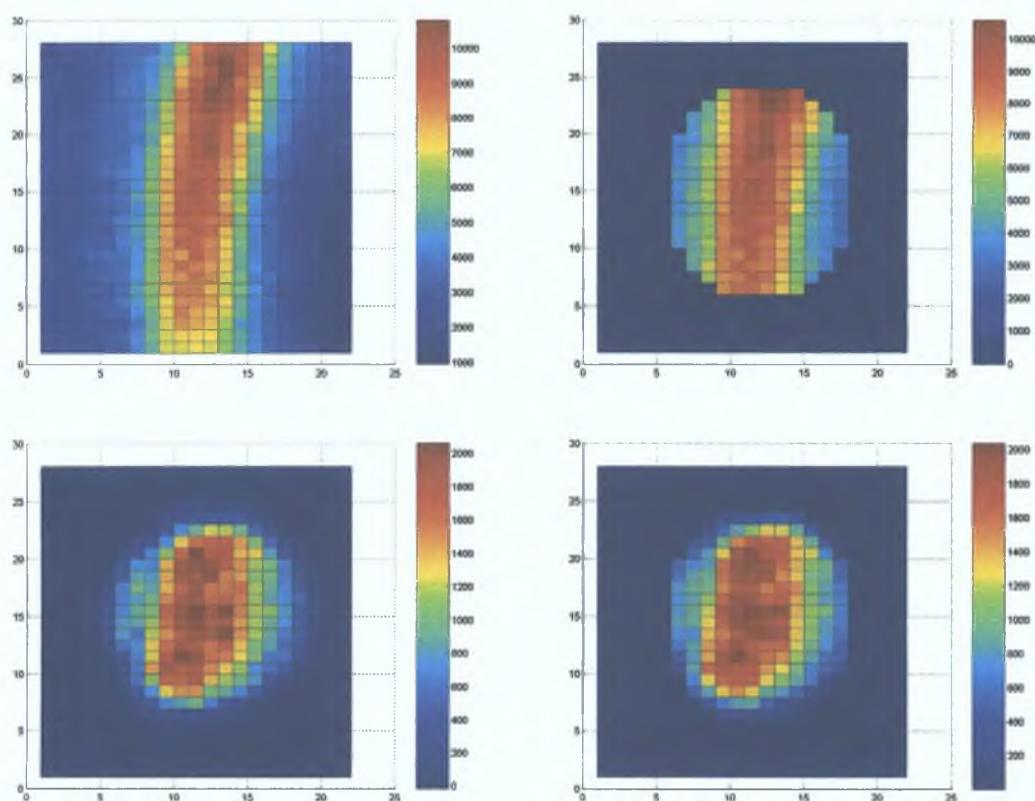


Figure 4-13 The top two pictures are incoming images and the bottom two are transmission images. The pictures on the left are before fine aligning the right is after fine aligning

In some cases the image must also be corrected due to the presence of holes in the film. These holes can often occur in very thin films. If any holes are identified while inspecting the images, another mask must be created that will remove the superpixels that correspond to the position of the hole as described in section 5.5.2. This has the result of eliminating the section from both the incoming and transmission images.

4.3 Extracting counts from the aligned images

Extracting counts from the images can begin when they are fully aligned according to the procedures stated at the start of section 4.2. How the counts are obtained depends on whether it is a one-dimensional file or a two-dimensional file

and if there were any filters used while the image was recorded. This process yields a value for the intensity of the incoming, transmitted, or reflected light at the wavelength in question.

4.3.1 *Example 1: One Dimensional Arrays*

When plotted out a one-dimensional file looks like that in Figure 4-14. These one dimensional arrays are referred to as plots.

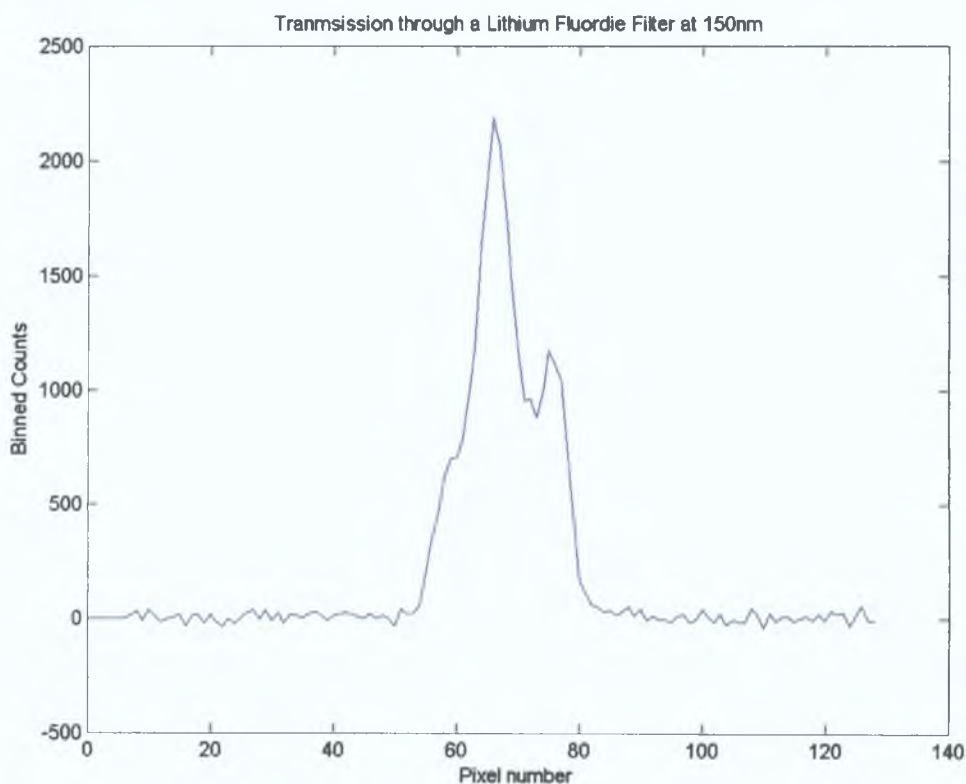


Figure 4-14 Raw Plot of binned data after a transmission through the Lithium Fluoride filter at 150nm

The standard experimental procedure stated at the start of chapter 4 should result in 6 incoming files and 5 transmission/reflection files in an incoming/ transmission (reflection)/ incoming configuration. Since all the shot numbers for each file were noted in the filename it is a simple task to extract this number and use it to interpolate the incoming file.

For example, assume that the incoming plot filenames were named <incoming>5, <incoming>15, <incoming>25, <incoming>39 and <incoming>49. The associated transmission plot filenames were named <transmission>10, <transmission>20, <transmission>34 and <transmission>44. This would correspond to a sequence where 5 shots were fired in recording each of the first three incoming, and first two transmitted plots. However, when the third transmission plot was recorded, 4 shots were fired. This plot was not saved, but another transmission plot was recorded having the required 5 shots. In order to carry out the interpolation of the incoming plots two sets of numbers need to be assembled: the shot numbers of each incoming plot and the shot number of all the plots. For the example above these sets of numbers would be (5,15,25,39,49) and (5,10,15,20,25,34,39,44,49). The first set tells the interpolation program how many shots were fired at the target when the incoming plot was recorded, while the second set of numbers tells the interpolation program at what stage an incoming and transmission measurement was recorded, so that we can evaluate the amount of light that was being produced when a transmission was being measured. At this point a decision needs to be made with regards to taking option 1 or option 2 shown in Figure 4-3. Option 1 should be taken if plot profile is needed for the analysis, while option 2 should be taken if only a simple average of the transmission is needed. This choice not only affects the rest of the analysis but also the complexity of any further calculations.

With option 1 all the incoming plots must be opened and stored in a stack like that in Figure 4-15. The shot numbers are then used to interpolate the stack of plots in order to generate the incoming plots that occurred during a transmission measurement. This results in a set of incoming and transmission/reflection plots that have the same shot number. We can then divide the transmission plot by the

interpolated incoming plot to obtain a plot of the transmission. Further analysis of the profile may then be done. For our needs these plots may simply be averaged to gain a value for the percentage transmission of the sample. This method requires a lot of computation time due to interpolating stacks of plots.

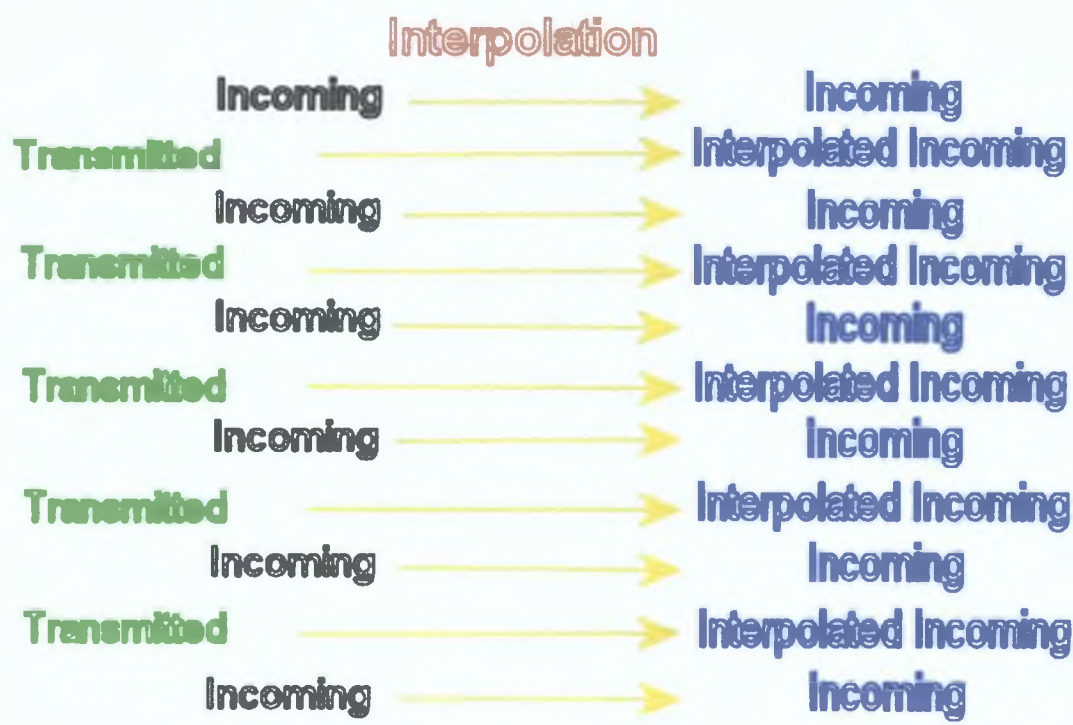


Figure 4-15 Diagram of how the Incoming images are stacked and then interpolated

In option 2 the plots are averaged prior to interpolating the incoming. This means that instead of interpolating a stack of plots we are simply interpolating a set of numbers. This reduces calculation time to a large degree and it is this method that is favoured for transmission measurements. If a gas filter is used the method of calculation is stated in section 4.3.3. Otherwise the five values for the percentage transmission/reflection can then be averaged to obtain a value with an associated standard deviation. It is this value that is used in the calculations detailed in sections 4.4 and 4.5.

4.3.2 *Example 2: Two Dimensional Arrays*

The two dimensional arrays are images as opposed to plots like the one dimensional arrays, they can be up to a size of 2048×512 pixels (the maximum resolution of the CCD). The incoming images need to be interpolated in a similar way to the one-dimensional arrays in section 4.3.1. The same choice for averaging the images prior to interpolation must be made; selecting option 2, the averaged counts of the image is used for the interpolation. The major difference with dealing with two-dimensional arrays would be with interpolating the images. As a stacked array of images would be huge and the resulting interpolated stack would be almost twice the size. The time taken to interpolate these would not be short and so taking the average would be recommended unless the shape of the image is required. The amount of transmission/reflection is calculated in the same way as the one-dimensional technique.

4.3.3 *Filters*

The use of gas filters complicates the analysis, as there is another absorbing medium in addition to the thin film. Measurements taken under vacuum with a solid filter such as a lithium fluoride window or a neutral density filter would not affect the analysis procedure, because the window would absorb a constant fraction of the beam. However, when using gas filters such as helium or argon, an exact pressure would have to be maintained to ensure a relatively constant absorption. In order to find what pressure we required to remove all the second order light we ran an experiment in which we incrementally increased the gas pressure. Unfortunately at the higher pressure the gas was able to get into the target chamber, which affected the plasma expansion and thus the positioning of the plasma on the optical axis of the beamline.

Such a situation was not acceptable. It was decided that in order to use gas filters reliably it was necessary to take several measurements at lower pressures. At each pressure a value for the average incoming and average transmission/reflection was measured. When each of these values was plotted as a function of pressure, two exponentially decreasing graphs result with similar decay rates. The asymptote of each graph gives the first order contribution of the incoming and the reflected or transmitted images, from which the amount of reflection or transmission can be calculated (see Figure 4-16)

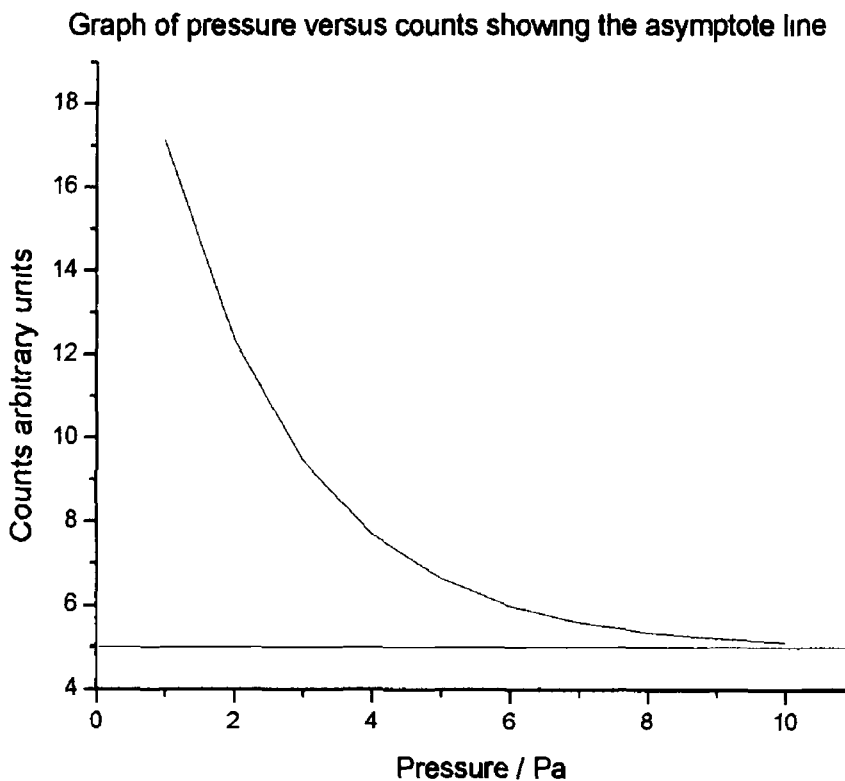


Figure 4-16 Sample plot showing the decay of counts with increasing pressure. The red line shows the asymptote line, which the value of the graph is tending to

4.4

Calculating Absorption Data

With the transmitted values calculated for a few thicknesses at a single wavelength a graph can be put together showing how the transmission varies with thickness. A graph such as this should be an exponentially decaying graph whose decay constant contains the absorption coefficient. In order to do this the thickness of the samples need to be measured. Once this thickness is known an absorption spectrum may be created.

4.4.1 *Thickness Measurements*

Measuring the thickness of the sample is extremely important as according to theory the transmission through a material is given by equation (4.3)

$$T = T_0 \exp(-\alpha d) \quad (4.3)$$

where T is transmitted intensity, T_0 is the light intensity after the effects of the interface, α is the linear absorption coefficient through the sample and d is the thickness. Unfortunately a value for T_0 cannot be directly measured. However, T_0 can be obtained by normalising the transmission with the incident light. We may then plot the natural log of the normalised transmission against the thickness of the film, and T_0 can be obtained from the vertical intercept.

Equation (4.3) shows that a slight change in the thickness of the sample can significantly affect the resulting calculation of the absorption coefficient, especially when the material strongly absorbs at the wavelength of interest. It is therefore a necessity to accurately measure the thickness of all samples that we intend to measure the absorption coefficient of. To this end three independent measuring systems were

used. The first was the thickness monitor inside the deposition chamber, the second was a Profilometer and the third was an Atomic Force Microscope.

4.4.1.1 Thickness Monitor

The thickness monitor is simply a crystal that is suspended in the deposition chamber of the evaporator at a position that the evaporated material may be deposited onto it. The crystal is driven at a frequency of 6MHz. The frequency of oscillation of the crystal is monitored and is dependent upon the mass of the crystal. When deposition of material occurs the oscillations slow down. The thickness of the material may be determined by measuring this change in frequency. The thickness is then calculated using equation (4.4) [48]

$$T_f = \left(\frac{D_q}{D_f} \right) \left(\frac{N_q T Z_f}{\pi Z_q} \right) \tan^{-1} \left(\frac{Z_q}{Z_f} \tan \left(\pi \left(1 - \frac{T_q}{T} \right) \right) \right) \quad (4.4)$$

where T_f is the film thickness, D_q is the density of quartz, D_f is the density of the film, N_q is the frequency constant of the quartz crystal, T is the period of the loaded crystal, Z_f is the acoustic impedance of the film material, Z_q is the acoustic impedance of the quartz and T_q is the period of the unloaded crystal. Once all the required constants are known it is a simple task to work out the film thickness for each film that is grown.

4.4.1.2 Profilometry

A profilometer is a measurement device that probes the surface topology of a sample material by sweeping a stylus across the surface. It is an inherently destructive technique as the stylus is kept in contact with the surface at all times with a constant force, this means that it can scrape the top layer off a sample as it is swept over it. It is therefore not an ideal measurement technique for soft samples or very thin samples. Upon sweeping the stylus over the surface the vertical movement is

recorded. This gives a height map of the surface as a function of distance from the starting point; an example of such a height map may be seen in section 5.4.3.2. The profilometer used is a surface profiler Dektak V200 Si made by Veeco. It can handle substrates up to the size of 200mm^2 and has a range of stylus sizes to choose from depending on the accuracy that is required (the stylus used in this work has a radius of 1.25mm). The force applied to the stylus may be varied from $4 \times 10^{-3}\text{N}$ to $2.9 \times 10^{-1}\text{N}$. It has a maximum resolution of 0.1nm when measuring surfaces with a maximum height of 6500nm . The resolution of the device varies depending on the height range that is selected up to a maximum height of $800\mu\text{m}$.

The analysis of the data from the measurements made with the profilometer was quite simple. The reason for the simplicity is that the profilometer produces plots of the topography at each place that was measured. In our samples they resulted in a step profile see Figure 4-17.

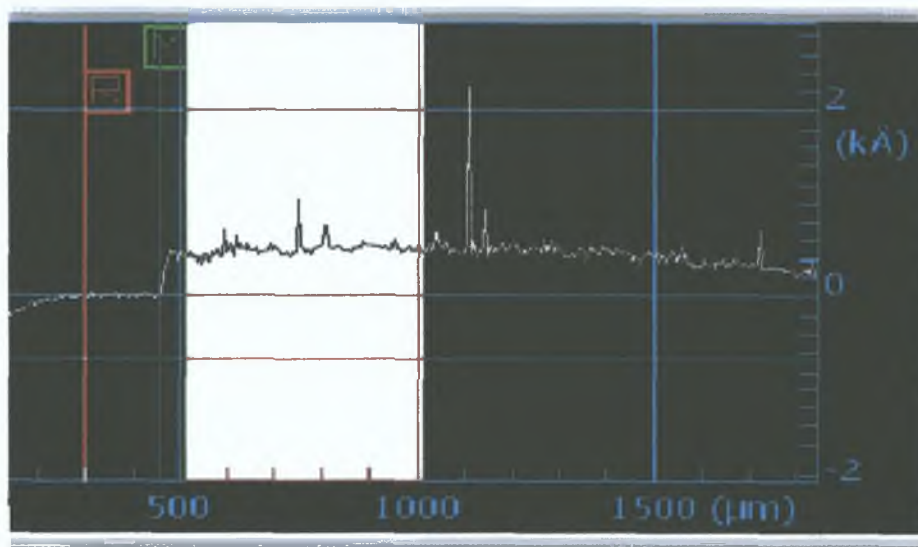


Figure 4-17 Thickness of an aluminium film on a glass side measured across its surface using the profilometer

The height of the step was measured using the profilometer control software. The heights of several measurements were then averaged to gain the average height of the

step, which is effectively the thickness of our sample. The results of the measurements may be found in section 5.5.3.2.

4.4.1.3 *Atomic Force Microscopy*

An Atomic Force Microscope (AFM) is a device similar in nature to a profilometer, but the implementation of the idea is quite different. The AFM uses a microscopic tip whose height is controlled by piezoelectric arms. This results in a non-destructive scan of a surface when in tapping mode that is accurate to the atomic level. The movement of the piezoelectric arms then determines the topography of the surface. The instrument used was a Dimension 3100 Scanning Probe Microscope (SPM) from Veeco Ltd. It utilizes automated atomic force microscopy (AFM) and scanning tunnelling microscopy (STM) techniques to measure surface characteristics of various types of samples up to 150mm in diameter. The scanner head includes a piezoelectric tube scanner, a laser, and a quadrature optical detector, which ensures a constant low tip-sample force over the entire scan area. The optical detector can monitor the tip and the surface, while the laser determines the height of the tip from the surface. When the tip is being brought close to the surface the laser guides the head to a safe distance above it and then it is brought down slowly until it makes contact. Once the tip is in contact with the surface the piezoelectric tube scanner takes over to scan the surface. There are different types of scans that can be done with this AFM. The tip can be simply moved across the surface to get topography in this way however there are drawbacks. These are mainly due to the frictional forces between the tip and the surface while dragging it across the surface, which could damage both the tip and the surface. To get around this the tip can be placed in tapping mode where the piezoelectric arm is set to oscillate at a set frequency. The

frequency change is then monitored and the height of the arm is adjusted to maintain this frequency as the tip comes in contact with features on the surface. The height adjustment of the piezoelectric arm is then monitored, as the tip is rastered across the surface of the sample until it scans the entire area selected with the control software. Images taken by the AFM can be seen in section 5.4.3.3.

For our needs we only needed to identify the height of the step between the glass substrate and the aluminium film deposited onto it. However, when using an AFM you tend to get a bend in the image due to the nature of the piezoelectric arms and the large scan size used. This bend can be corrected for quite easily for data in the same plane. Unfortunately the images obtained using the AFM shown in section 5.5.3.3 have a step in them. Therefore more complex processes had to be carried out on the images in order to flatten them and then extract the proper height information. Using a flatten command in a program called WsXm [49] reduced the bend in the image Figure 4-18.

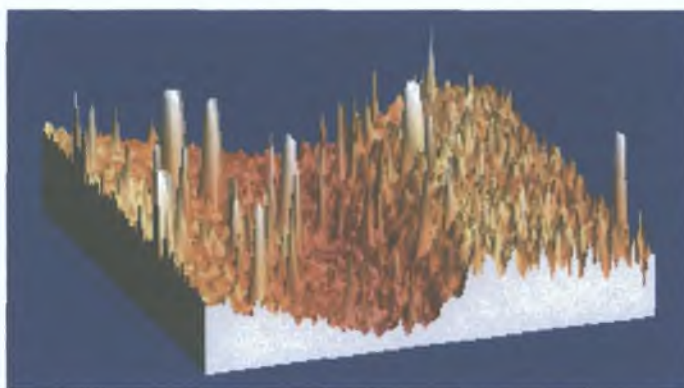


Figure 4-18 WsXm flatten command applied to the entire raw image from the AFM. Notice the four corners at the same height

This did not fully flatten out the image but instead set all four corners to the one height giving a tilted image. This was improved by setting the location of the area to be flattened to that corresponding to the substrate (in our case it was the glass slide) to one plane and then carrying out a flatten command on this section Figure 4-19. Doing

this almost corrected the tilt and eliminated the bend in the image. The only option left to get the height information was to take height plots across the sample.

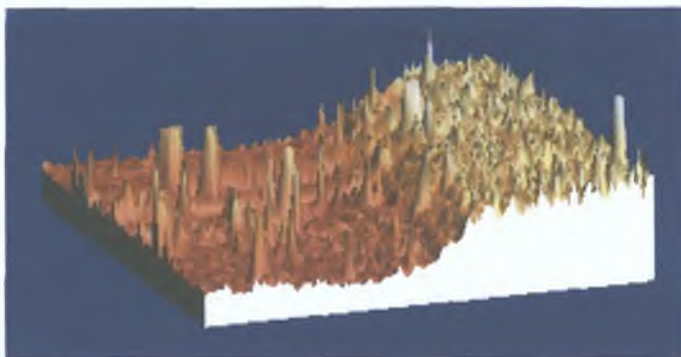


Figure 4-19 The left hand side of the image was the substrate this was picked out and flattened. This resulted in the step being quite obvious.

These plots were then curve fitted so that the height of the glass and then the film could be calculated. It was then a simple matter of subtracting the height of the glass from that of the film to determine the thickness of the sample. Such plots were taken across the film and the heights averaged.

4.4.2 *Absorption Spectra*

When all the thicknesses are calculated they can be plotted against the natural log of the transmitted values. A straight line can be fitted to this data. The slope of the fitted line corresponds to the absorption coefficient. This procedure needs to be carried out for all wavelengths that the films were examined at. This results in absorption spectra, which can be compared with other spectra obtained from the literature. When the absorption spectra are created we can utilise a Kramers Kronig analysis on the imaginary refractive index (see equation (2.37)) to obtain values for the real refractive index at the wavelengths of interest. This is best done by using the data along with those from the literature to increase the range of the data prior to applying a Kramers Kronig analysis.

4.5 *Reflection Analysis*

The analysis of the reflection data is quite similar to that of the transmission data. The procedures only deviate when the ratio of the reflected to incoming is taken. At this point a Kramers Kronig Analysis is carried out on the data.

4.5.1 *Kramers Kronig Analysis*

The theoretical explanation of a Kramers Kronig analysis can be found in section 2.3. In this case the data that is being analysed is reflection data. Adding data from the literature onto the higher and lower wavelength regions can expand the range of the data, thus improving the accuracy of the calculation. Care must be taken with this as it is necessary that the function be smooth, continuous and have the same step size through the entire data set. Theoretical wings may also be applied to the high and low wavelength regions. At the high wavelength region the reflectance tends towards that reflectance taken in the visible. While at lower wavelengths the reflectance tends to drop off as ω^{-4} . More details about these wings may be found in [6]. With the extended wings it is now possible to run the Kramers Kronig Program (RefKKDennXX see appendix A) with the data. This will produce the phase change upon reflection at each point. With the reflection and the phase it is possible to calculate the optical constants using equation (2.39) and equation (2.40).

4.5.2 *Sum Rules*

There are several sum rules that have been calculated over the last century and are stated in section 2.4. These rules can be applied to increase the accuracy of any analysis of the optical constants. The most applicable of all are the Partial f sum

rules, which relate the effective number of electrons that take part in an excitation to the various optical and dielectric constants equation (2.46)-(2.48). The application of this sum rule was used in [8] to show that there was an error in the measurement of the absorption coefficient below the L edge. These sum rules are fairly easy to apply, as it only requires a file containing the energy and the appropriate absorption or dielectric constant. Once such a file is available it is simple to numerically integrate the data. A program was written in Matlab to calculate the partial f sum rule using the imaginary refractive index (*Partial_sum_absorption.m*). This program was used to calculate the effective number of electrons contributing to the absorption of light in gold (see section 5.1.2).

The inertial sum rule equation (2.41) can be used as a verification of a Kramers Kronig analysis, specifically for the real refractive index. This verification of the analysis requires the normalisation of the sum rule, this results in a verification factor (ξ) which can be used to judge the accuracy of the real refractive index. It shows the error in the real part of the refractive index and is shown in equation (4.5) [8], the ideal value of ξ is 0 showing no error.

$$\xi = \frac{\int_0^{\infty} [n(\omega) - 1] d\omega}{\int_0^{\infty} |n(\omega) - 1| d\omega} \quad (4.5)$$

This verification factor can be easily calculated using matlab with the appropriate file similar to the one mentioned previously. Such a file was generated for those real refractive indices in section 5.1.1 and 5.1.2, the verification factor of these files were calculated by using a program called *Inertial.m* in Matlab.

5 System Testing and Experimental Results

Chapter 4 detailed the analysis system which is put to the test using the experiments discussed in this chapter. The experimental set-ups described in chapter 3 gave us a viable way of obtaining reflection and transmission data for the two different styles of experiments. We will discuss the experimental measurements that were taken and present the decisions that had to be made to improve the reliability of the experiments with regards to the use of filtering and the changing of test material.

We will first discuss the testing of the Kramers Kronig analysis program. It was tested using a method shown in [6], which used Lorentzian oscillators to computationally generate optical constants and reflection data for a hypothetical material. The KK program is then used to recalculate the optical constants from just the reflection data. The original optical constants may then be compared with the constants calculated using the KK program. We were able to extend the method used in [6] by showing how the wings affect the end result, which we show by including the inertial sum rule test. The program was then used on experimental gold data over a wide energy range obtained from the literature.

Time permitted only a full range of experimental tests to be carried with the transmission set-up. The initial testing of the analysis system was carried out with a number of calcium fluoride windows. During the investigation of the windows it became evident that spectral filters would be a necessity for measurements using the VUV beam. Regrettably after the introduction of suitable filtering to characterise the windows it was shown that the windows were not in fact made out of a single crystal.

This showed that the analysis system could identify problems with contaminants yet these insights hindered us from verifying or even improving on existing data [50]

This opened the way to the next step in our research, the creation of our own thin films of aluminium, which were supported by TEM grids. The grids were analysed prior to depositing the aluminium thin films onto them so that their transmission was known and could be used later in the analysis if necessary. The transmission data of aluminium was then fully analysed to obtain the transmission of each film at a number of chosen wavelengths. This allowed for the comparison of our data with data found in the literature. In order to make this comparison the thickness of the films needed to be measured, which allowed us to calculate the mass absorption coefficient of aluminium at each wavelength. The thickness was measured by using three independent techniques, a thickness monitor in the deposition chamber, and step measurements using a profilometer and an AFM. With this thickness data available, mass absorption coefficients could be calculated and plotted showing the difference between our data and that found in the literature.

The chapter will conclude with a discussion of all the results and the kind of future work that can be carried out in this area.

5.1 *Testing of the Kramers Kronig analysis program*

The Kramers Kronig analysis system was primarily programmed to work with the reflection data taken from the reflection set-up described in section 3.2.4 however it is easily modified to work with the other forms stated in section 2.3. The analysis system described in section 4.5 was extensively tested using artificially generated

reflection data and also with reflection data calculated from experimental data of optical constants for gold [50]

5.1.1 *Generated Data*

In order to test the Kramers Kronig analysis system, data had to be generated in the form of a file containing energy data and reflection data, which would correspond to the data that we could measure. The dielectric constants and/or the optical constants corresponding to this data can also be calculated, and allow us to assess the effectiveness of the analysis. The dielectric constants can then be determined using equations (5.1) and (5.2), which stem from equations (2.22) and (2.23)

$$n^2 - k^2 = \epsilon_1 \quad (5.1)$$

$$2nk = \epsilon_2 \quad (5.2)$$

It was decided to simulate a triple resonance system using Lorentzian oscillators (see section 2.2.4) separated by certain energy similar to that used in [6]. This was done by using equation (5.3) (in CGS units), which follows from equation (2.35), and is implemented using the procedures stated in section 4.5.1

$$\epsilon_1 + i\epsilon_2 = 1 + \frac{4\pi e^2}{m} \sum_{j=1}^3 \frac{f_j}{(\omega_j^2 - \omega^2) - i\Gamma_j \omega} \quad (5.3)$$

The three oscillators were selected to reside at 10, 15 and 20 eV. Each oscillator had strength of 5.8×10^7 to correspond with those used by Bortz *et al* [6]. The resulting dielectric constants and the optical constants were calculated between 0 and 30 eV in steps of 0.5 eV using equations (5.4)-(5.7), the resulting graphs can be seen in Figure 5-1. Equations (5.4) & (5.5) come about as a direct result of equation (5.3) while

equations (5 6) & (5 7) come about due to the relations given by equations (5 1) & (5 2)

$$\varepsilon_1 = 1 + \frac{4\pi e^2}{m} \sum_{j=1}^3 \frac{f_j (\omega_j^2 - \omega^2)}{(\omega_j^2 - \omega^2)^2 + \Gamma_j^2 \omega^2} \quad (5 4)$$

$$\varepsilon_2 = \frac{4\pi e^2}{m} \sum_{j=1}^3 \frac{f_j \Gamma_j^2 \omega}{(\omega_j^2 - \omega^2)^2 + \Gamma_j^2 \omega^2} \quad (5 5)$$

$$n = \left\{ \frac{1}{2} \left[\sqrt{\varepsilon_1^2 + \varepsilon_2^2} + \varepsilon_1 \right] \right\}^{1/2} \quad (5 6)$$

$$k = \left\{ \frac{1}{2} \left[\sqrt{\varepsilon_1^2 + \varepsilon_2^2} - \varepsilon_1 \right] \right\}^{1/2} \quad (5 7)$$

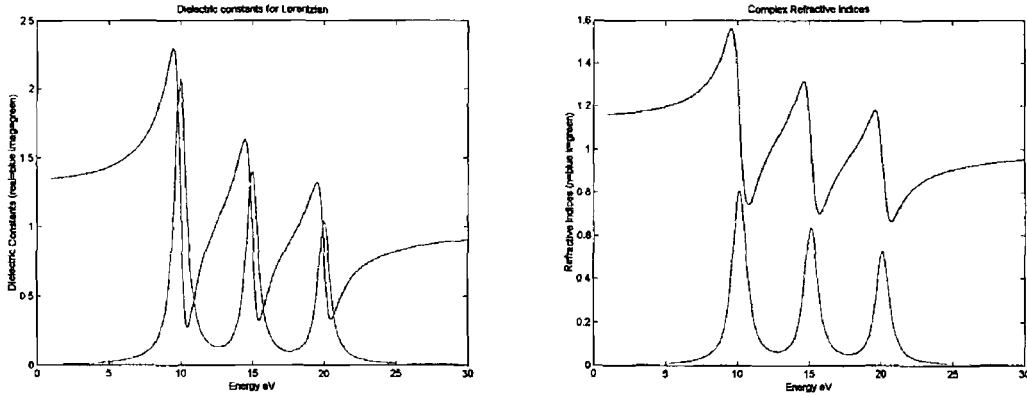


Figure 5-1 Shown on the left are the dielectric constants generated from three Lorentzian oscillators Shown on the right are the optical constants calculated from the dielectric constants

The reflectivity can then be calculated from the optical constants using equation (5 8) it is plotted in Figure 5-2

$$R = \rho^2 = \frac{(n-1)^2 + k^2}{(n+1)^2 + k^2} \quad (5 8)$$

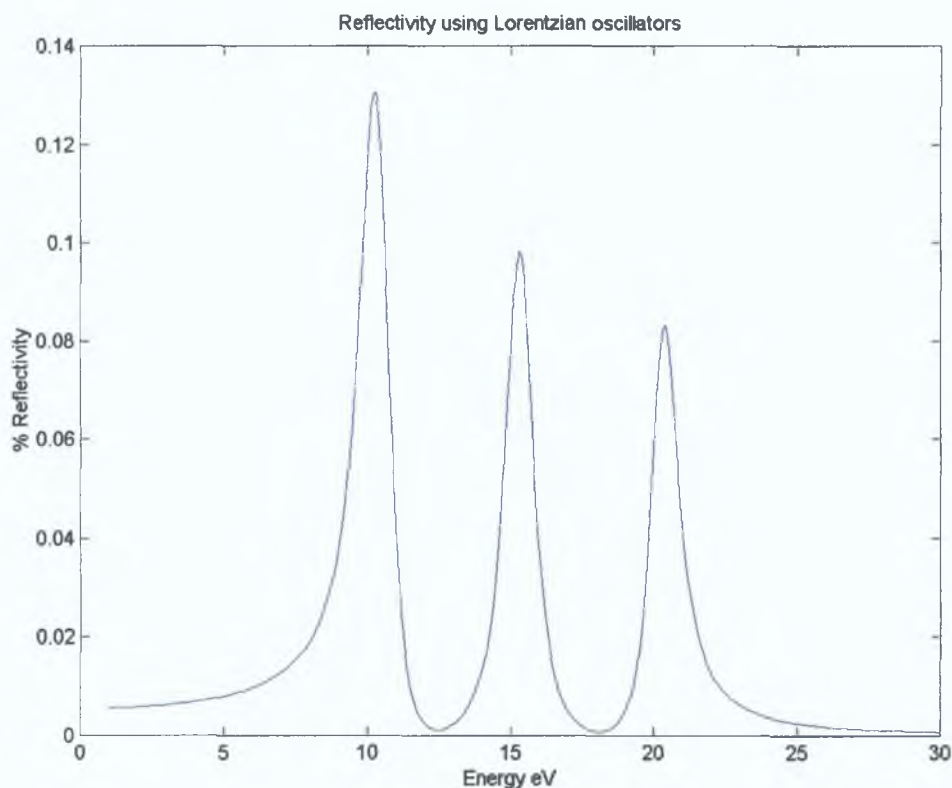


Figure 5-2 Reflectivity calculated from the optical constants in Figure 5-1.

These reflectivity data are then sent through the Kramers Kronig routine, which will calculate the phase change upon reflection according to equation (2.38). This phase can be used in conjunction with the reflectivity in equations (2.39) and (2.40) to calculate the optical constants. The accuracy of the Kramers Kronig calculation can then be evaluated by comparing the original dielectric and optical constants with the new calculated ones.

Numerous papers in the literature (see for example [6]) state how the size of the energy range affects the accuracy of the result, yet the effect of either wing on the result was not examined in any great detail. We shall endeavour to examine such a relationship between the sizes of the data sets to the end result after a Kramers Kronig analysis. To see how the use of a small energy range affects the result, the reflection data set mentioned above was first simply sent through the Kramers Kronig analysis.

The results of this can be seen in Figure 5-3. It is clear that the constants obtained from a Kramers Kronig analysis are a lot different from the original constants calculated from (5.6) and (5.7) in Figure 5-1.

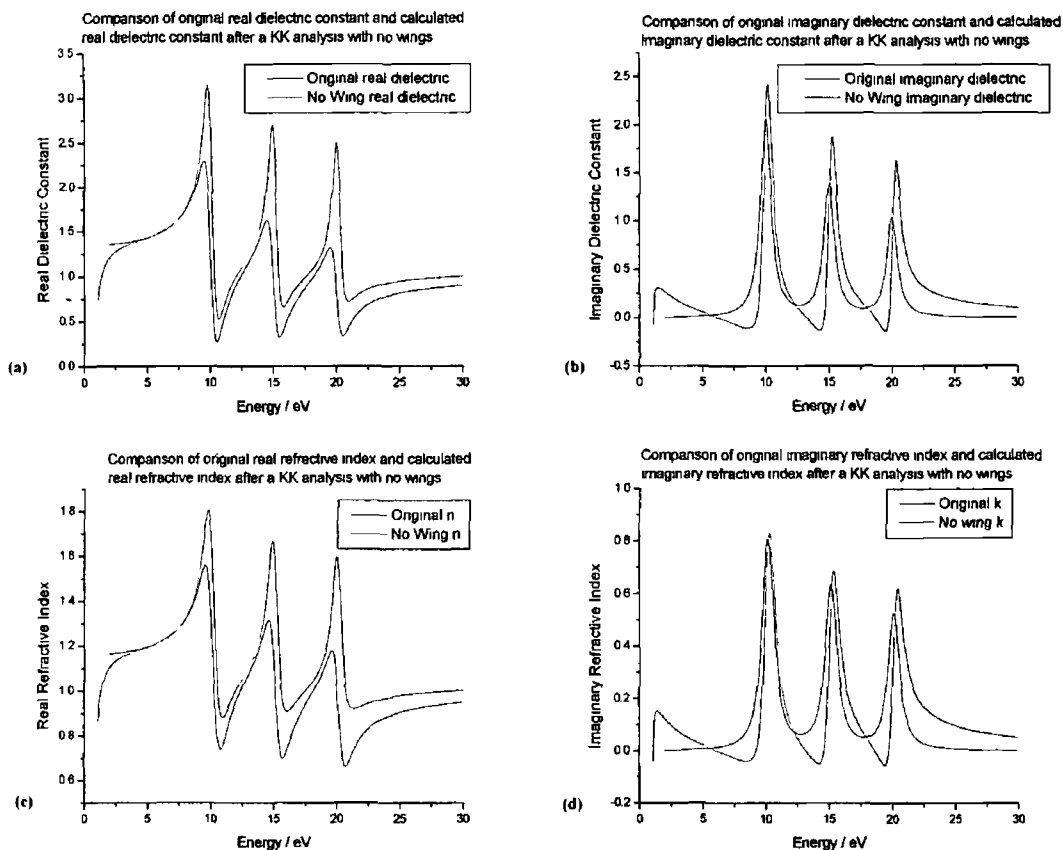


Figure 5-3 These are the calculated dielectric and refractive indices compared with the original values (a) is the real dielectric constant, (b) is the imaginary dielectric constant, (c) is the real refractive index and (d) is the imaginary refractive index.

The difference in values for a theoretically perfect data set is unsatisfactory. If the procedure followed here were applied to actual data, it would result in erroneous results for the optical constants. When the real refractive index was tested using the inertial sum rule it resulted in a verification factor (see sections 2.4 and 4.5.2) of 0.8692, this value is unacceptably large. The best verification factor should be 0.

In [6] the theoretical wings extending the data to 0 and to higher energies were added to increase the effectiveness of the Kramers Kronig analysis. To see how this would improve the data, we added wings to the Lorentzian reflectivity data

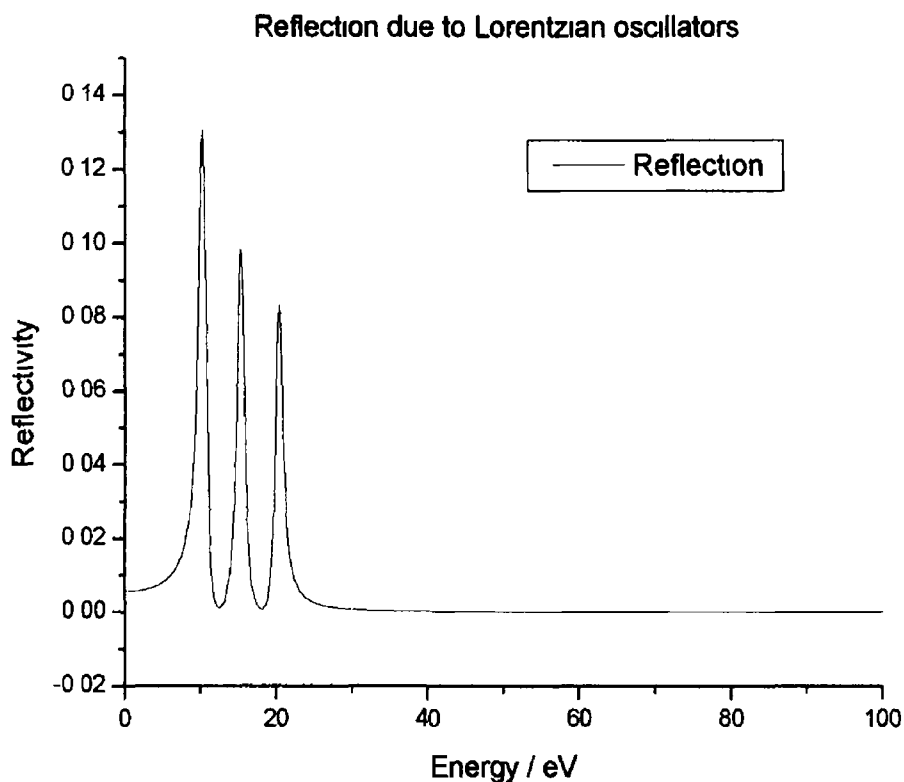


Figure 5-4 Graph of the reflection of the triple Lorentzian function from Figure 5-2 with wings It shows the addition of the theoretical wings the higher wing extends up to 1000eV The green section on the left represents the lower wing and the red section on the right represents the upper wing

First, a lower energy wing was added (the green and black portions in Figure 5-4) which tended towards the experimentally determined reflectivity at the lowest energy (in the visible)[6] The resulting dielectric and optical constants can be seen in Figure 5-5

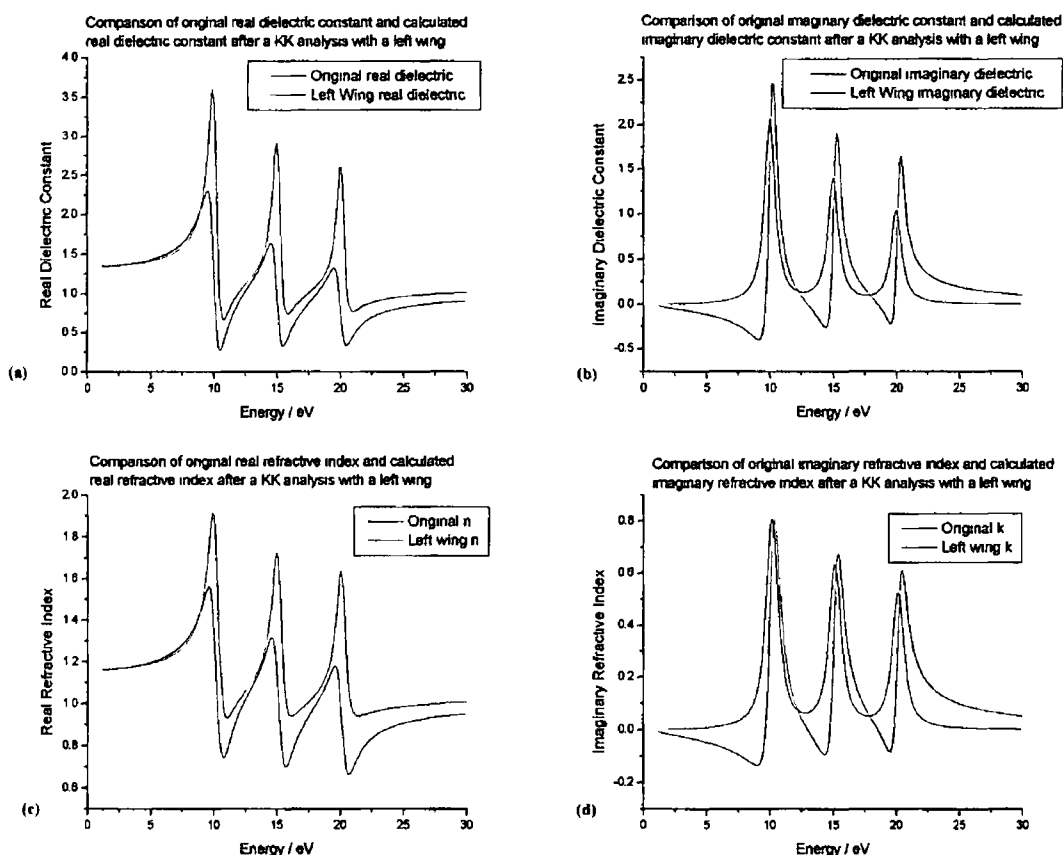


Figure 5-5 Placing a wing on the low energy region allowed a better determination of the dielectric and optical constants (a) is the real dielectric constant, (b) is the imaginary dielectric constant, (c) the real refractive index and (d) the imaginary refractive index.

On examining the graph it is obvious that the addition of the lower wing has drastically improved the shape of the low energy values. It ensured that the imaginary refractive index (k) tends towards 0 and real refractive index (n) is tending closer to 1. However the values of the constants elsewhere are still not equal to the expected values. When the real refractive index was tested using the inertial sum rule it resulted in a verification factor of 0.7866, this value is still very large.

To improve this, a high energy wing was applied to the reflectivity, which made the reflectivity drop off as ω^{-4} . This high energy behaviour is consistent with equations (5.3) and (5.8). This new set was extended to 1000eV (all the graph in Figure 5-4) and then analysed again to see what improvements this new high wing would effect. This can be seen in Figure 5-6.

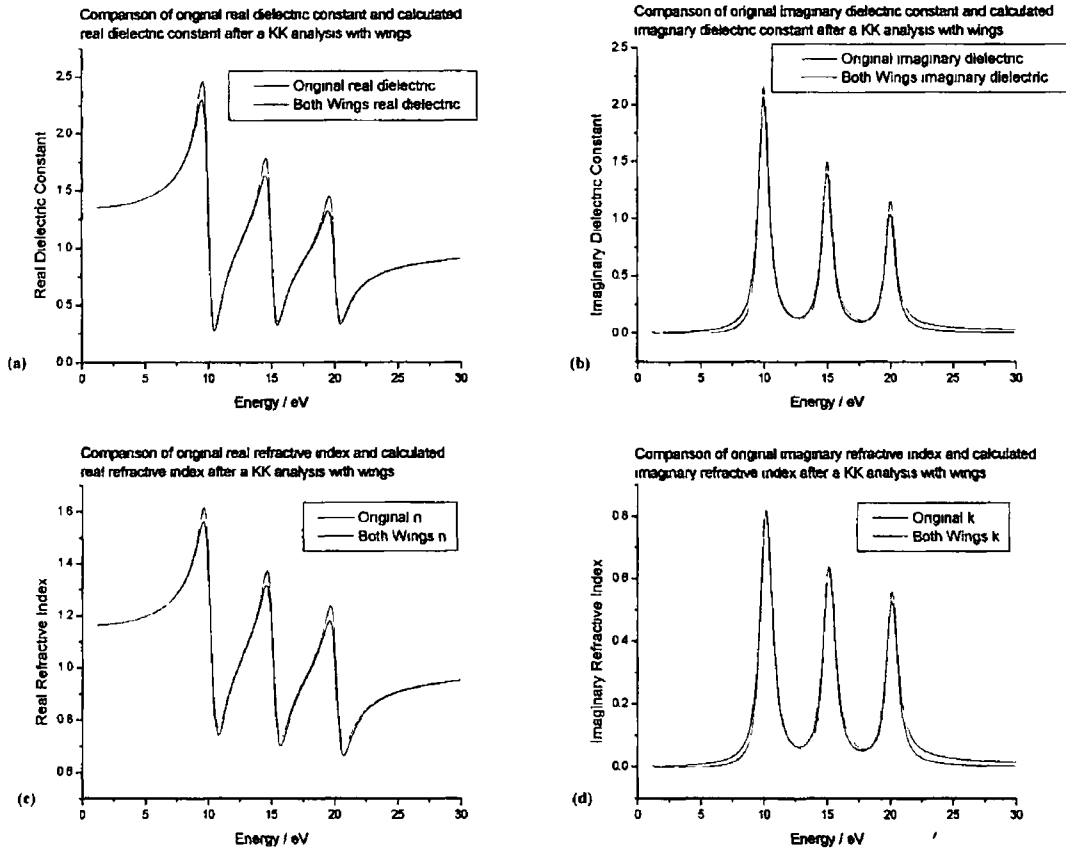


Figure 5-6 With wings on both the upper and lower energy the dielectric and optical constants have a better agreement with the actual constants (a) is the real dielectric constant, (b) is the imaginary dielectric constant, (c) is the real refractive index and (d) is the imaginary refractive index.

The addition of the upper wing to the data set containing the lower wing has drastically improved the data to such an extent that it is nearly unrecognisable from the original dielectric and optical constant plots. The calculated error on the new constants is around 0.05%. When the real refractive index was tested using the inertial sum rule it resulted in a verification factor of 0.1078, this value is much smaller than the last two results and shows how increasing the data set improves the calculation of the refractive index. It also shows how useful the sum rule is for identifying errors when we compare the value obtained when comparing the original to the calculated refractive index.

Utilising the test function above we witnessed how the upper and lower wings affect the end result and hence prove the effectiveness of our Kramers Kronig analysis.

program We can therefore apply the program to analyse actual reflection data obtained from the literature [50]

5.1.2 *KK analysis of Experimental Data*

The Kramers Kronig analysis program was used on reflection data calculated from the optical constants of gold from [50] This data was tabulated in Paliks book [50] and covered an energy range of 0.125-9919 eV from five different authors (Dold, Theye, Canfield, Hagemann and Zombeck, for references see [50]) With such a large energy region there was no need to add any theoretical wings, but some interpolation was carried out on the data to ensure a constant step size throughout the range As these are published data containing values for both the real and imaginary refractive indices we can therefore use the results as an applicable test to further check our programs accuracy

The results of the analysis can be seen in Figure 5-7 to Figure 5-10 The graphs show the original real and imaginary refractive index from Palik [50] plotted next to the real and imaginary refractive indices calculated from a Kramers Kronig analysis of the total set The entire experimental data set ran from 0.125-9919eV utilising a step size similar to that used in section 5.1.1 (0.5eV)

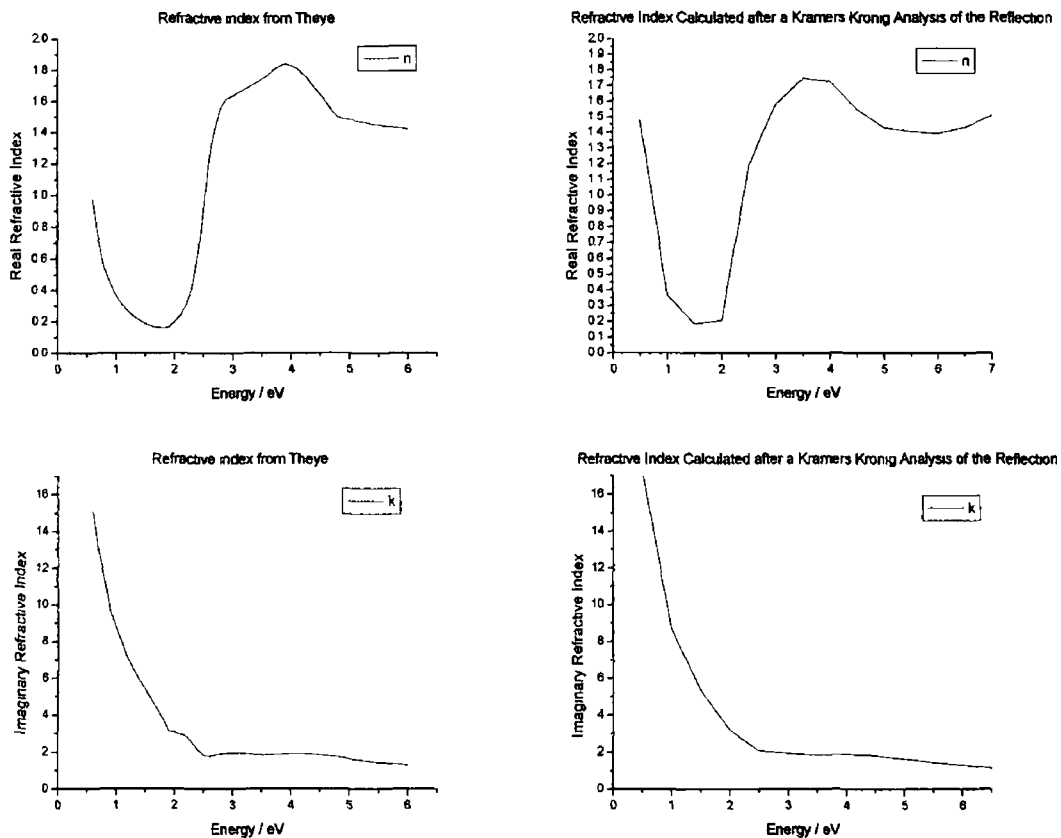


Figure 5-7 Results from data in the region that Theye measured in The left is Theye' data and the right is the data calculated using our Kramers Kronig analysis program on the reflection data.

Figure 5-7 shows the results from the 1-6eV region The step size is much larger than that of the original experimental data, but the similarity of the shapes and values of the calculated data are encouraging

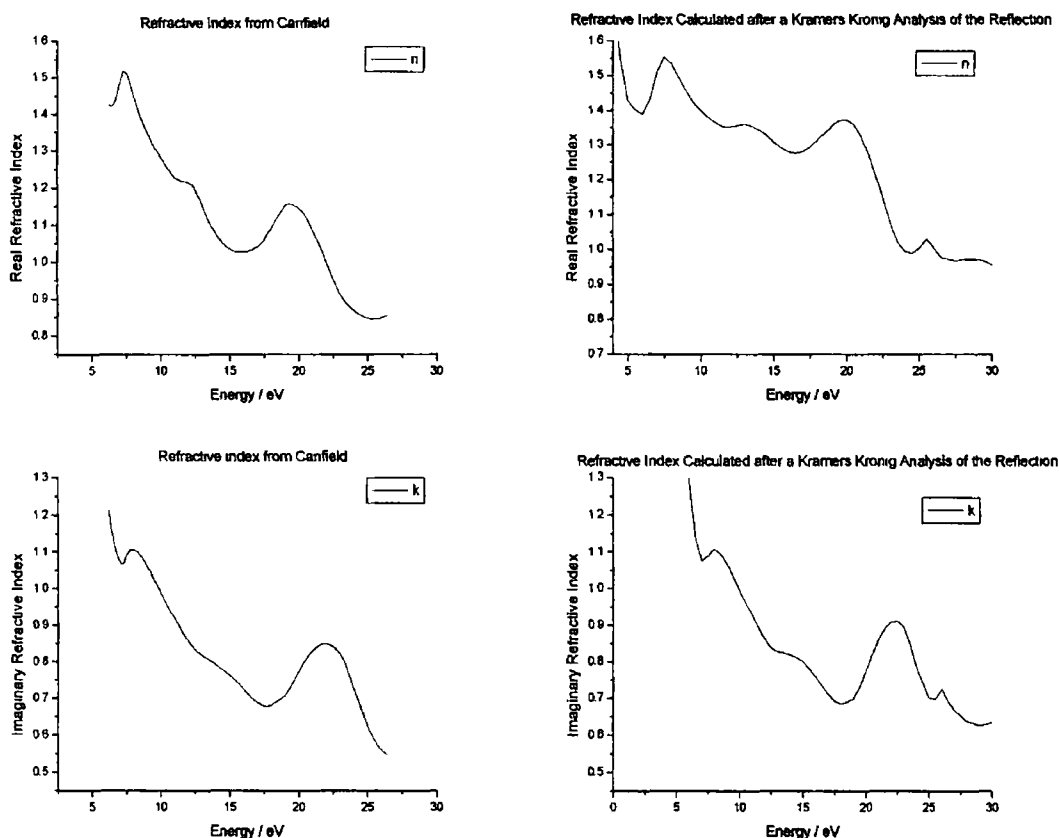


Figure 5-8 Results in the region examined by Canfield. The data on the left was measured by Canfield, data on the right was calculated using our Kramers Kronig analysis program on the reflection data

Figure 5-8 shows the results for the 5-27eV region. These are in good agreement with similar shapes and numerical value for both the real and imaginary refractive index. The error in height could be due to mismatched data. Mismatched data is usually caused by different techniques used to measure the optical constants and they result in a jump in the data. During analysis mismatched data can cause variations in the value of the optical constants or can be seen as unexpected peaks in the data like that seen above at 25.5eV.

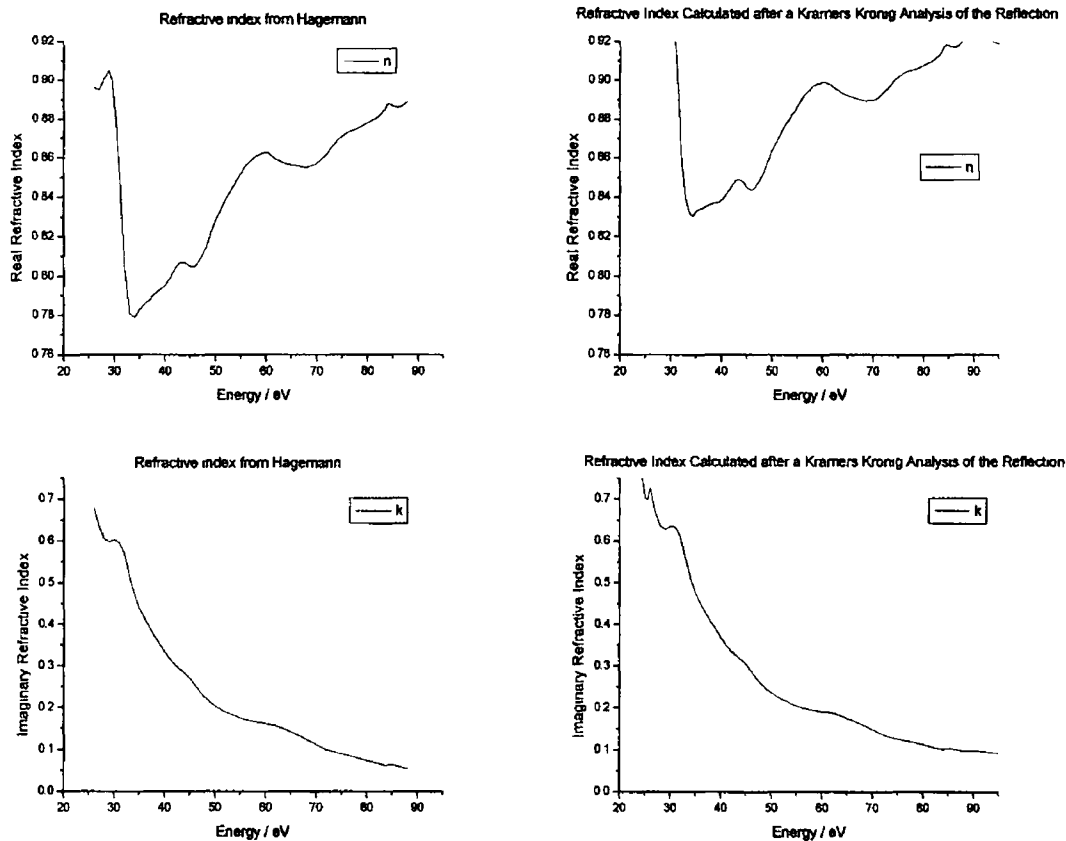


Figure 5-9 Results taken from the region examined by Hagemann The graphs on the left were measured by Hagemann, the graphs on the right are those calculated using the Kramers Kronig analysis program on the reflection data.

Figure 5-9 shows the data taken in the 26-88eV region. The match of the imaginary data is very good, however the real data is rather high. The height difference is once again most likely due to the mismatched data mentioned previously.

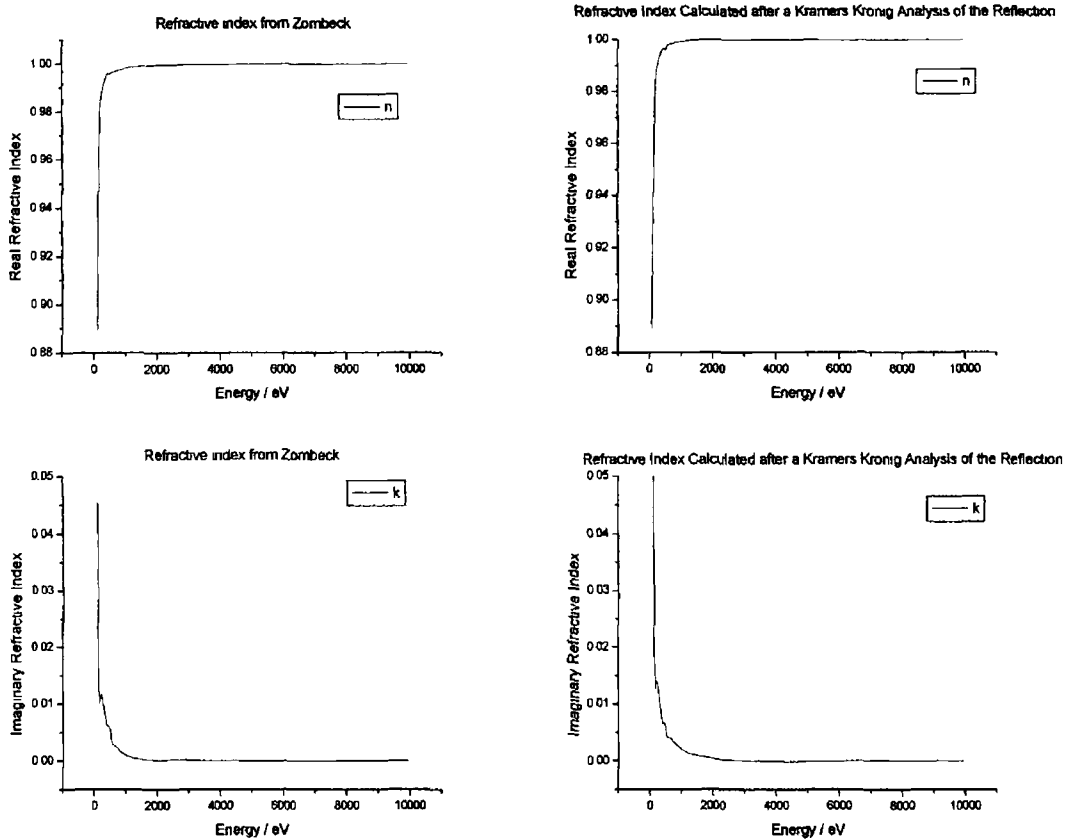


Figure 5-10 Results taken from the region examined by Zombeck. The graphs on the left are the results from Zombecks measurements

Figure 5-10 shows data taken in the 100-9919eV region and once again the similarity between both sets of graphs is encouraging

These results show the effectiveness of using data from other parts of the literature to increase the energy range used for a Kramers Kronig analysis. It was found that improvements in these values can be achieved if the data set is extended to 35 times greater than the region under investigation. For example when investigating a region from 1-30eV the set should be extended to at least 1050eV.

The inertial sum rule was applied to the entire data set and resulted in a verification factor of 2×10^{-3} . Such a result for the sum rule for our data set is indeed encouraging as it shows how accurate the program can be when using it with actual data. We can therefore confidently use it on any data we obtain from experiments see section 5.5.4.

5.2 *Calcium Fluoride Testing*

The experimental set-up was first tested on transmission measurements of Calcium Fluoride. Calcium fluoride was chosen as the first test material as it transmits at wavelengths greater than 125nm, and we could buy off-the-shelf windows of varying thickness. Having varying thickness gives an ideal way of determining the absorption coefficient if the thickness is the only variable that is changed the reflectivity is constant while the transmission varies with the thickness. This should provide us with an exponentially decaying graph whose decay constant is directly related to the absorption coefficient.

The windows in question were purchased from Focetek Ltd. These windows were placed in the analysis chamber and quite a few measurements were taken on them initially. Since the windows were used to test the analysis system, the wavelengths were chosen to be looked at were selected from the published data from [50]. The data was analysed by methods described in sections 4.2 and 4.3.1 to get the transmission/incoming ratio at eight wavelengths from 130nm to 200nm. The maximum and minimum wavelengths were then plotted against window thickness as shown in Figure 5-11.

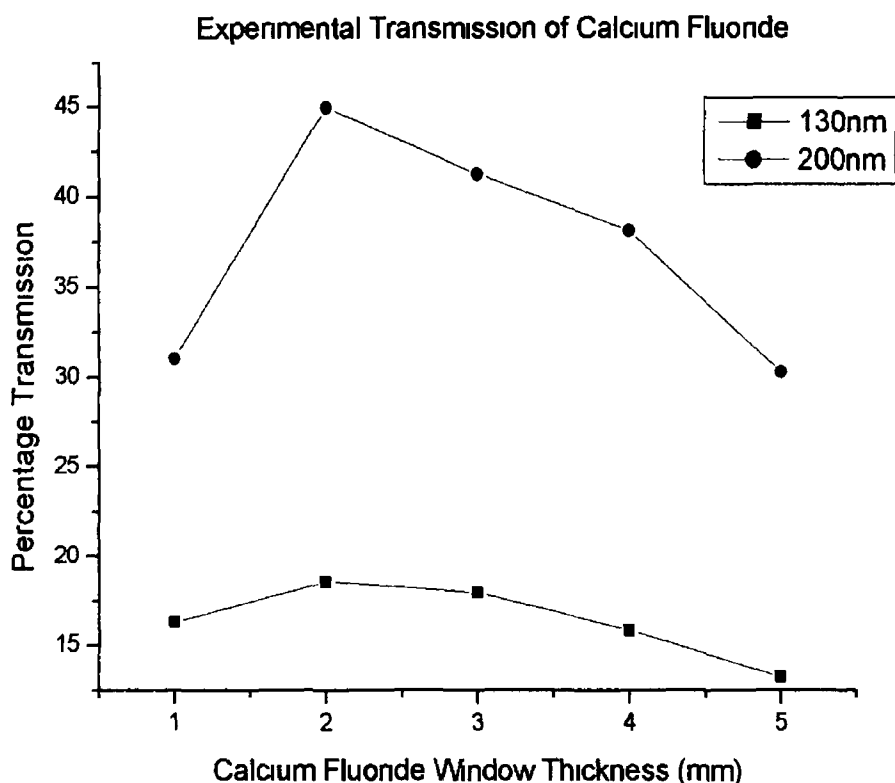


Figure 5-11 Graph obtained from the experimental data for transmission through all five calcium fluoride windows These results were taken without spectral filtering

The graph above shows two especially interesting features first, the transmission of the 1mm thick window is consistently lower than the two or three millimetre windows for both wavelengths and secondly, the level of transmission for both wavelengths is much lower than values in the literature According to [24], the transmission at 200nm should be close to ninety percent, which is clearly not the case for our measurements Foctek also provided a transmission spectrum for their calcium fluoride windows upon request, which is reproduced in Figure 5-12

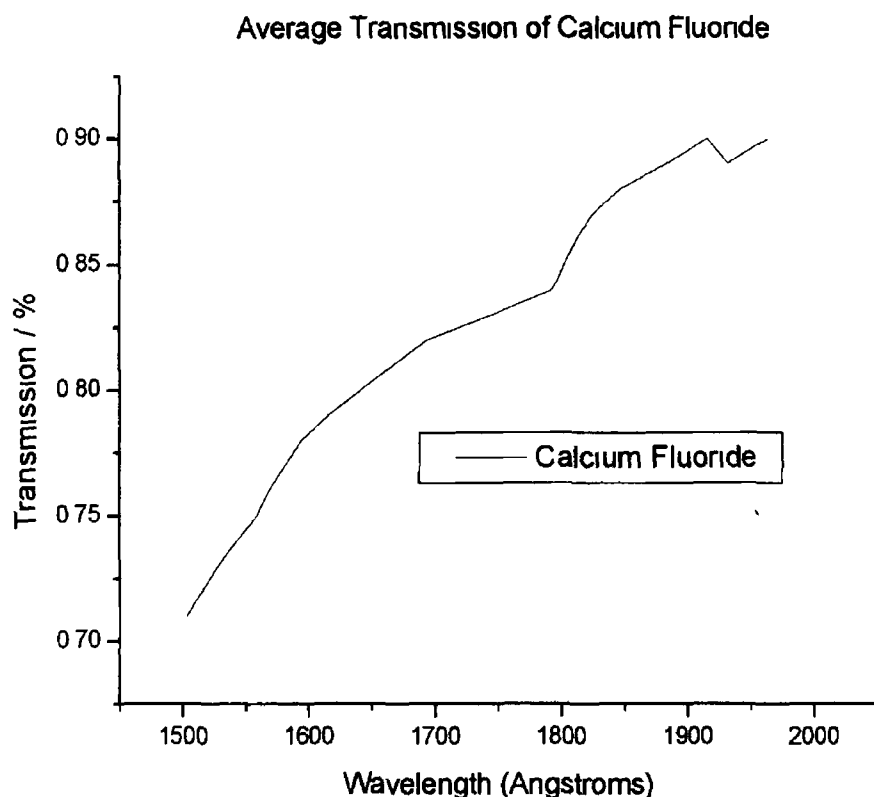


Figure 5-12 Average transmission of calcium fluoride windows as measured by the manufacturer. The thickness of this window is not known, however, the thinnest window they supply is 1mm thick

The graph clearly shows that the windows should have a higher transmission at 200nm. We surmised that the reason behind this discrepancy could be the addition of second order light from the monochromator, which would result in false counts for the incoming light (I). The calcium fluoride window has a transmission cut-off at about 125nm, which is 25nm higher than the second order light that would be produced when making measurements at 200nm. If there is a second-order contribution contained in the beam then the intensity of light being transmitted (T_0) through the windows at 200nm is correct, but the incoming light (I) is too high, this might cause the lower than expected transmission. This is summarised in equation (5.9)

$$\frac{T_0}{I} = \frac{T_0}{I_0 + I_{ho}} < \frac{T_0}{I_0} = T \quad (5.9)$$

where I_0 is the first order incoming intensity, I_{ho} is the higher order incoming intensity and T is the transmission of the sample at the first order wavelength

The problem of higher order light can only be solved with the appropriate use of filters to remove the second order light before the incoming light is measured

5.3 *Filter Testing*

A filter is a material that is used to remove something that is not required. In this case it is used to remove second and higher order light that is also present in the beam from the monochromator. The choice of the correct filter is essential. Ideally, the filter should not remove any of the first order light that is required for the experiment and all of the second and higher order light. The wavelength range of light used in the experiments on calcium fluoride is 125-200nm. An ideal filter for this is lithium fluoride as its transmission cut off is at approximately 104nm. For experiments on other materials the cut-off needed to go down as far as 30nm. The second order light contribution is so small at 30-45nm that no filter was needed, however, at greater wavelengths filtering is required. Helium gas can be used to filter out light below 50nm and argon gas can be used below 79nm. For both gas filters the length of the section in which the gas is leaked into the chamber is approximately two metres in length from the exit slit of the monochromator to the CCD camera on the analysis chamber. The gas is leaked into this section with the use of a needle valve just after the exit mirror chamber, this is at approximately the halfway position in the section.

5.3.1 *Lithium Fluoride*

Lithium fluoride transmits down to about 105nm as can be seen from the calculated from values obtained from [50] that are shown in Figure 5-13

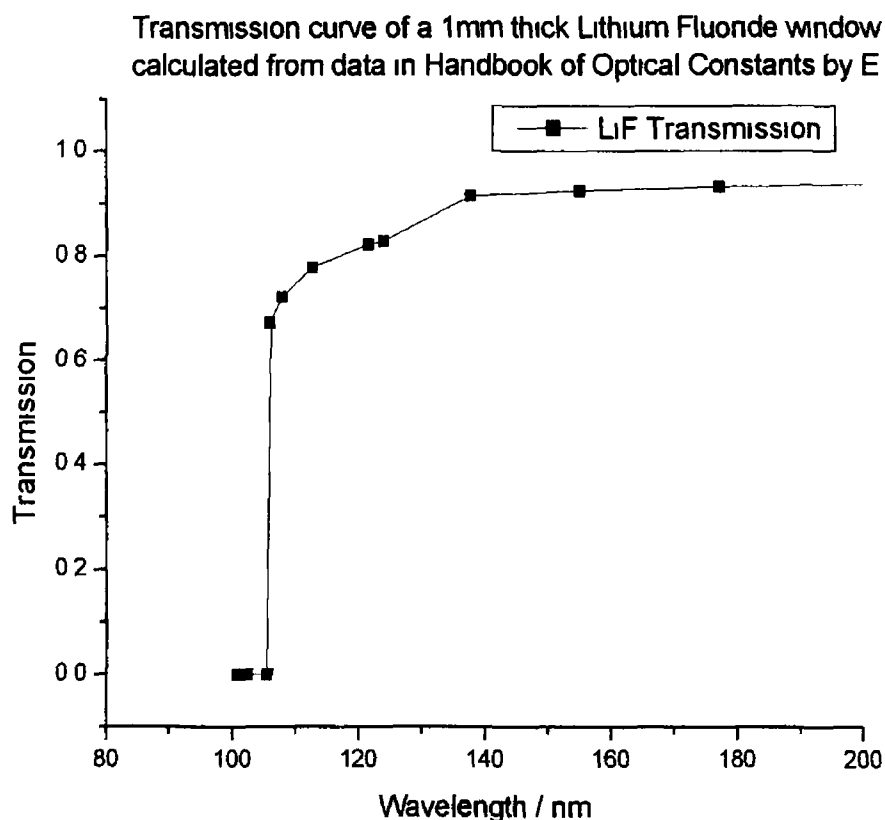


Figure 5-13 Transmission of 1mm thick window of Lithium Fluoride calculated from [50]

The calcium fluoride cut off is at about 124nm. According to the transmission graph, a lithium fluoride window should transmit about 80% of the incoming first order light at 124nm, but none of the second order light at 62nm. This means that lithium fluoride is an very good filter of second order light when making measurements from 120-200nm, which is the region of interest for calcium fluoride.

5.3.2 *Helium Gas*

Helium gas is one of the noble gases and does not react with any of the materials inside the vacuum chamber. The advantage of using helium gas as a filter

can be gleamed from Figure 5-14 above 50nm, it transmits essentially 100% of the light This graph was calculated using data obtained from Henke *et al* [20] The photoabsorption cross section (μ_a) can be calculated from equation (5 10)

$$\mu_a = 2r_0\lambda f_2 \quad (5 10)$$

where r_0 is the classical electron radius ($2.82 \cdot 10^{-15}$ m), λ is the wavelength and f_2 is one of the forward scattering factors listed by Henke [20] The transmission can then be calculated for each wavelength from equation (5 11)

$$T(\lambda) = \exp[-n\mu_a(\lambda)d] \quad (5 11)$$

where $T(\lambda)$ is the transmission of light of wavelength λ through a thickness d containing n atoms per unit volume and μ_a is the photoabsorption cross-section For an ideal gas n can be calculated from the ideal gas law in equation (5 12)

$$P = nk_B T_{gas} \quad (5 12)$$

where P is the pressure, k_B is Boltzmann's constant and T_{gas} is the temperature of the gas The temperature is known to be 300K (room temperature) and the pressure can be measured during experiments By substituting equation (5 12) into equation (5 11) we get a value for the transmission from equation (5 13)

$$T(\lambda) = \exp\left[-\frac{P\mu_a(\lambda)d}{k_B T_{gas}}\right] \quad (5 13)$$

The helium pressure was measured at the gas inlet, but this pressure does not represent the pressure in the entire section of pipe that the helium is contained in At each wavelength, the average pressure was calculated by measuring the transmission T , calculating μ_a from Henke's data [20], and substituting these values together with the measured path length $d=2.0$ m into equation (5 13) The difference between the gas inlet pressure and the equivalent pressure can be seen in Table 5-1

Table 5-1 Pressure comparisons for Helium

Gas Inlet Pressure (Pa)	Equivalent constant gas pressure (Pa)
18	1.4
37	3.8
56	7.6
75	10.8
94	14.1
112	17.3

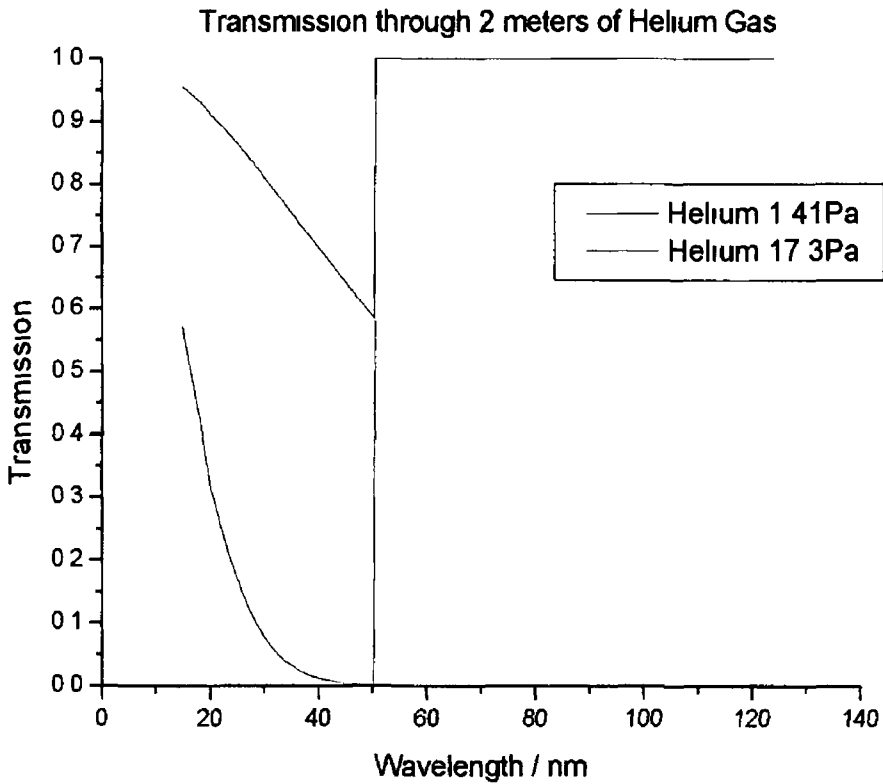


Figure 5-14 The transmission through a 2 meter thick volume of helium at the maximum and minimum gas pressures. The effect of discrete absorption lines is neglected.

Figure 5-14 shows that helium is transparent to wavelengths above 50nm and so with careful use it can be used as a filter from 50-100nm with the only exception being those wavelengths where discrete transitions may take place, these are tabulated in [52] At the lower pressures the efficiency of such a filter is much reduced For example if a measurement is taken at 60nm with a helium pressure of 1.41Pa, 80% of the second order light is transmitted while at the highest pressure of 17.8Pa almost no second order light (8%) is transmitted

It is clear that even at the highest pressure not all the second order light is removed, especially at lower wavelengths. However, if a higher helium pressure were used the strain on the vacuum pumps would be too great. An increase in pressure would also allow gas to enter the plasma chamber, which would result in a change in the plasma as it would be expanding into a gas as opposed to vacuum. To ensure this does not happen a maximum average pressure of 17.8 Pa was decided upon.

With a maximum pressure established, the gas pressure could be brought up in steps and at each step a set of measurements could be taken. This reduces the load on the pumps and allows us to extrapolate the amount of transmission that would occur at a much higher pressure. This extrapolation follows from equations (5.11) and (5.12) in which the transmission of second order light decays exponentially with the increase in pressure.

The first order light remains constant with the pressure change, thus the asymptote of the curve gives the counts due to the first order light. The result of this method can be seen in the black plot in Figure 5-15. It is clearly shown that the second order contribution for light at 77.5 nm is significantly higher than the first order contribution, which amounts to only 2565 counts. It must be noted that for this fit there is a non-zero error in the measurement of the gas pressure, however since this is not taken into account during the curve fitting it is not represented in the graph. The exponential decay of the second order can be calculated by using the equivalent pressures (Table 5-1). Using these pressures the number of atoms per unit volume may be calculated and then the associated transmission can be calculated using equation (5.13) (blue plot in Figure 5-15). The plot can then be curve fitted to give us the rate of decay of the second order light at the gas pressures used. This decay may then be used to calculate the asymptote value C_1 of the data in section 5.5.2.

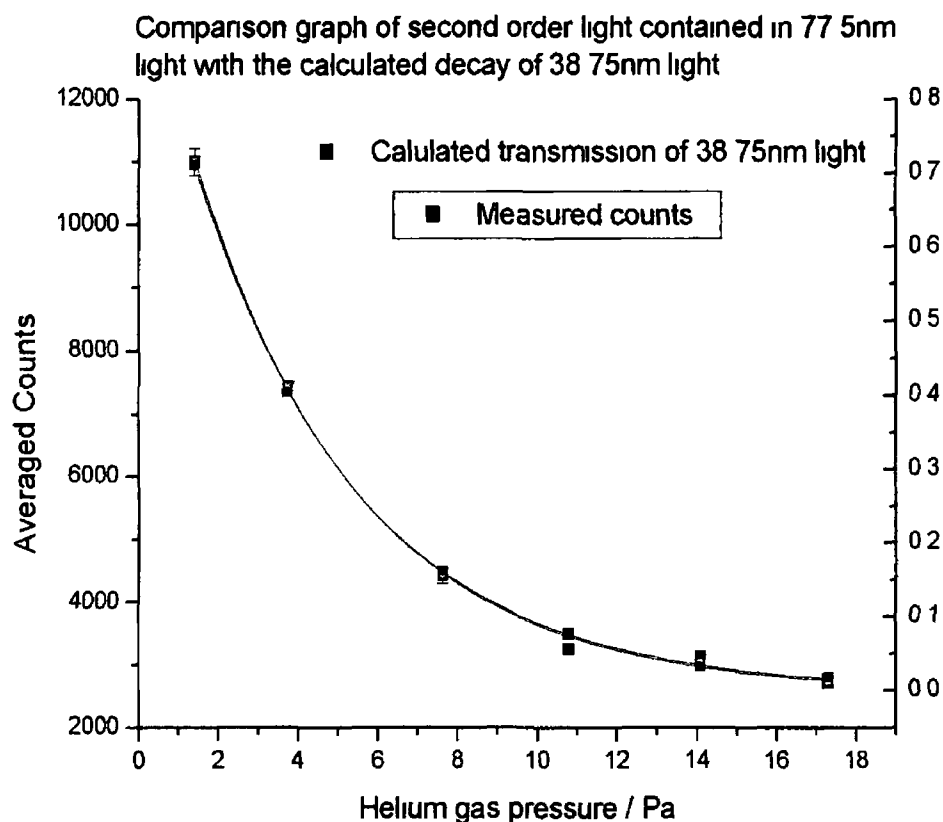


Figure 5-15 Graph showing the decay of second order light with increasing helium gas pressure. The blue points show the calculated counts for the 38.75nm light. Both graphs were separately curve fitted prior to merging with the red curve being the fit of the measured counts.

This value is then used as the true incoming count. True reflected and transmitted counts are evaluated in a similar fashion.

The quality of the single exponential fit is encouraging as it confirms that the increase in gas pressure does not noticeably affect the first order contribution. The inlet pressure of the gas is measured using the default nitrogen pressure reading on the pressure gauge controller. The correction factor between measuring pressures of nitrogen and helium is 1.1 [53]. This correction factor was included in all pressure readings for helium.

5.3.3 Argon Gas

Helium gas is only useful as a filter for second order light below 50nm. In order to filter out second order light at higher wavelengths another filter was needed. This filter was argon gas. Its transmission was also calculated in the same manner as helium using data from Henke *et al* [20]. The resulting calculation of the transmission through a 2 metre section of pipe containing argon gas can be seen in Figure 5-16.

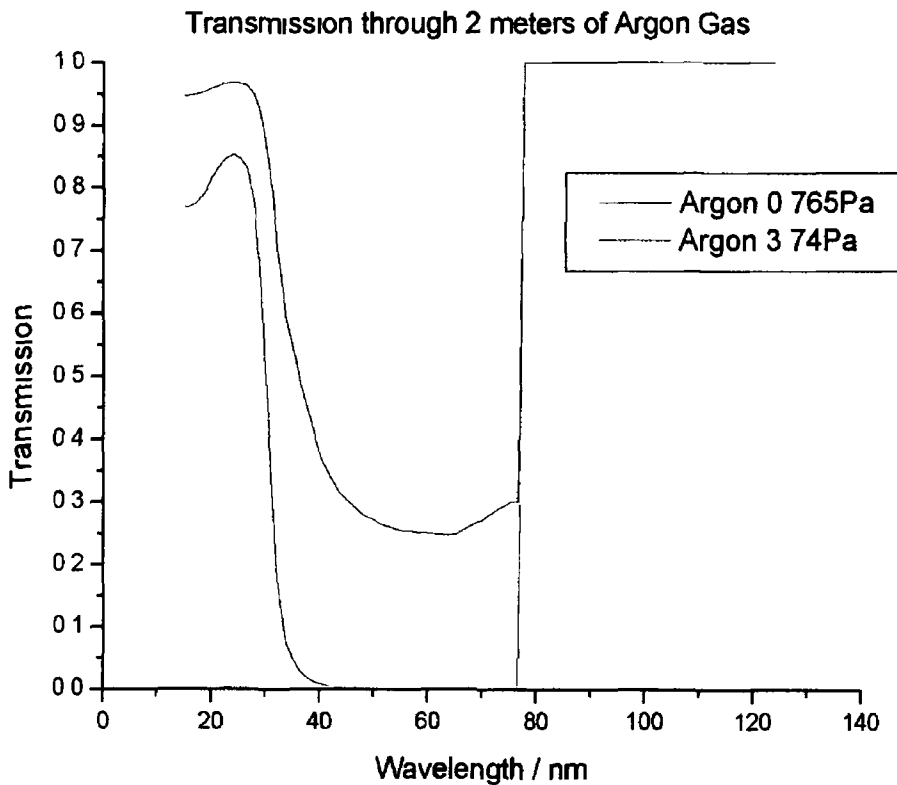


Figure 5-16 Transmission through a two metre thick volume of Argon gas at the maximum and minimum pressures. The minimum transmission of the 3.74Pa plot is 0.009.

The graph shows that argon gas is transparent for wavelengths above 79nm. This means that argon may be used as a filter for measurements from 79-156nm. It can be seen that for low-pressure measurements at 80nm 100% of the first order and approximately 38% of the second order light is transmitted, while at the higher

pressure approximately 1% of the second order is transmitted. Therefore argon is a good filter for the region from 79-156nm. However, as in the case for helium, the strain on the vacuum pumps must be considered and so for each wavelength to be measured, several pressures must be used and then plotted. An exponential curve may then be fitted to the plot to determine the asymptote of the first order light. An example of measurements taken in this way can be seen in the black plot in Figure 5-17. The decay rate of the second order light can be calculated in the same way as was done for the helium filter, this plot is the blue plot in Figure 5-17. The inlet pressure of the gas is once again measured using the default nitrogen pressure reading on the pressure gauge controller. The correction factor between measuring pressures of nitrogen and argon is 1.5 [53]. This correction factor was included in all pressure readings for argon.

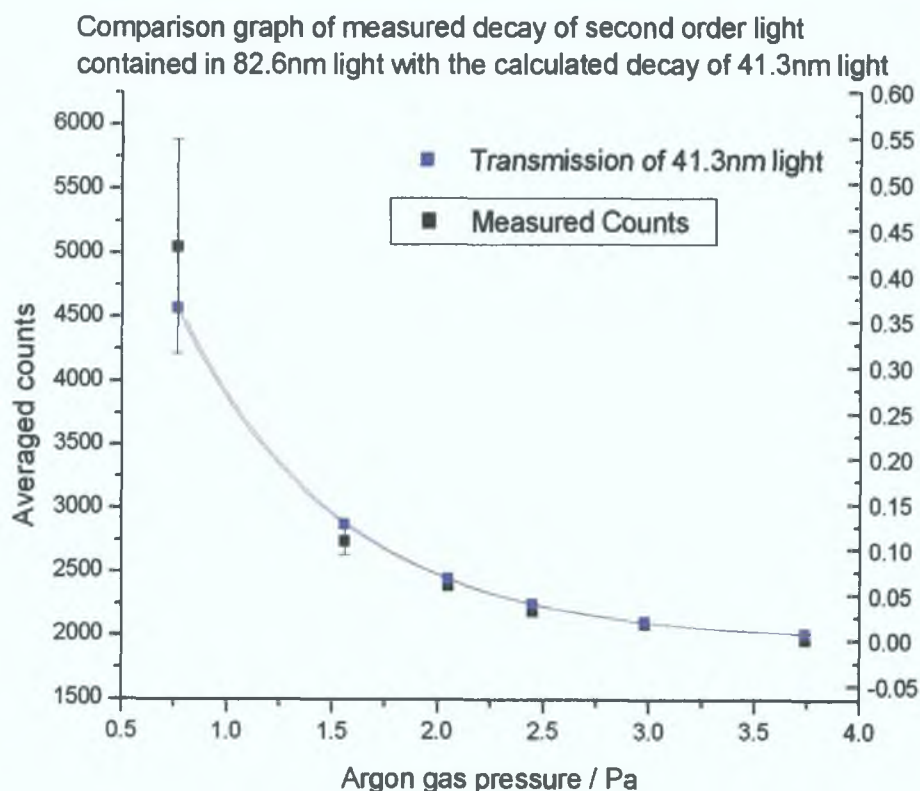


Figure 5-17 Graph showing the decay of second order light with increasing argon gas pressure. The blue points show the calculated counts for the 41.3nm light. Both graphs were separately curve fitted prior to merging with the red curve being the fit for the measured counts

5.4 Calcium Fluoride with a Filter

With a lithium fluoride filter available and in place the experiment on the calcium fluoride windows could be continued. The same conditions were set on all the components and the testing of the calcium fluoride at 130nm and 200nm was measured. The results of the data on this new data can be seen in Figure 5-18.

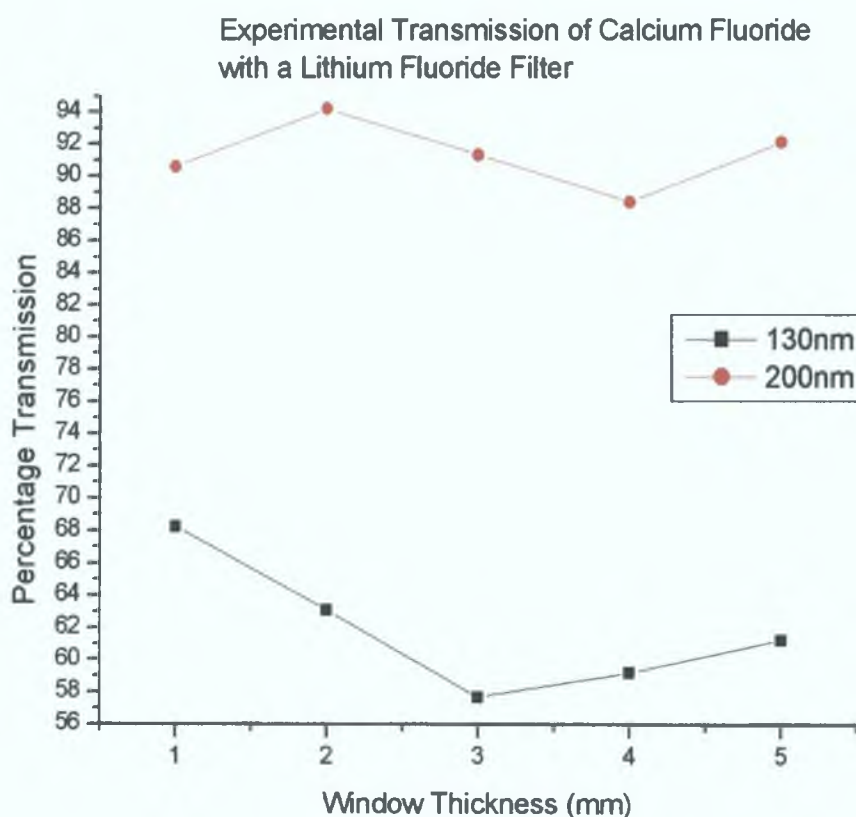


Figure 5-18 Experimentally determined transmission of the calcium fluoride windows when a lithium fluoride filter was used. Comparison with Figure 5-11 shows that the values have greatly improved.

The filter has provided conclusive proof that second order light is entering the system and so filtering must take place in the required regions as stated in section 5.3. A rigorous analysis of calcium fluoride can now be done for wavelengths between 120-200nm. A certain amount of improvement to the analysis was carried out to increase

the accuracy before the next set of experiments. This involved improving the image alignment and incoming image interpolation. The results of the next set of experiments can be seen in Figure 5-19.

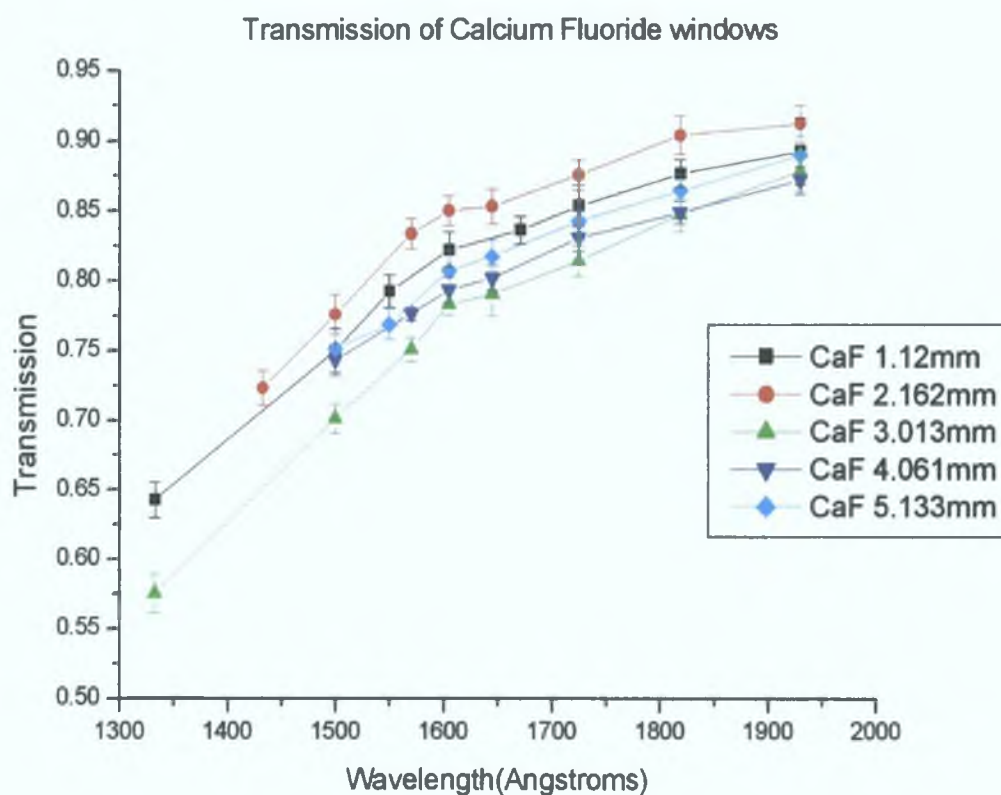


Figure 5-19 This shows the transmission of all five windows after the experiment. Note the order of transmission from highest to lowest: 2mm, 1mm, 5mm, 4mm, 3mm thickness.

Figure 5-19 is in good qualitative agreement to the reduction of transmission of calcium fluoride in Figure 5-12. However it also shows a disturbing picture where the relative amount of transmitted light is obviously wrong. The data was checked and reanalysed to ensure no calculation errors were made, yet still the transmission from highest to lowest is consistently 2mm, 1mm, 5mm, 4mm, 3mm windows. This data was sent to Foctek with the request of an explanation. Upon investigation by staff at Foctek it was discovered that the windows were not cut at the same crystal orientation as had been requested and there was a possibility of different levels of contaminants.

The windows were therefore not suited to such fine transmission measurements. Continuing using the calcium fluoride windows to extract optical constants would be a fruitless effort.

Despite this disappointing result, the measurements were useful in that the experiments did allow us to do a full test of the analysis procedure and to refine the steps required to efficiently use the experimental system. We put this knowledge to good use by proceeding to the next step of the project. This step was the creation of our own films that we will use to measure the optical constants of Aluminium.

5.5 *Aluminium Thin Films*

Aluminium is a material that has a history of interest surrounding it. It has been widely analysed, especially for its optical constants. However, the region from 30-100nm has rarely been looked at. Only a few authors have published data in this region and all have noted the lack of experimental measurements and the requirement for more.

Some measurements and theoretical calculations have been made on the transmission of aluminium in the VUV and soft X-ray regions. A detailed list of the atomic scattering factors for aluminium was compiled by Henke *et al* in 1993 [20]. He used theoretical models along with transmission measurements to produce a table of the atomic scattering factors from 0.041-24nm (50-30000eV).

The data just below the L edge was remeasured by Gullikson *et al* in 1994 [19]. His concern was that an oxide layer might have contaminated the previous measurements. They eliminated this possibility by carrying out transmission measurements on several films of aluminium of various thicknesses. For each wavelength they plotted the transmission (T_0/I_0) measurements against the thickness.

This resulted in an exponentially decaying graph whose decay constant contained the absorption coefficient of aluminium. The removal of the effect of an oxide layer in this way reduced the accepted value of the mass absorption coefficient of aluminium by a noticeable amount (as much as 50% less in some areas) from that of Henke *et al.*

In 2002 Keenan *et al* measured an aluminium step filter in the same way Gullikson *et al* did previously except they used two lasers to achieve two accurate wavelengths. Surprisingly, their data corresponded with the data previously tabulated by Henke *et al* but not with that of Gullikson *et al*.

It is clear that more data in this interesting region is needed; we therefore selected aluminium to test the experimental and analytical system, as we could measure some of the wavelengths used by Gullikson *et al* and further extend it into the VUV. The aluminium films were created as described in section 3.4 and were supported by transmission electron microscope (TEM) grids. In spite of this, it is customary to refer to such films as freestanding.

The spatial resolution of the beam was tested during the experiments and it was found that we obtain a peak percentage (~90%) transmission from the edge of a film at approximately 2 to 2.5 superpixels. This is clearly shown in the two cross section graphs extracted from a sample Figure 5-20.

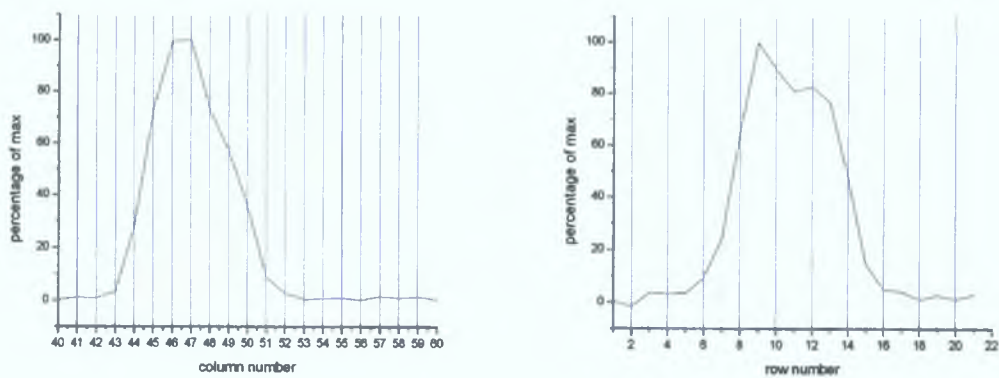


Figure 5-20 Cross section graphs from a transmission image. This shows the spatial resolution of the system to be approximately 2 super pixels.

5.5.1 TEM Grid Transmission

In order to use the TEM grids a certain amount of detail needed to be known about them. The only possible obstacle for their use would be how well they transmitted in the VUV. To check for this, measurements were carried out on the grids the result of these experiments are shown in Table 5-2. As can be seen the average transmission throughout the wavelength range is 49%.

Table 5-2 Transmission of new 200 grid

Wavelength (nm)	Transmission	error
30.2	0.498	0.009
35.4	0.497	0.004
40.0	0.497	0.006
44.2	0.491	0.006
49.6	0.486	0.004
68.8	0.494	0.007
88.5	0.478	0.017

Thus the grid removes a constant fraction of the incoming beam. This confirms that the bars forming the grid absorb all the incident light regardless of its wavelength.

The size of the grids were only 25mm in diameter while the beam was a 4x4mm square, with this in mind the incoming image had to be cropped in order to compare it with the image transmitted through the grid. The alignment procedure described in section 4.2 allowed alignment and cropping of the incoming image with the image being transmitted through the grid. The resulting aligned images can be seen in the set of sample images shown in Figure 5-21. These images show how much of the beam passes through aluminium holder and the grid at the center of it.

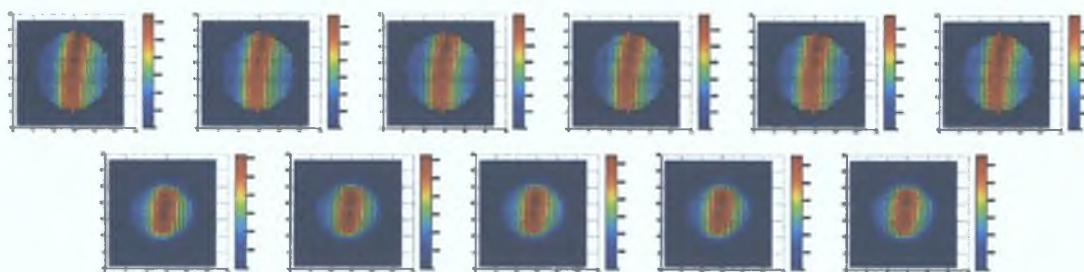


Figure 5-21 Images taken during experiments on the 200 grid at 49.6nm. The top row is the incoming images and the bottom are the transmission images through the grid.

5.5.2 Free standing Aluminium on TEM Grids

Seven aluminium films of different thickness were successfully deposited onto the salt crystals and placed onto the TEM grids. Since aluminium oxidises very rapidly, even under ultra high vacuum conditions [13], it was deemed unfeasible to try and carry out the experiments so fast that an oxide layer could not form. Instead, we let each film oxidise for the same duration of three days to ensure a similar build up of aluminium oxide on their surface. Each film was then placed inside the analysis chamber for transmission experiments. Each film was analysed at 17 wavelengths from 30.2-88.5nm using appropriate filters as discussed in section 5.3. All those measured using a gas filter required six sets of data (at six different pressures) to obtain the first order asymptote as described in section 5.3.2. Figure 5-22 shows a typical set of images taken of the 21.5nm thick film.

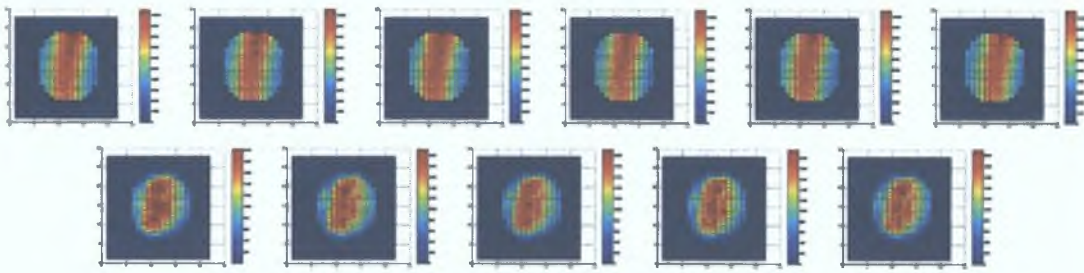


Figure 5-22 Incoming and transmitted beam images at 49.6nm with a 21.5nm thick film.

Some of the films also had unwanted characteristics that needed to be dealt with separately. These characteristics showed up in the form of holes in the film. Figure 5-23 shows the images taken of the 9.5nm thick film in which there is a notable hole. Thickness measurement calculations for this film can be found in section 5.5.3. The top six images show the incoming beam after a transmission mask was applied under the criteria stated in section 4.2. The bottom 5 images show the transmission through the film.

The base of this film contains what looks like a region of greater light intensity. Such an increase in intensity is not resident in the incoming beam and so the region must be a region that absorbs less of the light. This can only be explained as a hole in the sample due to the fact that it was present at all wavelengths and was further verified by visual inspection when the film was removed from the analysis chamber. This is easily removed from all the images taken of the 9.5nm thick film at all wavelengths. The description of how this is done can be found at the end of section 4.2.

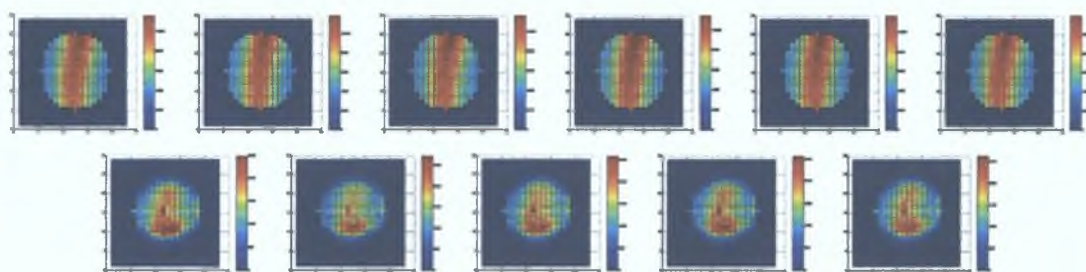


Figure 5-23 Pictures taken of the 9.5nm thick film at 49.6nm. The hole at the bottom of the film is clearly visible

These are but two sets of images taken at a wavelength of 49.6nm; all other images taken at this wavelength may be found in Appendix B to show a sample of the type of images gained. The removal of portions of the images was only carried out after all images of that film were examined and it was determined that a hole was indeed present in the film. With the removal of the holes the images were once again checked for any anomalies. If no anomalies were present the images could then analysed as per the steps stated in section 4.3.

If a gas filter was used the average transmission taken at each gas pressure must be evaluated according to the procedure described in section 4.3.3. The analysis requires that the incoming and transmission averages be plotted against the gas pressure. An exponential curve can then be fitted to it to obtain the asymptote value of the average incoming and transmission counts at a higher gas pressure (i.e. the first order counts). The graphs associated with the 21.5nm thick film taken at a wavelength of 82.6nm can be seen in Figure 5-24.

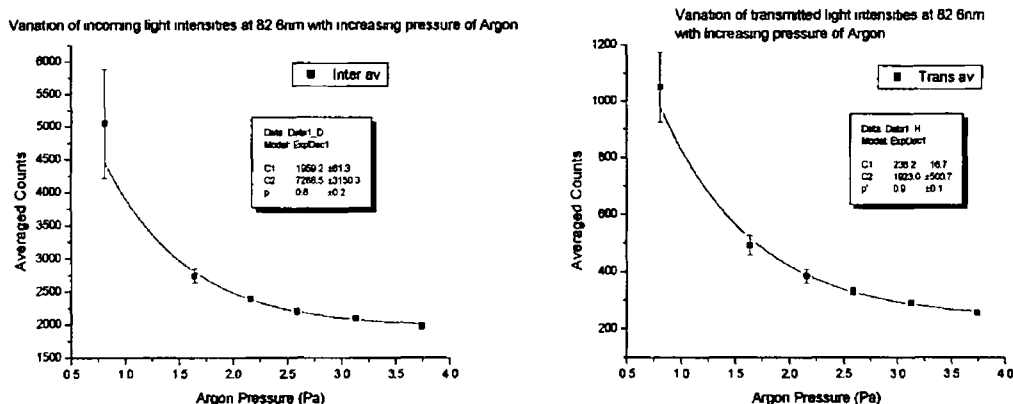


Figure 5-24 On the left is the incoming light measurements plotted against increasing pressure and on the right is the associated transmission plot.

An exponential curve of the form given in equation (5.14) was fitted to both curves

$$C = C_1 + C_2 \exp\left(-\frac{p}{p'}\right) \quad (5.14)$$

where C_1 is the counts of the asymptote representing the first order light, C_2 is a multiplication factor which represents the value of the second order light with no filtering and p is the pressure. Applying the equation resulted in a decay constant (p' in the table) as shown in the graphs above of 0.76 ± 0.15 for the incoming plot and 0.85 ± 0.13 for the transmission plot. Such curves were fitted to all the graphs so that the decay constant of each film at each measured wavelength could be examined.

For each wavelength we had a list of seven decay constants (relating to each film analysed) the majority of these were consistent within experimental tolerances. However, there were a few that gave an unrealistic result mainly due to an erroneous point in the graph that was fitted. When such points were removed from the fits it resulted in an improvement in the standard deviation of the decay constant of the gas at each wavelength. In order to reliably use this technique the same decay constant must be used for all graphs at a particular wavelength. Two options are available to achieve a single decay constant: the first is that which was mentioned above, while the second is a semi-theoretical fit, which could be calculated from the average gas

pressure used at each wavelength. For example at 82.6nm six transmission measurements for each film at each pressure are used, these are averaged to give us the five transmission values representing each of the six pressures. These transmission values are used to calculate the number of gas atoms in the chamber, which leads us to the amount of absorption taking place by the gas in the chamber at each pressure. This absorption is used to generate a graph that is curve fitted to give us our new decay constant to be used in the curve fitting for all the films analysed at 82.6nm. When this decay constant is applied to the graphs above they then become those in Figure 5-25.

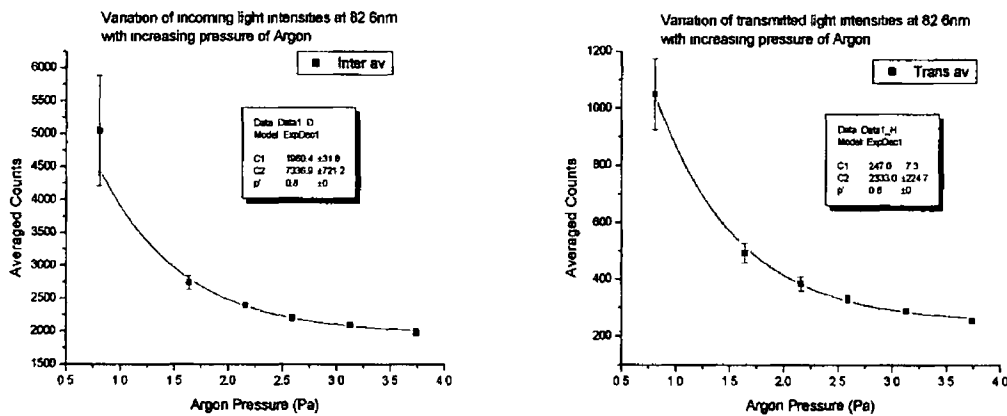


Figure 5-25 Plots of film f at a wavelength of 82.6nm with a constant decaying (p') exponential curve fit.

Applying such a technique increased the consistency of the result for all the films and allowed for a more reliable value for the asymptote to be determined for each film. In the sample above the asymptote value of the incoming changed from 1959 to 1960 but the error in this value was halved from ± 61 to ± 32 . Equally the transmission value changed from 236 to 247 and once again the error is halved from ± 16 to ± 7 . The asymptote values of the transmission could then be divided by the incoming for use in finding the absorption coefficient in section 5.4.4.

5.5.3 Thickness Measurement

As mentioned in section 4.4.1 the thickness is very important for calculating the absorption coefficient in the samples. All the results from the thickness monitor, Profilometer and AFM shall be given in this section.

5.5.3.1 Thickness Monitor

The frequency of the quartz crystal was noted before deposition started and when it finished. These values for the frequency can be seen in

Table 5-4 along with the result of the calculation using equation (4.4) with the following constants

$$T_f = \left(\frac{D_q}{D_f} \right) \left(\frac{N_q T Z_f}{\pi Z_q} \right) \tan^{-1} \left(\frac{Z_q}{Z_f} \tan \left(\pi \left(1 - \frac{T_q}{T} \right) \right) \right) \quad [4.4]$$

Table 5-3 Constants for use with crystal thickness monitor

D_q	2.648 gcm^{-3}
D_f	2.7 gcm^{-3}
Z_q	$(883400 \text{ gcm}^{-2} \text{ s}^{-1})$
Z_f	$817000 \text{ gcm}^{-2} \text{ s}^{-1}$
N_q	166800 Hzcm^{-1}

Table 5-4 Calculation of thickness of films a-g using thickness monitor equation

	Original Frequency (Hz)	Frequency after (Hz)	Thickness (nm)
Film a	5678970	5678175	40.3
Film b	5678222	5677616	30.8
Film c	5677290	5676989	15.3
Film d	5677106	5676470	32.3
Film e	5676603	5675407	60.7
Film f	5674500	5674000	25.4
Film g	5673870	5673470	20.3

Due to the thickness of the samples we were able to observe transmission of varying degrees in visible light. A visual inspection could be then carried out on some microscope slides that were deposited on at the same time as the thin film substrates.

(the sodium chloride crystal used as substrates were attached to similar slides) The visual inspection allowed us to estimate the ranking of thickness of the films This order coincided with the order calculated in Table 5-4 The slides were also used for the next two thickness measurements During deposition the slides were positioned beside the slide containing the sodium chloride substrates Both of these were at a height of thirty centimetres from the evaporating element for uniform deposition to occur over both slides

5.5.3.2 *Profilometry*

The second independent measurement of the thickness of the films was made using a profilometer Several measurements of each sample were made and the thickness values were averaged to obtain the data in Table 5-5

Table 5-5 Thickness Measurement of films a-g using the Profilometer

	Film Thickness (nm)
Film a	41.1
Film b	40.2
Film c	15.3
Film d	35.8
Film e	43.2
Film f	33.9
Film g	19.1

The measured thicknesses shown in Table 5-5 are in the same order as those obtained with the thickness monitor The data is however at the limit of the detection range of the profilometer Especially the smaller thickness films, as there is a strong possibility of high errors With this in mind it was decided to use a more sensitive detection apparatus namely an atomic force microscope

5.5.3.3 Atomic Force Microscopy

When analysed according to section 4.4.1.3, the images are flattened and the cross sections of the images taken so that thickness values can be extracted by using curve fitting. An image of one film from the AFM can be seen in Figure 5-26.

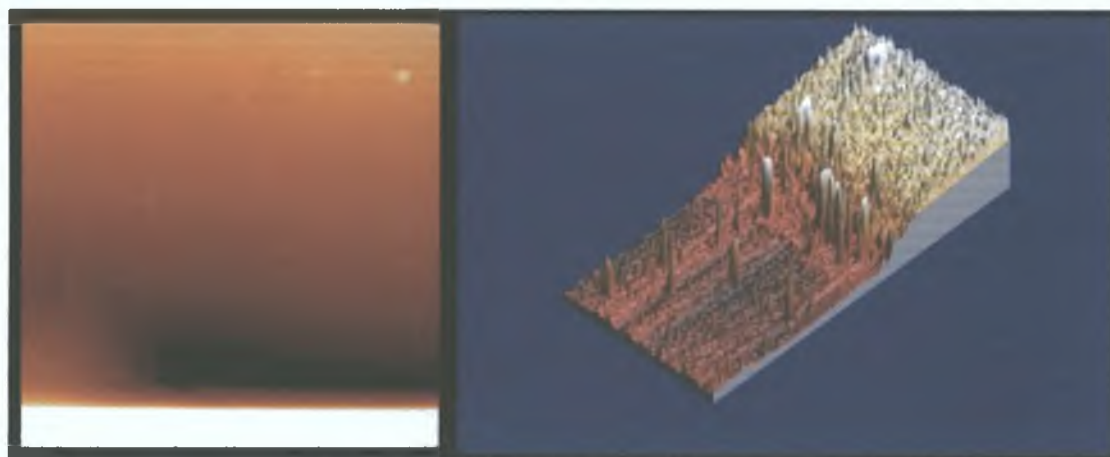


Figure 5-26 AFM images of film e. The image on the left is the original AFM image. The 3D representation is of the top half of the image due a large contaminant on the bottom left of the scanning region.

The other six films may be seen in Appendix B. The height measurement was obtained by taking sample lines across each image and finding the difference between the glass and the film, the results can be seen in Table 5-6

Table 5-6 Results of AFM measurements

Sample number	Thickness (nm)
Film c	9.5
Film g	18.6
Film f	21.6
Film d	28.7
Film b	42.1
Film a	54.7
Film e	60.6

5.5.4 *Absorption Coefficients*

The combination of all the thickness measurements is shown in Table 5-7. This data can then be used with the transmission measurements in section 5.5.2 to determine the absorption coefficient of aluminium.

Table 5-7 Results of all the thickness monitor measurements

	AFM Thickness (nm)	Profilometry (nm)	Thickness Monitor (nm)
Film c	9.5	15.3	15.2
Film g	18.6	19.1	20.3
Film f	21.6	33.9	25.4
Film d	28.7	35.8	30.8
Film b	42.1	40.2	32.3
Film a	54.7	41.1	40.3
Film e	60.6	43.2	60.7

With three different methods of measurement at our disposal it is clear that each method gives a similar ordering but different numerical values for the thickness. Due to the destructive nature of the profilometer and the errors due to the detection range, its measurements are expected to have the greatest error. Measurements on films a, b and c with the thickness monitor took place with a heavily loaded oscillating crystal in the monitor. The material deposited on the crystal occurred prior to our deposition of aluminium and so the material was not known. This meant that some errors were highly likely to occur. The extra material on the crystal would change the original natural frequency of the crystal. This crystal was changed after the third deposition. This may explain the difference in measurement between it and the AFM measurements for the first 3 films made. The thickness of films d-g measured with the AFM and thickness monitor are in good agreement. The AFM measurements were chosen as they were taken under identical conditions.

The transmission data for each sample is plotted against its measured thickness for each measured wavelength. The equation for the graphs comes about by

equating equation (4 3) with equation (5 11) and applying the identity in equation (5 15)

$$n\mu_a = \rho\mu \quad (5 15)$$

$$T = T_0 \exp(-\alpha d) = T_0 \exp(-\rho\mu d) \quad (5 16)$$

where T_0 is the light transmitted through the interface, α is the linear absorption coefficient, d is the sample thickness, ρ is the material density and μ is the mass absorption coefficient. If we take the negative of the natural log of T/T_0 and plot this against the thickness we get equation

$$\frac{-\ln(T/T_0)}{d} = \alpha = \rho\mu \quad (5 17)$$

This is the equation for the slope of the graphs that can be seen in Figure 5-27 as an example of a sample using no filter, in Figure 5-28 as an example of a sample using a helium filter and finally in Figure 5-29 for a sample utilising an argon filter. All the graphs can be found in Appendix B. Only five films were used as it was found out later that two of the films were supported by a different type of grid than the other five, these two were omitted from the analysis.

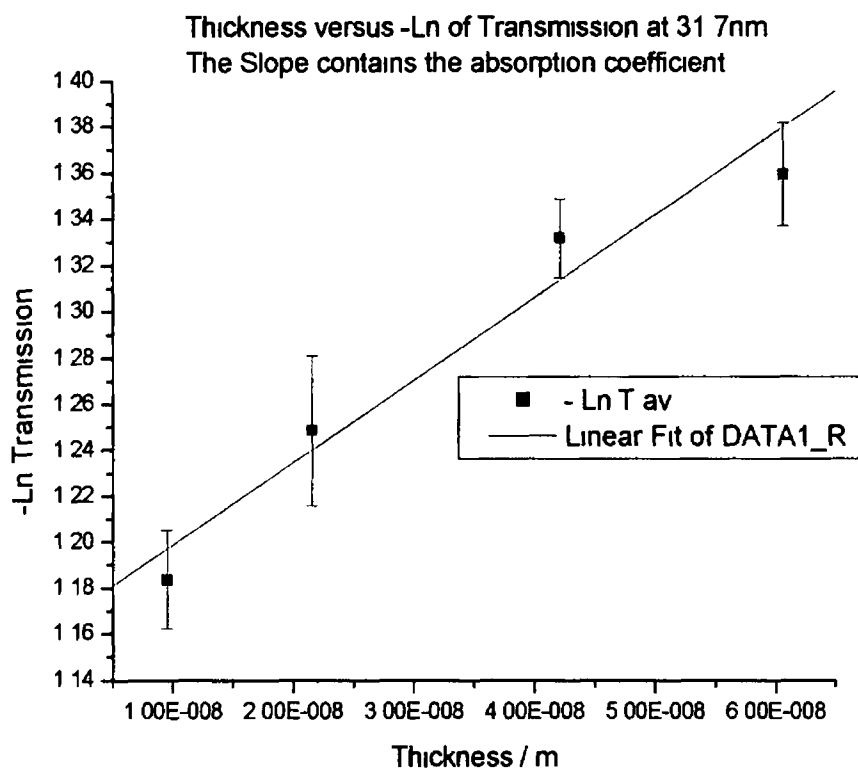


Figure 5-27 Plot of $-\ln T$ versus thickness of aluminium film at 31 7nm. No spectral filtering was used for obtaining this data.

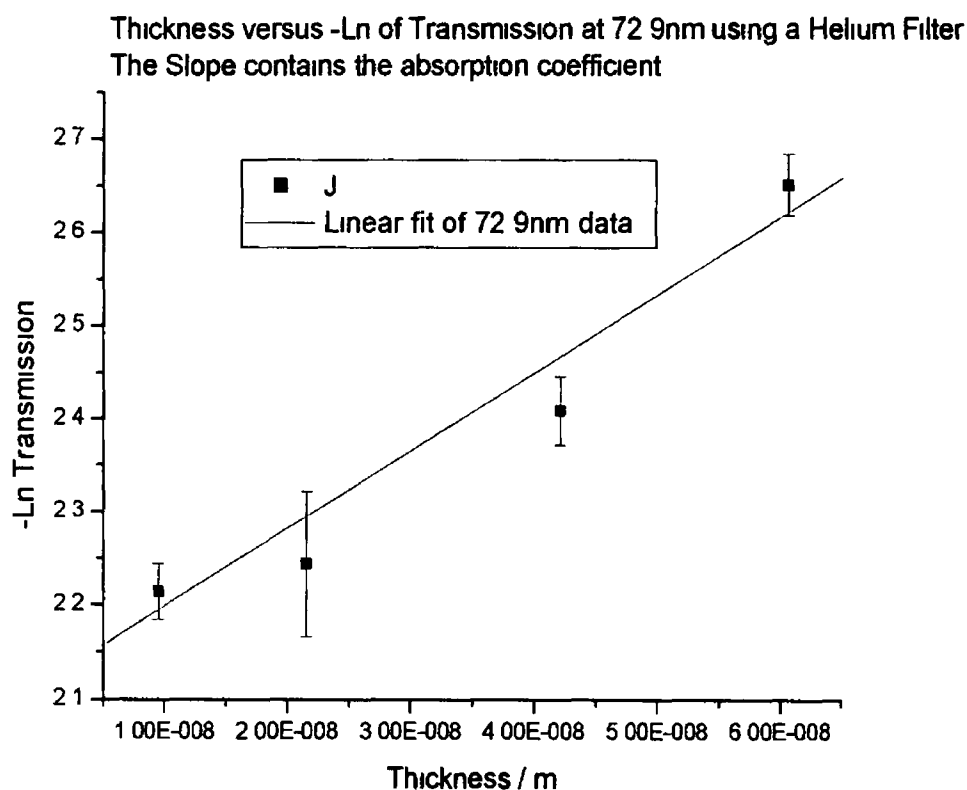


Figure 5-28 Plot of $-\ln T$ versus thickness of aluminium film at 72 9nm. A helium gas spectral filter was used to obtain this data.

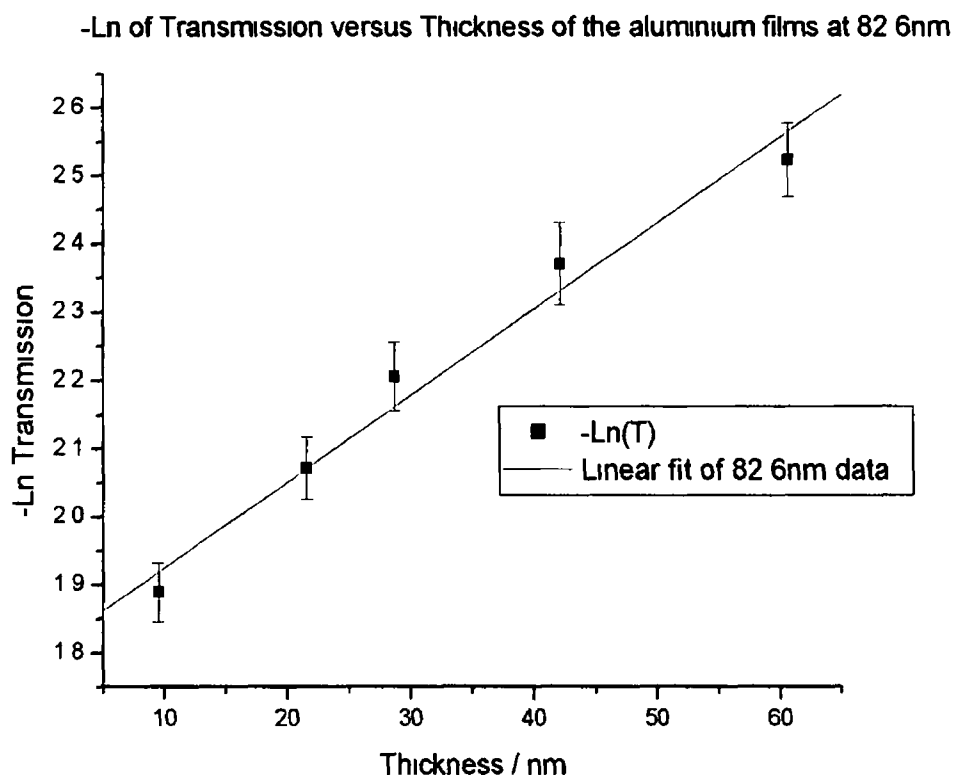


Figure 5-29 Plot of $-\ln T$ versus thickness of aluminium film at 82.6nm. An argon gas spectral filter was used to obtain these results

The slope is calculated by first noting the transmission T of a material, which is given by equation (5.16). It is clear from the graphs that the axial intercept is not at 0. This is explained by the absorption caused by the TEM grid on which the films are being supported and the reflection that occurs at the surface of both the aluminium film. Previous experiments with the grids show that it absorbs 49% of the light passing through it at the wavelengths in question.

An oxide layer readily forms on aluminium once it is exposed to oxygen and in our case all films were purposely exposed for three days to give a uniform oxide layer on both sides of the film such as that shown in Figure 5-30.

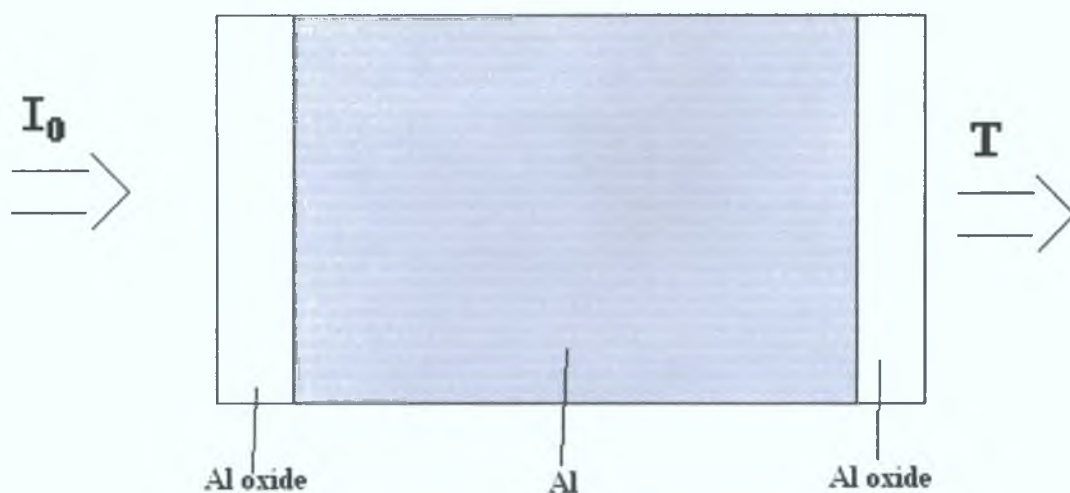


Figure 5-30 Diagram of oxide layer buildup on an aluminium film.

Fortunately we use the same grid and oxidation time for all the samples, resulting in the slope being directly related to the thickness of the samples. Therefore the fraction of the incoming beam lost due to the grid and surface reflections is constant; and hence when the slope of each graph is taken it can then be divided by the density of aluminium, which results is the mass absorption coefficient. This is a great achievement as we are effectively negating the effect of not only the oxide layer but also the presence of the grid on which the films are supported.

For comparison purposes the density is taken in g/cm^3 as opposed to g/m^3 ; this is due to all the other authors using these units for calculating the mass absorption coefficient. The results for this experiment are shown in Table 5-8 and displayed in Figure 5-31. The associated error in each result is achieved due to the error in the fitting of the straight-line for the natural log of transmission versus thickness graphs. This error is noticeably smaller for the measurements taken without a filter due to the smaller error in the measuring of the transmission/incoming ratio.

Table 5-8 Slope and absorption coefficient calculations at all wavelengths for aluminium taken from the graphs above.

Wavelength (nm)	Energy (eV)	slope / 10 ⁺⁶	error / 10 ⁺⁶	Absorption Coefficient (cm ² /g)	error (cm ² /g)
30.2	41.0	3.38	0.65	1.25	0.024
31.7	39.1	3.58	0.57	1.32	0.212
33.5	37.0	4.66	0.65	1.72	0.024
35.4	35.0	3.52	0.44	1.30	0.016
37.5	33.0	4.16	0.47	1.54	0.017
40.0	31.0	3.29	0.46	1.22	0.017
42.7	29.0	2.89	0.39	1.07	0.014
44.2	28.0	3.36	0.35	1.25	0.013
47.6	26.0	1.05	0.42	0.39	0.016
49.6	25.0	1.21	7.38	0.45	0.027
51.6	24.0	10.77	4.73	3.99	0.175
59.0	21.0	4.31	0.31	1.59	0.011
68.8	18.0	10.76	5.12	3.98	0.190
72.9	17.0	8.37	1.21	3.10	0.045
77.5	16.0	6.73	0.04	2.49	0.002
82.6	15.0	12.64	1.11	4.68	0.041
88.5	14.0	30.41	3.26	11.26	0.121

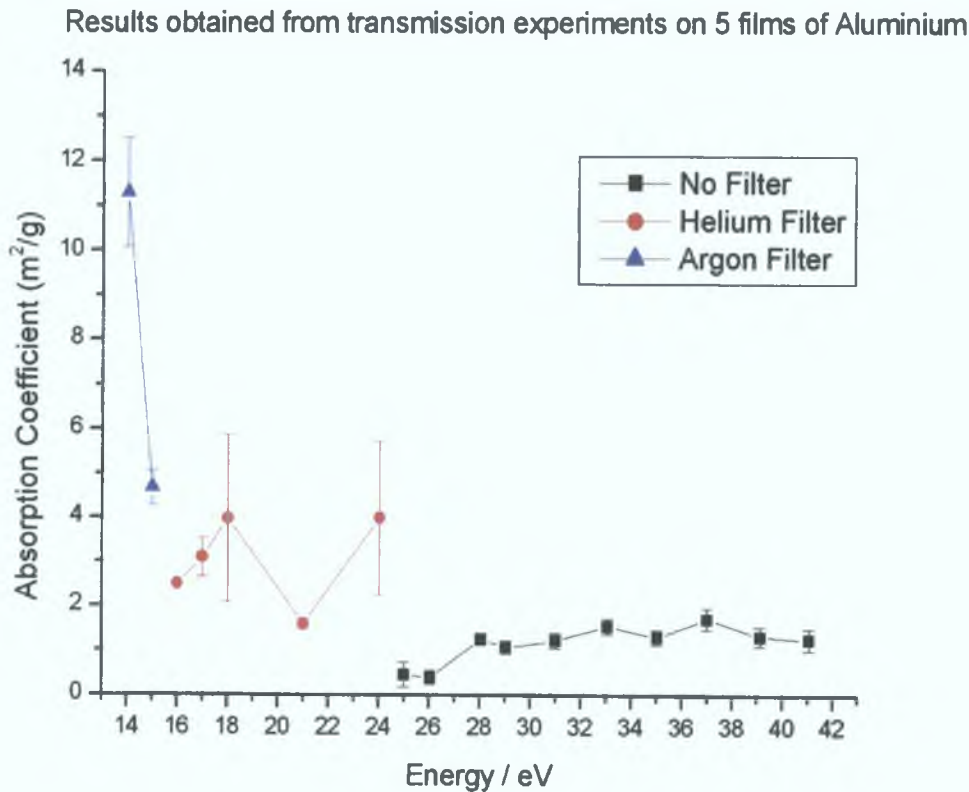


Figure 5-31 Absorption coefficient of aluminium determined in this work.

There is data in the literature from several authors concerning the absorption of aluminium in the VUV and X-ray region. These values can be found in papers by Henke *et al* [20], Gullikson *et al* [19], Scott [16] and Keenan *et al* [21]. There is some controversy between the measurements made by Henke and Keenan with those made by Gullikson, this allows us to add our data to the debate. Even with these inconsistencies these papers are of great assistance to us as some of the measured results coincide in energy range with those that we made. Also these same authors have the backing of large institutes and hence a wide range of state of the art equipment to choose from, it is encouraging to compare such a large facilities measurements to those made by an effective tabletop experiment such as ours. These data sets have been plotted along with the data obtained during this research and can be seen in Figure 5-32.

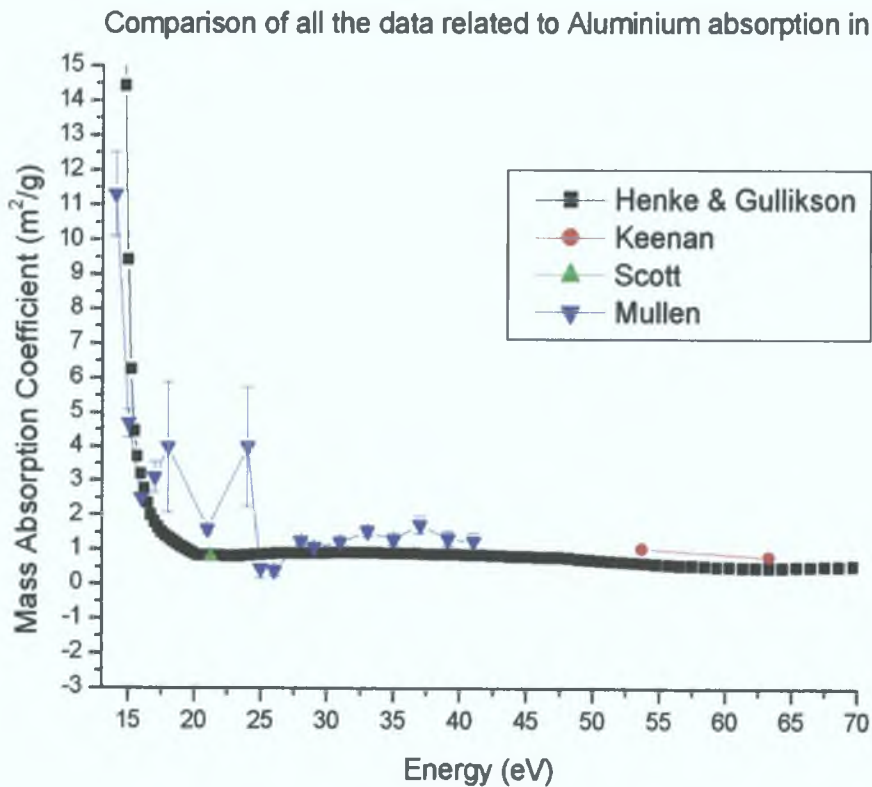


Figure 5-32 Mass absorption Coefficient of Aluminium as a function of photon energy. The Graph compares our data with data from the literature. Such measurements are often made and result in varying values due to different experimental conditions.

During the analysis problems were noticed with the helium data from 51.6-72.9nm (17-24eV). These values seemed to be unrealistically high with large errors as we can see in the graph. Another problem was noticed at 49.6nm (25eV) and 47.6nm (26eV), the values for both of these were too low. These values are suspected to contain second order light, which would explain the reduction in the absorption coefficient.

Apart from these difficulties, Figure 5-32 shows that even under the most taxing of circumstances, the suite of experimental and analytical systems that were developed is capable of obtaining experimental results comparable to world leading facilities. The main source of error in our research is due to the essential use of noble gas filters. When used at a different wavelength range, where solid state higher-order filters are available, we can confidently predict an even better performance. The final data in this work is in good agreement with the work of Henke *et al* who coincides at higher energies with Keenen *et al*, who utilised two Ni and Ge lasers for both their measurements at 57eV and 63eV. Scott's paper used reflectometry to determine the mass absorption coefficient.

With a value for the mass absorption coefficient it is a simple matter to extract imaginary refractive index data from it by using equations (2.18) and (5.17). This gives us values for the imaginary refractive index from 14 to 41eV (30-88nm). As has been stated in section 5.1 we get the best results when a data set is extended by either theoretical wings or by data from the literature. Fortunately there is a lot of data in the literature for the optical constants above and below this region ([50] and [20]), which we can use to compliment our experimental data. Values for the imaginary refractive index k can be easily calculated from the known value of the slope α using equations (2.18) and (5.17). When this was done we used a version of

our Kramers Kronig analysis program that utilises equation (2.37) to evaluate the real refractive index at all wavelengths, without any recourse to reflection and phase angles as in section 5.1. Figure 5-33 shows the result for the real refractive index.

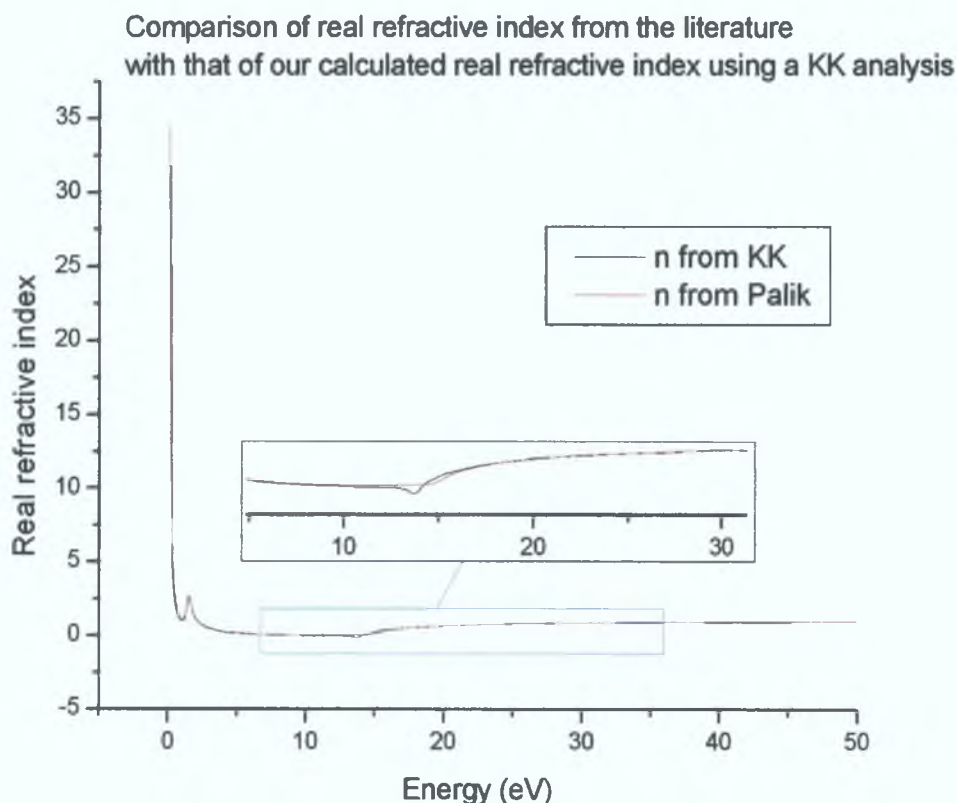


Figure 5-33 Graph of the real refractive index of aluminium from a Kramers Kronig analysis of the imaginary refractive index.

It is clear from the graph that some of our data has reduced the real refractive index in the 15-40eV region. An inertial sum rule test would not be reliable in this case as the data set used only ranged from 0.1 to 75eV. However it was carried out and resulted in a verification factor of 0.4594. If a larger data set was used this would be more reliable. It must be noted that the majority of the data in the literature is known to not take into account the oxide layer and so it is this that could be blamed for such a high verification factor. This would be improved upon if the oxide layer were taken into account when calculating the optical constants in all regions as stated by Shiles *et al* [8].

5.6 *Conclusions and Discussions*

The experimental system was fully tested in conjunction with the VUV beam. This testing entailed verification of the alignment of the chamber in the transmission set-up and the use of this set-up for experiments on calcium fluoride windows and aluminium thin films.

The computerised analysis system was continually improved upon until it was at the stage described in chapter 4. The system as it stands can deal with both reflection and transmission measurements and can effectively remove any holes resident in data gained from the samples under investigation.

The mass absorption coefficient of aluminium was then determined using the data from the experiments carried out. This mass absorption data of aluminium gained from the experiments seem to agree with the data published by Henke in the region below 49.6 nm and above 77.5 nm. The data in between these have large errors in them and so cannot be trusted until further experimental data is taken at these regions.

The development of the Kramers Kronig analysis software is a powerful tool for calculating optical constants from both reflection measurements and absorption measurements. It is also capable of calculating the real refractive index from the imaginary or vice versa. When this is used in conjunction with the inertial sum rule and partial f sum rules it becomes an even more powerful technique that is self testing. This allows us to examine more materials with greater certainty in the results.

5.7 *Future Work*

With the current data that is available further measurement at those wavelengths where we obtained large errors should be measured to gain a better value for the mass absorption coefficient

With the experimental chamber and analysis system in place it would be a fruitful effort to utilise the equipment and software to carry out experiments on not only aluminium but also other materials of interest as spectral filters in the VUV. With the introduction of a new grating for the spectrometer other wavelength regions could be examined with ease. Improvements could be made with the sample holder to adjust the tilt as such adjustments would drastically speed up the alignment procedure required for the reflection experiments. The analysis system, although complete, could be improved with the use of a suitable graphical user interface. Such an interface would make the analysis a lot easier and user friendly to the experimentalist.

The calculated optical constants of aluminium show the need for the rest of the data range to also take into account the oxide layer in the calculations. Such a measurement would greatly increase the accuracy of measurements made with metallic aluminium. Such a system could also be applied to any highly oxidising materials or even for the measurement of thin films that require support.

References

- [1] W R Hunter *App Opt* 21, 12 (1982) 2103-2114
- [2] R deL Kronig, *J Opt Soc Am* 12, 547-557 (1926)
- [3] Kramers, H A *Atti Congr Intern Fisici* 2, 545, 1927
- [4] R deL Kronig, *Ned Tijdschr Natuurk* 9, 402 (1942)
- [5] C W Peterson *et al J Opt Soc Am* 65, 10 (1973) 1238-1242
- [6] M L Bortz and R H French *App Spec* 43,8, 1989 (1498-1501)
- [7] A H Abdullah, W F Sherman *Vib Spec* 13, (1997) 133-142
- [8] E Shiles *et al Phys Rev B* 22, 4, (1980)
- [9] J H Barkyoumb *et al Phys Rev A* 41, 9 (1990) 4863-4867
- [10] H Ehrenrich *et al Phys rev* 128, 4, (1962)
- [11] H Ehrenrich *et al Phys Rev* 132, 5, (1963)
- [12] E A Taft and H R Phillip *Phys Rev* 121, 1100 (1961)
- [13] J L Larruquert *et al App Opt* 33, 16, (1994), J L Larruquert *et al Opt Comms* 124, (1996) 208-215, J L Larruquert *et al App Opt* 32, 31, (1993), J L Larruquert *et al App Opt* 34, 22, (1995), J L Larruquert *et al App Opt* 35, 28, (1996), J L Larruquert *et al Opt Comms* 135, (1997) 60-64
- [14] J A Aznarez *et al Rev Sci Instr* 67, 2, (1996)
- [15] R F French *et al J Am Ceram Soc* 81, 10 (1998) 2549-2557
- [16] M L Scott *App Opt* 27, 8, (1988) 1503-1507
- [17] R Swanepoel *J Phys E Sci Instruments* 16 (1983) 215-222
- [18] R Swanepoel *J Phys E Sci Instruments* 17 (1984) 896-903
- [19] E M Gullikson *et al Phys Rev B* 49, 23, (1994) 16283-16289

- [20] B L Henke *et al* At Data Nucl Data tables 54, 181 (1993) available at [http //www-cxro lbl gov/optical_constants/](http://www-cxro.lbl.gov/optical_constants/)
- [21] R Keenan *et al* J Phys B At Mol Opt Phy 35 (2002) L447-L451
- [22] M Kubinyi *et al* Thin Solid Films 286 (1996) 164-169
- [23] I Chambouleyron *et al* App Opt 36, 31, (1997) 8238-8247
- [24] V Denks *et al* App Sur Sci 158 (2000) 301-309
- [25] Y Laaziz *et al* Thin Solid Films 303 (1997) 255-263
- [26] Y Laaziz *et al* Thin Solid Films 277 (1996) 155-161
- [27] Y Laaziz *et al* Thin Solid Films 372 (2000) 149-155
- [28] M Kepinska and M Nowak NDT&E International 13, 2 (1998) 105-110
- [29] Carillon A, Jaegle P, Dhez P, Physical Review Letters, Vol 25, p140, (1970)
- [30] Breton C and Papoular R , Journal of the Optical Society of America, Vol 63, p 1225,(1973)
- [31] Carroll P K, Kennedy E T, O'Sullivan G, Optics Letters, Vol 2, p 72, (1978),
O'Sullivan G, Carroll P K, McIlrath T J, Ginter M L, Applied Optics, Vol 20, p 3043, (1981), O'Sullivan G, Roberts J R, Ott W R, Bridges J M, Pittman T L, Ginter M L, Optics Letters, Vol 7, p 31, (1982)
- [32] P K Carroll and E T Kennedy, Contemp Phys 22, 1, 61 (1981)
- [33] J T Costello, J P Mosnier, E T Kennedy, P K Carroll and G O'Sullivan, Physica Scripta T34, 77 (1991)
- [34] E T Kennedy, J T Costello, J-P Mosmer, A A Caffola, M Collins, L Kiernan, U Koble, M H Sayyad & M Shaw, Opt Eng 33, 3964 (1994)
- [35] W Whitty and J-P Mosnier , Appl Surf Sci 127-129, 1035 (1998)
- [36] M Stapleton PhD Thesis 2004
- [37] J S Hirsch *et al* Rev Sci Instr 74, 6 (2003) 2992-2998

- [38] L. Ward, The optical constants of bulk materials and thin films, Bristol, England; Philadelphia : A. Hilger, 1988
- [39] W.R. Hunter, Ultraviolet and vacuum ultraviolet systems, Washington press 1981 (Proceedings of SPIE)
- [40] E. Hecht, Optics 3rd edition, Addison-Wesley 1998
- [41] M. Altarelli *et al* Phys. Rev. B, 6,12, 4502(1972)
- [42] P.K. Carroll, E.T. Kennedy, and G. O'Sullivan, Appl. Opt. 19,1454 (1980)
- [43] O. Meighan *et al* Appl. Phys. Lett. 70(12) 1997 & M. Beck *et al*. Opt. Comms. 190, 317-326 (2001)
- [44] J. S. Hirsch Phd thesis 2003
- [45] Andor communication 2004
- [46] L. Poletto *et al* Applied Optics 38,1 , 29-36(1999)
- [47] N. Smith private communication 2004
- [48] Model FTM5 Thickness Monitor instruction Manual
- [49] Nanotec WsXm can be downloaded from <http://www.nanotec.es>
- [50] E. D. Palik, Handbook of optical constants of solids, Academic Press 1985
- [51] E. D. Palik, Handbook of optical constants of solids II, Academic Press 1991
- [52] National Institute of Standards and Technology at www.nist.gov and associated references
- [53] Leybold Thermovac Tr 211 vacuum gauge manual, Leybold Penningvac Pr 25 vacuum gauge manual
- [54] J. Mullen, P. Van Kampen, Determination of optical constants and thickness imaging of thin films, SPIE Proceedings, 4876, 2002.
- [55] J. Mullen, P. Van Kampen, future publication.
- [56] J. Mullen, P. Van Kampen, future publication.

Appendix A

Obtaining File Lists

This can be done by opening a DOS prompt in windows, accessing the directory containing the ascii files and running the command 'dir > files.txt'. This will output all the details of the directory into a 'files.txt' file. Converting the file to a useable list is easily achieved by using any spreadsheet program, by importing the file and using a space delimited format. Once in this format the required sections may simply be copied and pasted into a new text file.

Sorting of files into directories

At this point Matlab is used to process all the data. All the programs that were written in Matlab for this project require a certain file naming convention to be applied to the data files: (sample name)_(filter)_(measurement type)_(wavelength)_(shot details)_(slit widths)_(binning)_(target number)_(shot number). This file convention allows for quick separation of the files into subdirectories for each experiment and for ease of analysis. A typical image of the beam can be seen in Figure A-1.

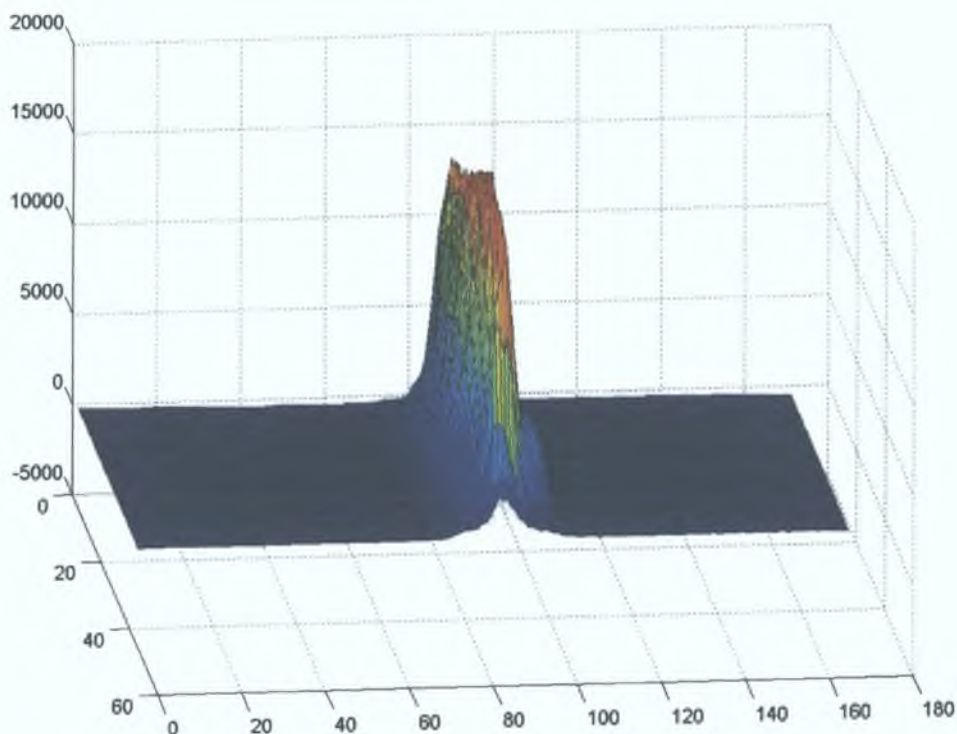


Figure A-1 Three-dimensional image of the incoming beam recorded with the CCD camera.

The initial processing is carried out by using the program *'bulkconstructorpixel12'*. It automatically makes minor alterations to the file and then places each file into a new directory after making by */analysisastro/'sample'/'filter'/'wavelength'/'*. It produces a list of all files processed and a list of all the files with the same 'sample', 'filter' and 'wavelength' values, while placing these lists in their corresponding directories. From this point the files need to be separated into those that contain incoming, reflected and transmitted data for each 'wavelength' directory. This is movement of files is done by using the program *'bulkmovesig15'*. The resulting directory structure can be seen in Figure A-2.

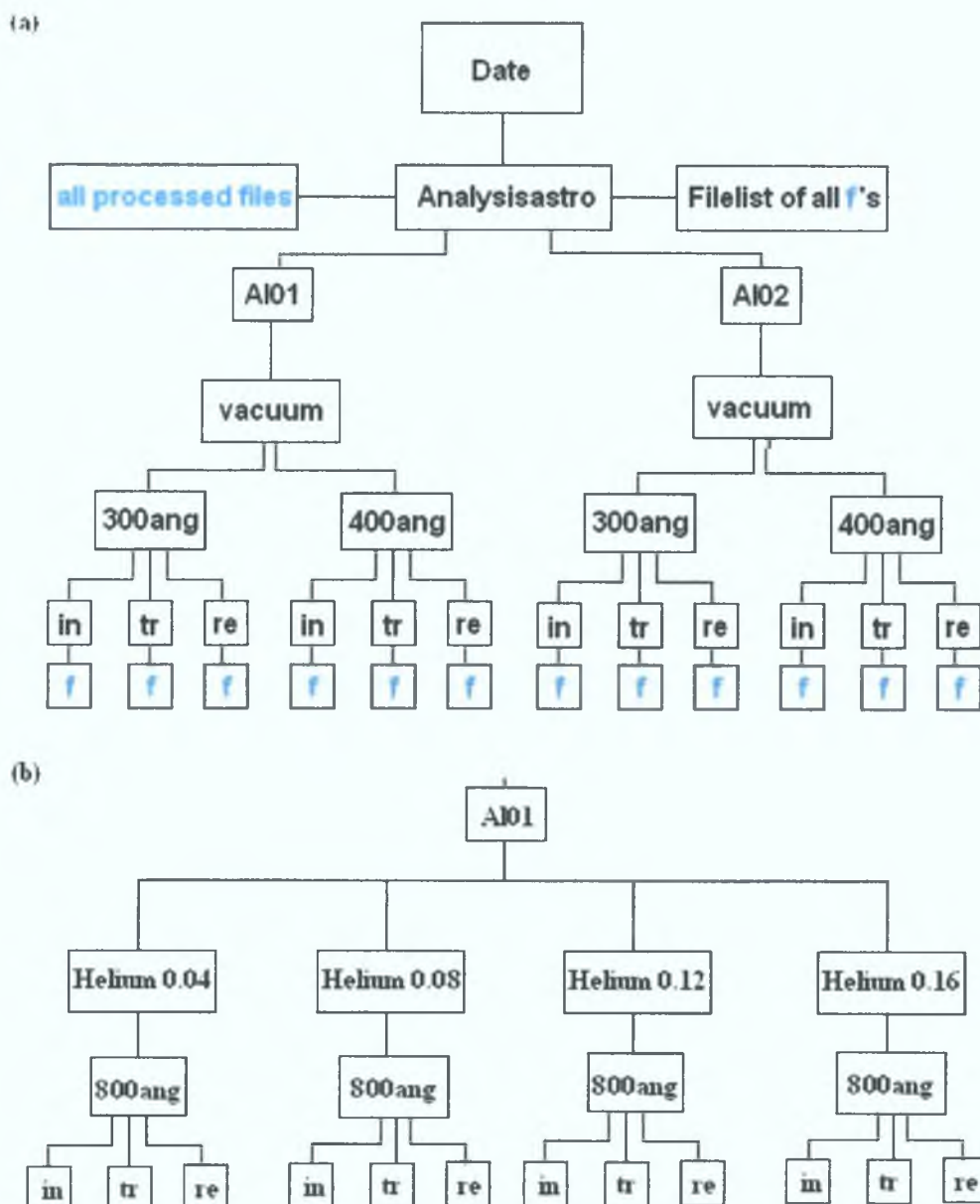


Figure A-2 (a) The directory structure that is required by the analysis system for automation. It uses two samples Al01 and Al02 with two vacuum wavelengths 300 and 400 Angstroms. The blue f's stand for the file lists. None of these wavelengths require any filter. **(b)** The structure that is required when a gas filter is used. The top part of the directory structure is the same as in a.

Each wavelength box in the diagram has a file list that is listed in another file list in the 'analysisastro' directory. This main file list allows for automating the analysis of all the measurements.

Step by step guide to the Analysis

- 1 Convert `sif` image files from the CCD to `asc` files using the Andor® software
- 2 Create a file list using dos commands and a suitable spreadsheet as described above
- 3 Open up Matlab® and run `bulkfconstructor11('filelist.txt',0,0)` on the `filelist.txt` generated from 2
- 4 Run `Analyastro11('filelist.txt')` where `filelist.txt` is open `txt` generated from 3 in the Astroanalysis directory
- 5 Examine all the `jpeg` images for each film and decide if a smaller elliptical mask needs to be applied Run `bulkfalterateellipse10('filelist.txt',y1,x1,y2,x2)` where `filelist.txt` is the last incoming file list generated for each wavelength, `y1,x1` are the bottom left coordinates of the rectangle encompassing the new ellipse and `y2,x2` are the top right coordinates
- 6 Check all images for holes still remaining in the images and extract them by using `bulkfbottomhalf('filelist.txt',line)` and `bulkftophalf('filelist.txt',line)` where `filelist.txt` is the last incoming file list and `line` is the line above or below which the half of the image is being removed
- 7 Run `goaverage('filelist.txt')` on the last incoming file list generated

Program listing on the CD

`align1Dfile.m`

- very simple alignment of two 1d files

AllAstroAnalysis2dalign11a m	- Carries out all analysis on a data set and results in a data file containing incoming and transmission image summations
AnalyAstro11 m	- Utilises 'AllAstroAnalysis2dalign11a' on all the data sets carried out in a day to automatically do the analysis
arrArrayAlign1d m	- aligns up two arrays
arrArrayAlign2d m	- aligns up two 2d arrays
arrayconstructor m	- initial correction made to images to remove line numbers and rotate them
arrayeVtonm m	- converts first column of array from eV to nm
arraynmtoeV m	- converts first column of array from nm to eV
arrfinealignment2d10 m	- fine aligns two arrays with an interpolation of 10 times the size of the array to be aligned
bulkfalign2dfilesfine12a m	- main program for carrying out fine aligning of all the files in a set It is used in the automation
bulkfalign2dfileswrough13a m	- main program for carrying out rough aligning of all the files in a set It is used in the automation

<code>bulkfalterenateellipse10 m</code>	- used after automation routine to shrink the elliptical mask and regenerate the images
<code>bulkfaverage10 m</code>	- Averages all the images and outputs the results to a text file <code>bulkfbottomhalf m</code>
<code>bulkfconstructorpixel12 m</code>	- Initial editing of the entire data set images <code>bulkfinterpolate13 m</code>
<code>bulkfmovesig13 m</code>	- movement of images into their specified directories
<code>bulkfsavejpeg10 m</code>	- Saves the specified images to jpeg format
<code>bulkfsavejpeg1d10 m</code>	- Saves 1d images to jpeg format
<code>bulkfsavejpegdetail10 m</code>	- saves high detail jpeg images
<code>bulkfsigmmusbgd11 m</code>	- removes background file if this option was not selected during the experiments
<code>bulkfsumarrays10 m</code>	- sums up all the pixels of each image in a data set
<code>bulkftophalf m</code>	- removes top of each image in a set at a specified height This is used to remove holes in the films
<code>Dielconst m</code>	- Calculates the dielectric constants from both optical constants
<code>fnkerror m</code>	- calculates the error between two sets of optical constants This is used to compare original optical constants to those generated using a KK analysis

foptconsts m	- generates the optical constants from reflectance and phase change data after a KK analysis on the reflectance
ImagKKDenn m	- KK analysis program to find the real refractive index from the imaginary refractive index
Inertial m	- Calculates the verification factor for the inertial sum rule
Intersumarrays m	- Interpolates the incoming values and outputs them along with the transmission values in the root data set directory
kkprep m	- prepares reflectance data for a KK analysis
makemask M	- Creates mask to eliminate background noise around the signal
mangle m	- angle correction used in the R/T setup
mflip m	- image flipping also used in the R/T setup
msave m	- main image saving system
Partial_sum_absorption m	- calculates the effective number of electrons interacting from imaginary refractive index data (see partial f sum rules)
RefKKDenn m	- KK analysis of reflectance data
wavelength2noise m	- assigns noise level in the CCD at each wavelength

Appendix B

Examples of holes found in the samples.

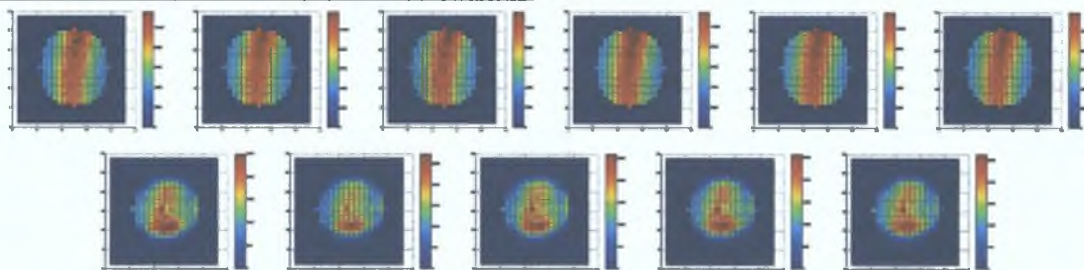


Figure B-1 9.5nm film taken at a wavelength of 49.6nm. The hole at the bottom was consistent at all wavelengths and the hole had to be removed from the analysis.

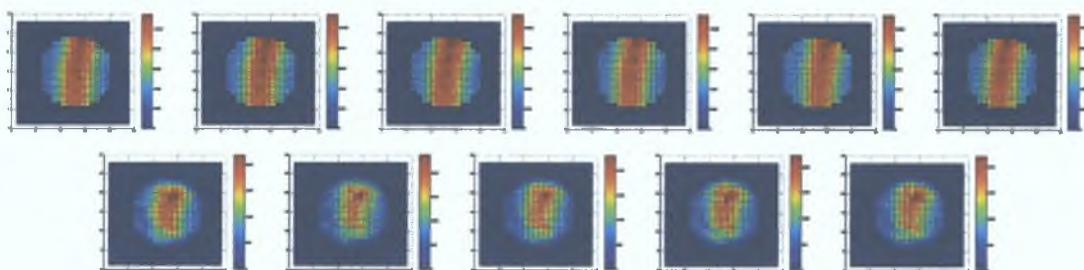


Figure B-2 18.6nm film taken at a wavelength of 49.6nm. The small hole at the top was removed prior to averaging the transmission.

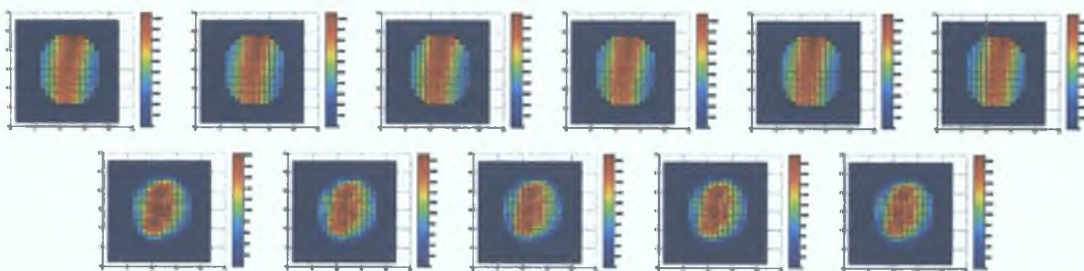


Figure B-3 21.6nm film taken at a wavelength of 49.6nm. No visible hole was located across the wavelength range that scanned this film.

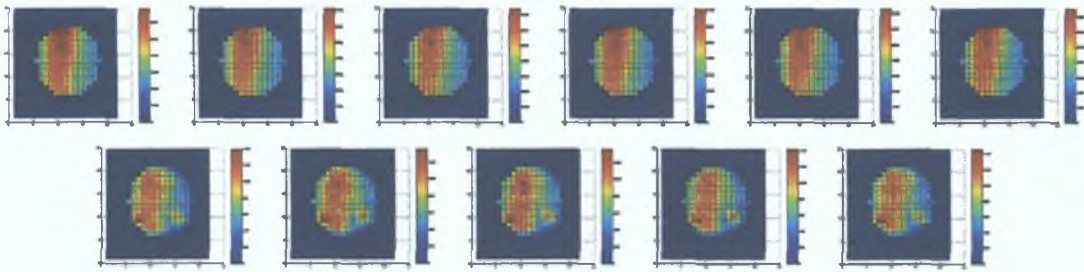


Figure B-4 28.7nm film taken at a wavelength of 49.6nm. The hole on the right was removed prior to further analysis.

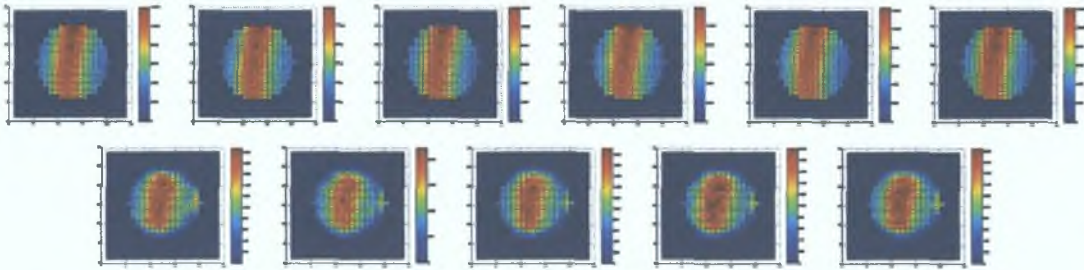


Figure B-5 42.1nm film taken at a wavelength of 49.6nm. The hole on the right was removed once it was notice to be consistent through all the measurements.

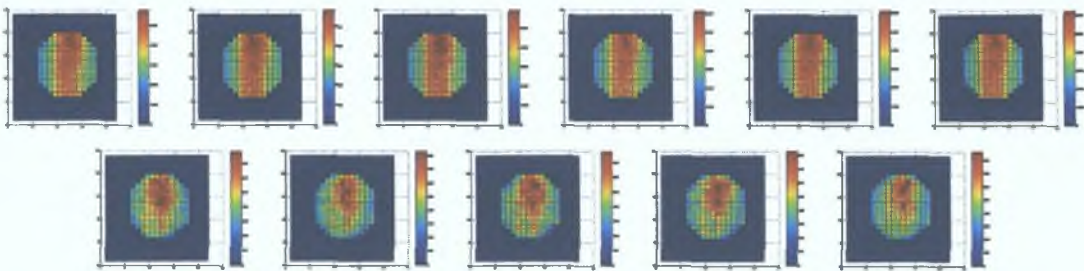


Figure B-6 54.7nm film at a wavelength of 49.6nm. This contained the largest whole of all the samples.

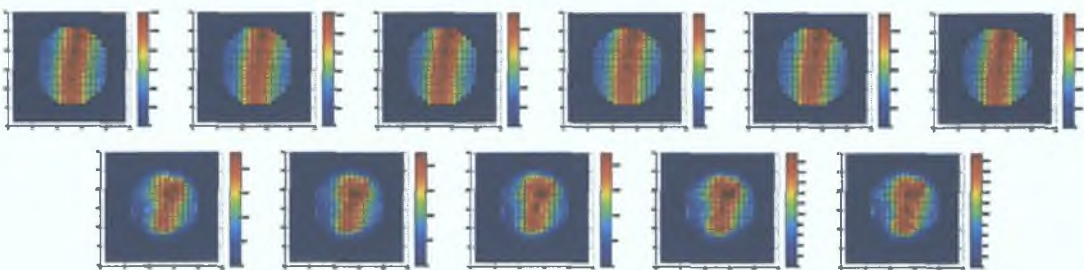


Figure B-7 60.6nm film at a wavelength of 49.6nm.

AFM Images

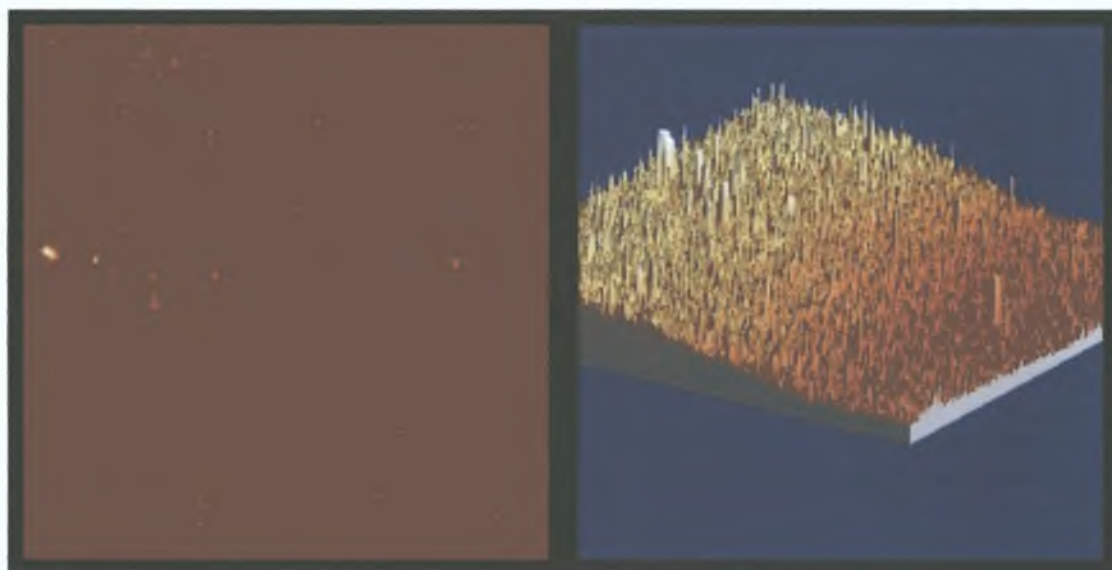


Figure B-8 Image of 54.7nm film. Image on the left is the original image while the image on the right is a 3D representation of the image after the bend in the image was removed.

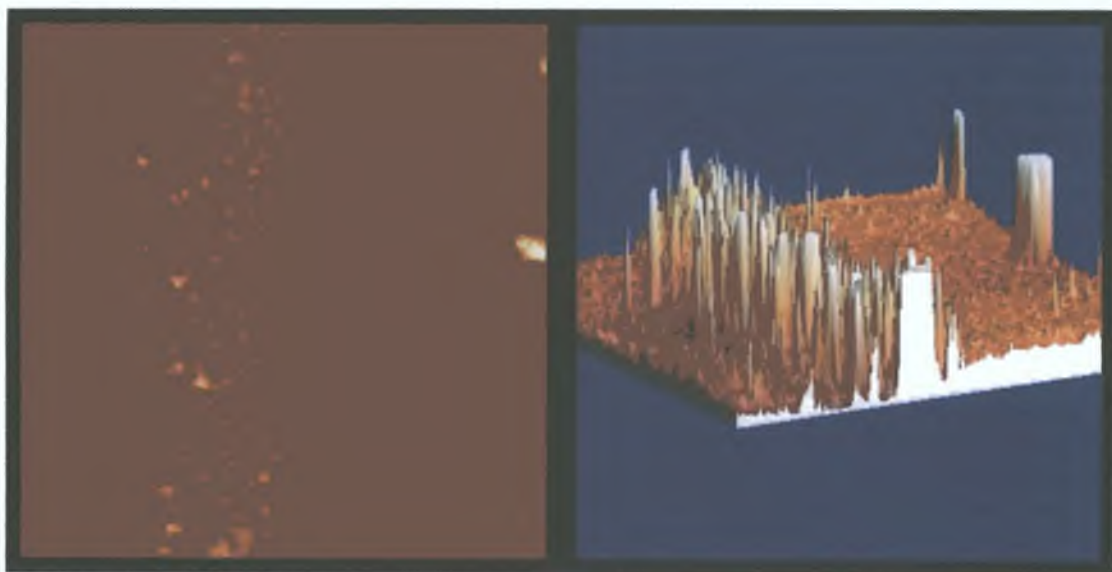


Figure B-9 Image of 28.7nm film. Image on the left is the original image while the image on the right is a 3D representation of the image after the bend in the image was removed.

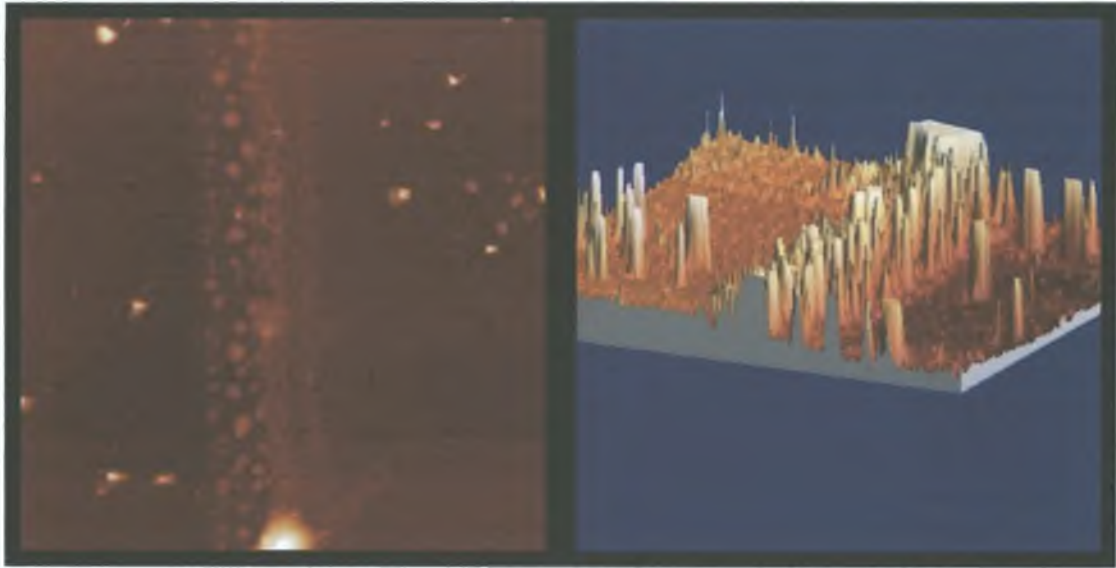


Figure B-10 Image of 18.6nm film. Image on the left is the original image while the image on the right is a 3D representation of the image after the bend in the image was removed.

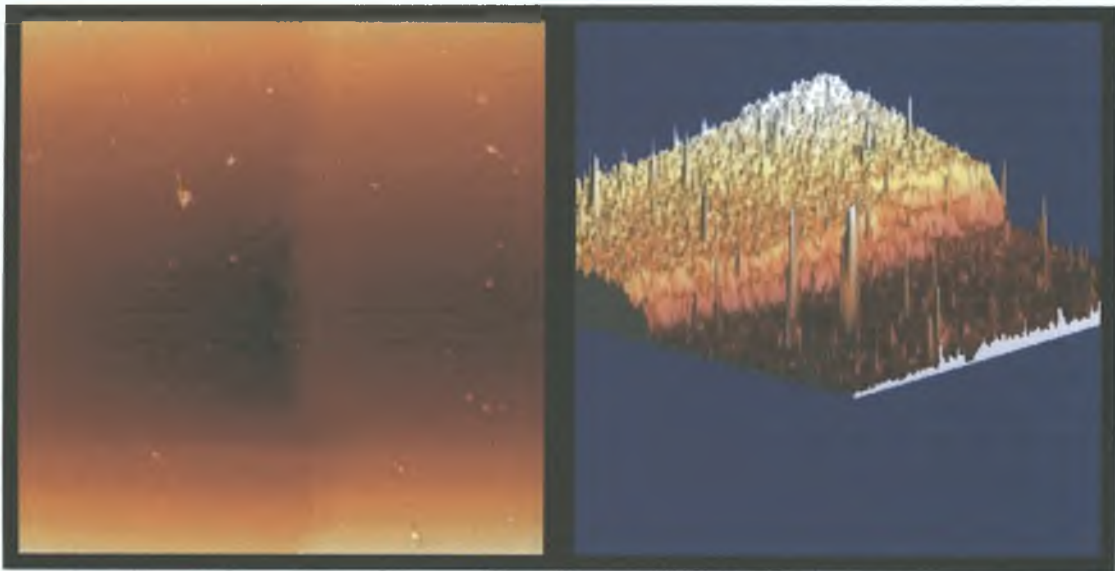


Figure B-11 Image of 42.1nm film. Image on the left is the original image while the image on the right is a 3D representation of the image after the bend in the image was removed.

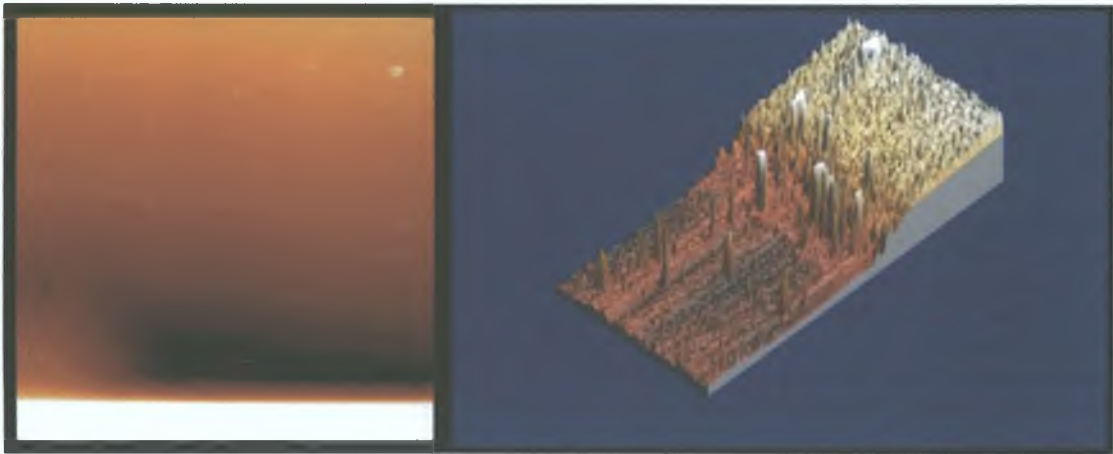


Figure B-12 Image of 60.6nm film. Image on the left is the original image while the image on the right is a 3D representation of the image after the bend in the image was removed.

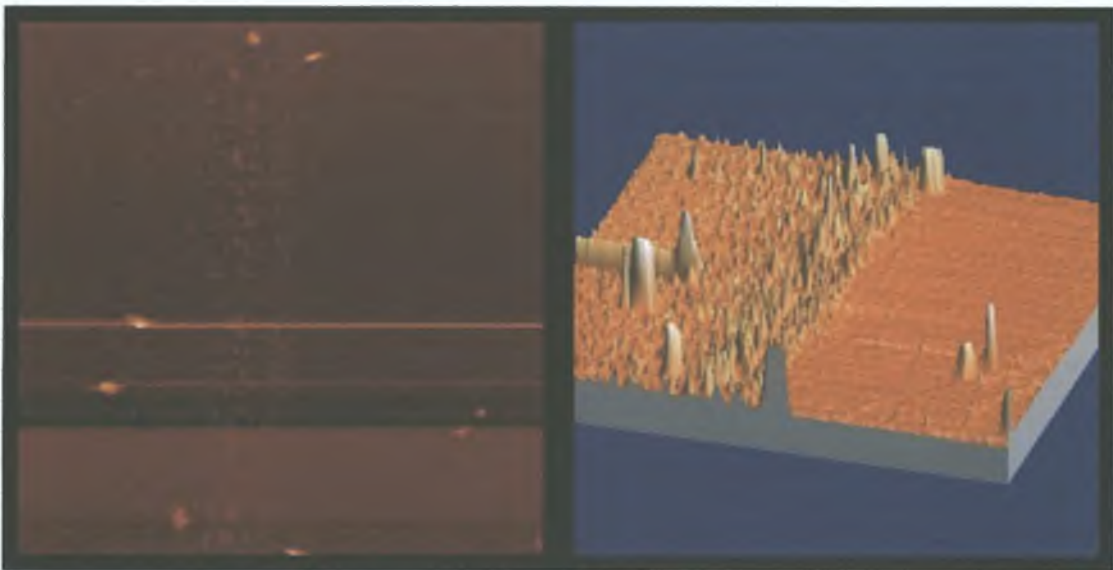


Figure B-13 Image of 9.5nm film. Image on the left is the original image while the image on the right is a 3D representation of the image after the bend in the image was removed.

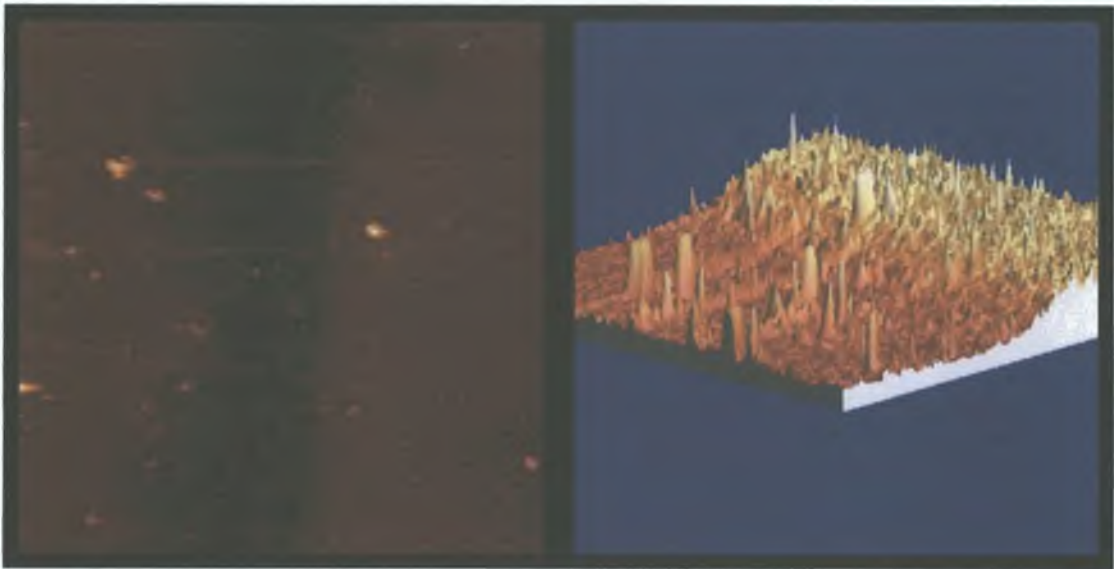


Figure B-14 Image of 21.6nm film. Image on the left is the original image while the image on the right is a 3D representation of the image after the bend in the image was removed.

Graphs of photoabsorption of aluminium

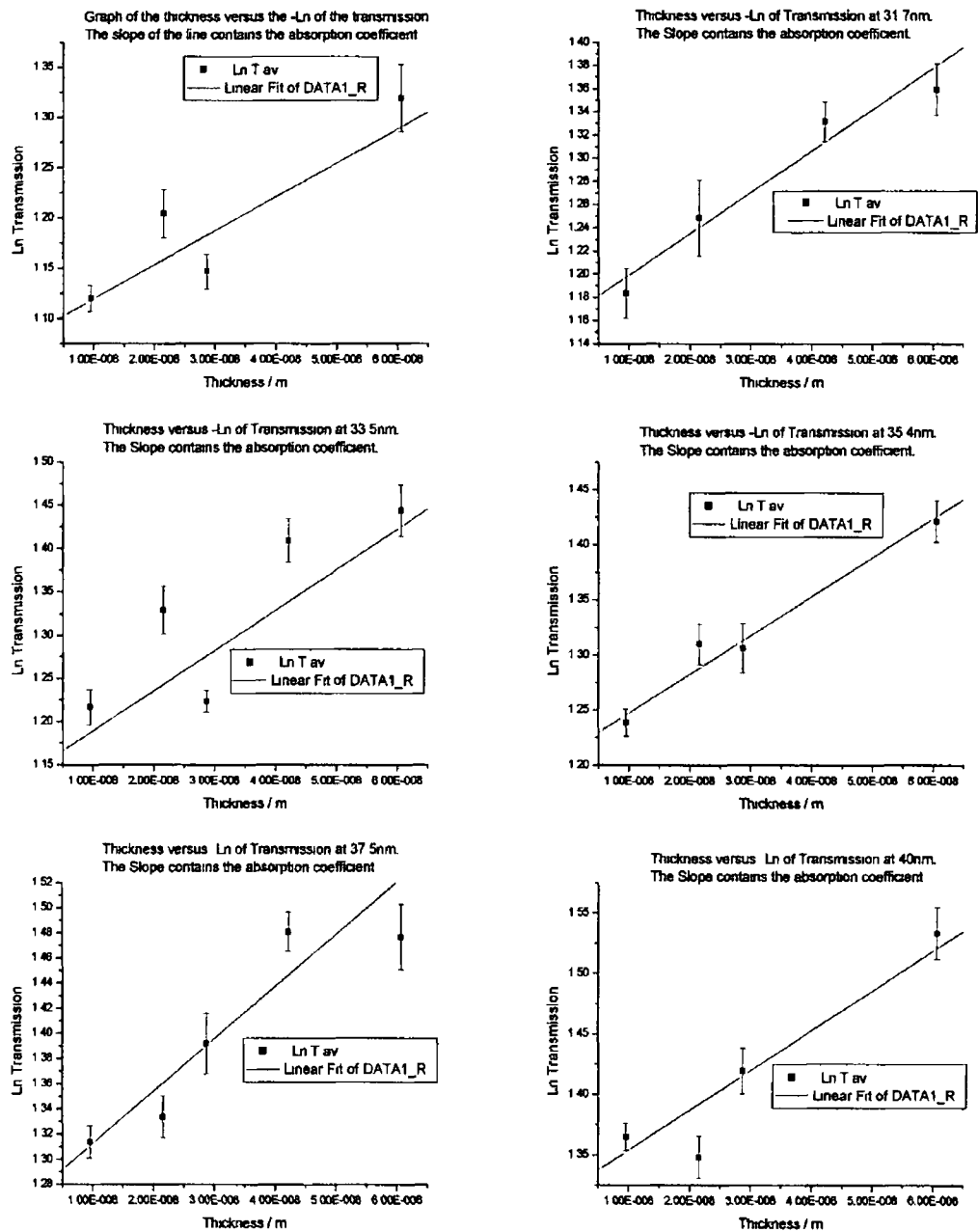


Figure B-15 Graphs of $-\ln$ Transmission versus thickness for wavelengths from 30.2-40 nm. The slope of each graph contains the absorption coefficient of aluminium.

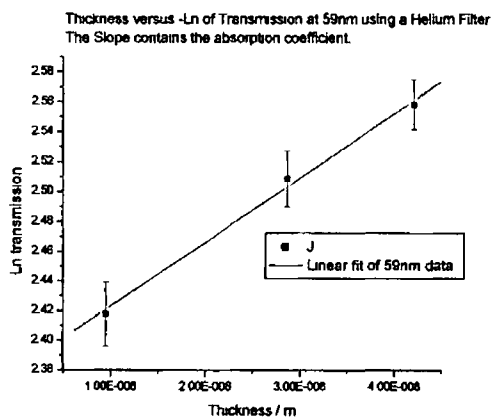
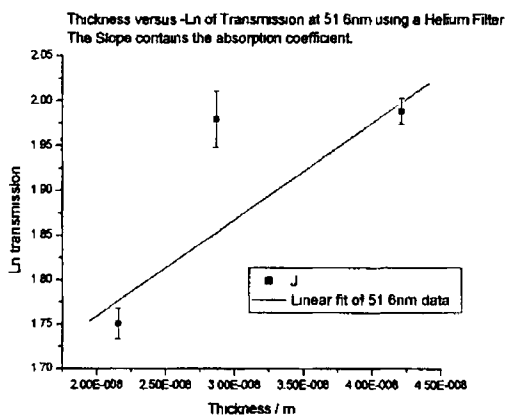
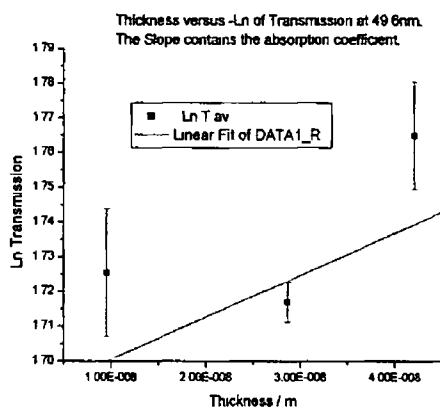
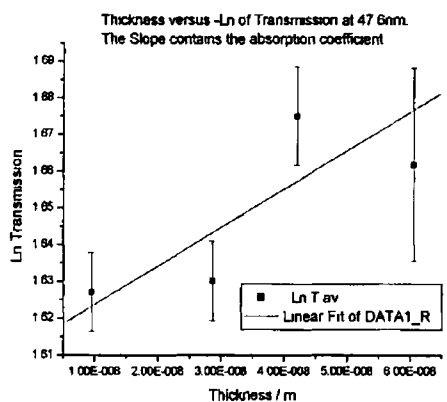
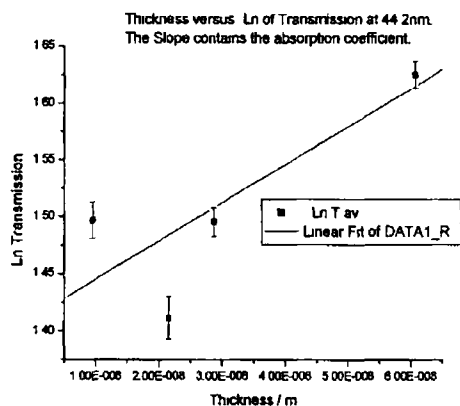
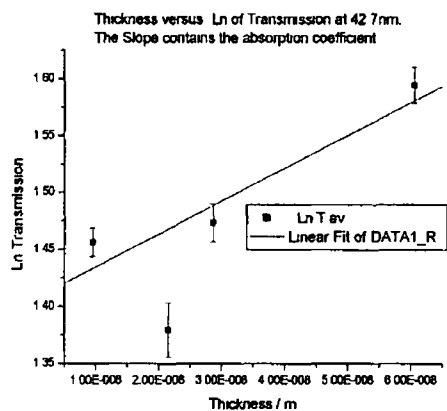


Figure B-16 Graphs of -Ln Transmission versus thickness for wavelengths from 42.7-59nm. The slope of each graph contains the absorption coefficient of aluminum.

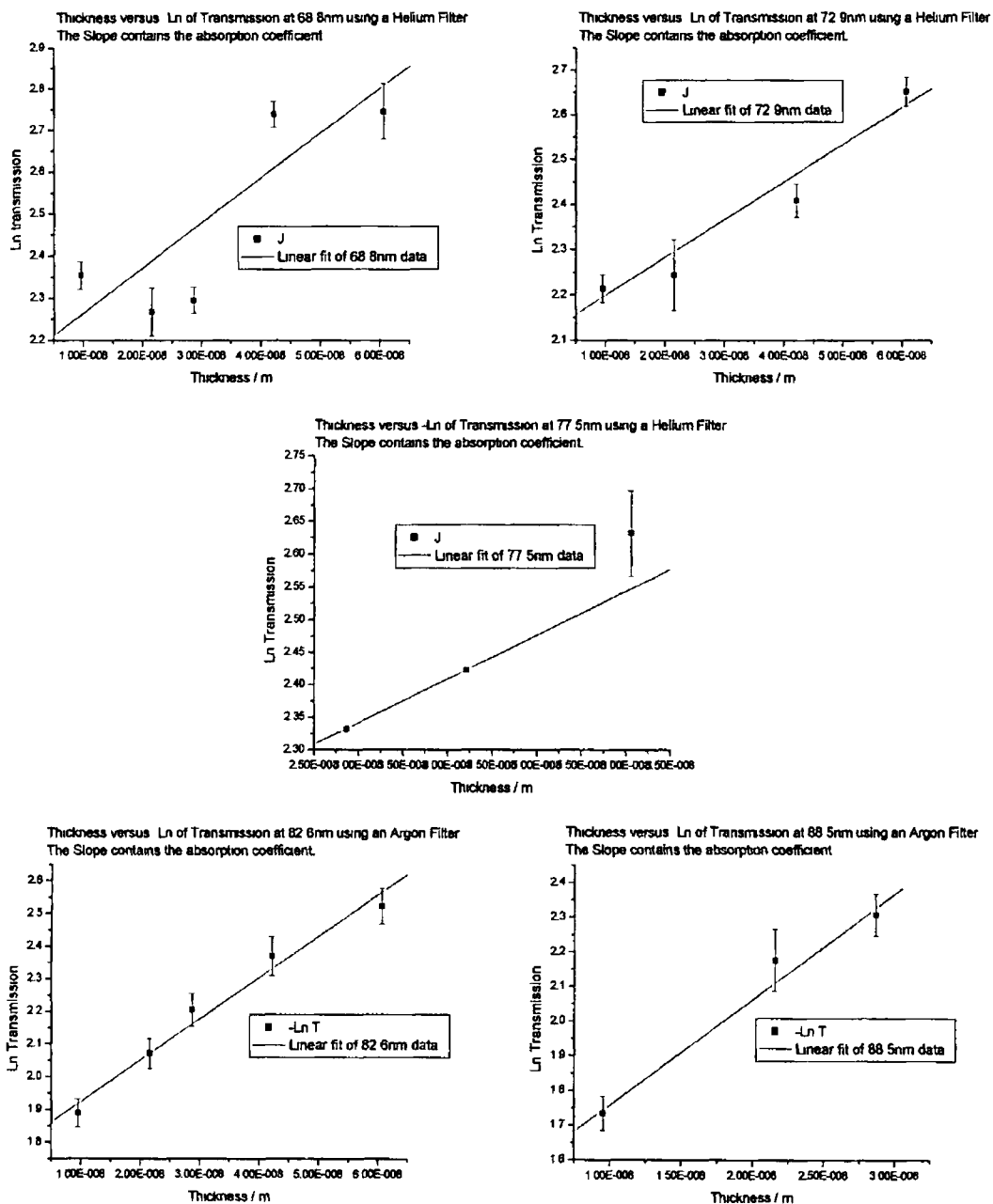


Figure B-17 Graphs of $-\ln$ Transmission versus thickness for wavelengths from 68.8-88.5 nm. The slope of each graph contains the absorption coefficient of aluminum.